A&A 487, 485–502 (2008)
DOI: 10.1051/0004-6361:200809666

Astronomy & Astrophysics

Broad-band *BVRI* photometry of isolated spiral galaxies⋆

H. M. Hernández-Toledo and S. Ortega-Esbrí

Instituto de Astronomía, Universidad Nacional Autónoma de México, Apartado Postal 70-264, 04510 México D. F., México
e-mail: [hector;sortega]@astroscu.unam.mx

Received 27 February 2008 / Accepted 14 May 2008

ABSTRACT

Context. Uniform and high resolution observations in samples of isolated galaxies are required to estimate fundamental morphological and structural parameters for comparative studies of environmental effects and for confronting model predictions of galaxy evolution. A subsample of The Catalog of Isolated Galaxies (CIG), Karachentseva (1973), has been uniformly observed at San Pedro Mártir National Observatory in México and a photometric and morphological study of these galaxies has been carried out.
Aims. We report multicolor broad band (*BVRI*) photometry for a subsample of 40 isolated spirals drawn from the CIG. Total magnitudes and colors at various circular apertures as well as a detailed morphological analysis that is extended into the NIR bands are presented. Some structural parameters are estimated from the global light distribution in the optical and NIR bands to complement our morphological analysis and several correlations between the photometric and structural parameters are explored. Emphasis was given to the detection of morphological distortions at high/low intensity levels.
Methods. The observations, data reduction, and analysis are described. Morphology is reevaluated from a combination of optical logarithmically scaled *R* band images, filter-enhanced *R* band images, $(B-I)$ color index maps, archived near IR *JHK* images from the TwoMicron Survey and optical-NIR ϵ and PA radial profiles after an isophotal analysis. *RGB* images from the SDSS database were retrieved when available to complement our analysis. The *CAS* structural parameters (Concentration, Asymmetry, and Clumpiness) were calculated from the images in each band.
Results. The fraction of galaxies with well-identified optical/near-IR bars (SB) is 40%, while another 25% shows evidence of weak or suspected bars (SAB). The sample average value of the maximum bar ellipticity is $\epsilon_{\rm max} \approx 0.35$. 57.5% of the galaxies in the sample show rings. The *CAS* parameters change with the observed band, the morphological type and global color. We found 9 isolated galaxies with disturbed morphology. After reviewing their local number density and tidal strength parameters, we identified CIG 744 as a morphologically disturbed isolated galaxy having $M_{\rm HI}/L_I > 1$; a tentative candidate to interact with a dark gas-rich object. However, its loci in the $\mu_0^{\rm I}/\log(M_{\rm HI}/L_I)$ diagram, suggests that CIG 744 is itself a gas-rich disturbed-isolated galaxy probably in a lengthy or ongoing process of formation, instead.

Key words. galaxies: spiral – galaxies: structure – galaxies: photometry – galaxies: interactions – galaxies: fundamental parameters – galaxies: general

1. Introduction

The origin of the morphology of galaxies is one of the fundamental pieces to understand galaxy formation. One of the legacies of surveys like the Sloan Digital Sky Survey (SDSS) is that now we have a more extended view of the local universe allowing to look for fundamental relations between physical properties of galaxies at local and larger-scale environment. Recently, Park et al. (2008) used the SDSS data and studied the environmental dependence of the observed morphology at different smoothing scales to address the question of whether galaxy morphology depends primarily on the large-scale environment in which the galaxy initially formed, or on a smaller scale environment that may reflect the influence of later evolutionary effects such as galaxy-galaxy interactions. Park et al. (2008) pointed out that galaxies statistically become more isolated if they recently merged, and that at a fixed large-scale density more isolated galaxies are more likely to be recent merger products. It is therefore possible that the disturbed isolated ones are galaxies that recently experienced mergers.

An alternative explanation for finding disturbed morphology in isolated galaxies comes from the results of cosmological numerical simulations within the CDM model that show that a high population of subhalos survive inside galaxy-sized halos (Klypin et al. 1999; Moore et al. 1999). These sub-halos and the associated gas clouds could produce signs of morphological distortion on isolated galaxies (Trentham et al. 2001; Pisano et al. 2002).

These results emphasize the need of a careful identification of galaxies in isolated environments that may show evidence of disturbances not associated to intrinsic processes. Recently, Karachentsev et al. (2006, 2007), searched for disturbed (interacting) objects among very isolated galaxies. They inspected the galaxies in the Catalog of Isolated Galaxies (Karachentseva 1973, hereafter CIG) from the blue POSS-II images available on the digital Sky Survey, finding 5/1050 strongly disturbed galaxies and suggesting that the existence of "dark" galaxies could explain the observed signs of distortion.

An equally important problem, apart from identifying disturbed galaxies in isolated environments, is that of a detailed morphological classification of the isolated galaxies themselves. It is actually not clear whether or how far the morphological trends observed in clusters or groups extend to an environment typical of isolated galaxies.

The CIG is one of the most uniformly selected and complete samples of local isolated galaxies available in the literature.

⋆ Appendices A and B are only available in electronic form at http://www.aanda.org

Since its publication, the CIG has shown its usefulness for studies either of individual or statistical nature. Although recognized as a good comparison sample for studies on environmental effects, it has not been until recently that a careful revision of their main properties, and in particular, of its morphological content has begun. Sulentic et al. (2006) inspected the galaxies in CIG from the red POSS-II images available on the digital Sky Survey providing a uniform classification for these galaxies.

The aim of this paper is to present a global *BVRI* photometric and morphological analysis for 40 galaxies from the CIG based on new uniform and deeper CCD observations. We applied a uniform reduction pipeline and an image processing scheme to produce an homogeneous set of photometric and detailed morphological data. We take advantage of the higher resolution (~0.5″/pix) and higher dynamic range of our images to proceed with a new morphological revaluation for these 40 isolated galaxies that is extended into the NIR bands, giving special emphasis to the detection of low/high surface brightness morphological distortions. Further we carry out a structural analysis in the optical and NIR bands through the concentration, asymmetry and clumpiness (*CAS*) parameters, that complements our morphological study. A detailed morphological and structural characterization of galaxies in isolated environments is also useful for studying intrinsic secular processes that are able to affect the structure and dynamics of galaxies, for instance, the formation and evolution of bars, rings, lopsidedness, and bulges.

The outline of the paper is as follows: Sect. 2 describes the observations and reduction techniques used. We also present a comparison of our estimated total magnitudes against those in the literature. Section 3 presents a correction scheme for our apparent and absolute magnitudes and colors. In Sect. 4 we discuss the observed morphology based on logarithmically scaled *R*-band, *R*-band filtered-enhanced images, $(B-I)$ color index maps, composed near-infrared (NIR) *JHK* images extracted from the Two Micron All Sky Survey (2MASS) archives, optical/NIR ϵ and PA radial profiles after an isophotal analysis and *RGB* images from the Sloan Digital Sky Survey (SDSS). In Sect. 5 we present the results of the optical morphology with emphasis on the detection of distorted morphology in isolated galaxies. In Sect. 6 we present our estimates of the structural *CAS* parameters in the optical (*BVRI*) and NIR (*JHK*) bands. The loci of our isolated galaxies in the *CAS* diagrams space are presented. Here we also explore some basic correlations between the photometric and structural parameters in this sample that could be useful for comparative studies involving galaxies in other environments. Section 7 is a summary of the main conclusions achieved. An Appendix is devoted to the presentation of *BVRI* magnitudes at two other concentric circular apertures.

2. The data sample

2.1. Isolated spiral galaxies from the Karachentseva catalog

We have carried out an observational program at the Observatorio Astronómico Nacional at San Pedro Mártir (OAN-SPM), Baja California, Mexico, devoted to obtaining uniform and deep CCD photometric data for one of the most complete and homogeneous samples of isolated galaxies currently available, the Catalog of Isolated Galaxies (CIG) of Karachentseva (1973). The CCD *BVRI* images in the Johnson-Cousins system were obtained with a SITe1 detector attached to the 1.5 m telescope at OAN-SPM, covering an area of about $4.3' \times 4.3'$, with a typical seeing of 1.8″ and a scale of 0.51″ pixel^{-1}.

The 40 galaxies reported in this work were obtained in three observing runs and no special strategy was applied in selecting this current subset. Availability of observing time and good weather conditions were the main factors constraining the number of observed galaxies. Some aspects of the selection criteria for the CIG sample that are relevant to the present and further photometric analysis are described in Hernández-Toledo et al. (1999).

2.2. Data reduction

A journal of the photometric observations is given in Table 1. Column (1) gives the original catalog number, and Cols. (2)–(9) give the number of frames per filter, the integration time (in seconds), and the seeing conditions (in arc-seconds).

Table 2 reports some relevant information on the observed isolated galaxies obtained from literature. Column (1) gives the CIG number, Col. (2) reports other identifications, Col. (3) gives the apparent total m_B magnitude from the Lyon Extragalactic Database (LEDA), Col. (4) gives the Hubble Type from LEDA, Col. (5) gives the apparent total m_B magnitude from the NASA/IPAC Extragalactic Database (NED), and Col. (6) gives the radial velocity in kilometers per second, corrected for Virgo-centric infall from LEDA.

Images were de-biased, trimmed, and flat-fielded using standard IRAF[1] procedures. First, the bias level of the CCD was subtracted from all exposures.

Photometric calibration was achieved by nightly observations of standard stars of known magnitudes from the PG 1525-071, PG 1633+099, PG 1657+078, and M 67 fields of stars (Landolt 1992; and Chevalier & Ilovaisky 1991, respectively) with a global color range $-0.20 \leq (B-V) \leq 1.13$ and $-0.40 \leq (B-I) \leq 2.27$. Once the principal extinction coefficients in B, V, R and I were estimated, the transformations of the instrumental magnitudes to a standard system were:

$$\begin{aligned} B - b &= \alpha_B + \beta_B (b-v)_0, \\ V - v &= \alpha_V + \beta_V (b-v)_0, \\ R - r &= \alpha_R + \beta_R (v-r)_0, \\ I - i &= \alpha_I + \beta_I (v-r)_0; \end{aligned} \quad (1)$$

where B, V, R and I are the standard magnitudes, b, v, r, and i are the instrumental (and airmass-corrected) magnitudes, and α and β are the transformation coefficients for each filter.

Sky background was subtracted using an interactive procedure that allows the user to select regions on the frame free of galaxies and bright stars. This was also done by modeling the whole 2-D image. Errors in the determination of the sky background are, in fact, the dominant source of errors in the estimation of total magnitudes.

Within the galaxy itself, care was taken to identify superposed stars. A final step in the basic reduction involved registration of all available frames for each galaxy and in each filter to within ±0.1 pixel. This step was performed by measuring centroids for foreground stars on the images and then performing geometric transformations using the *geomap* and *geotran* tasks in IRAF.

[1] The IRAF package is written and supported by the IRAF programming group at the National Optical Astronomy Observatories (NOAO) in Tucson, Arizona. NOAO is operated by the Association of Universities for Research in Astronomy (AURA), Inc. under cooperative agreement with the National Science Foundation (NSF).

Table 1. Journal of observations.

CIG	B	$\langle B\rangle_{\rm FWHM}$	V	$\langle V\rangle_{\rm FWHM}$	R	$\langle R\rangle_{\rm FWHM}$	I	$\langle I\rangle_{\rm FWHM}$
CIG 72	1 × 1200	1.8	1 × 600	1.6	1 × 300	1.5	1 × 300	1.6
CIG 89	3 × 900	2.4	3 × 240	2.4	3 × 120	2.4	3 × 90	2.3
CIG 103	4 × 600	2.5	1 × 600	2.3	2 × 300	2.4	1 × 300	2.3
CIG 109	1 × 1200	1.8	1 × 600	1.8	1 × 300	1.6	1 × 300	1.5
CIG 135	1 × 1200	2.6	1 × 600	2.5	2 × 600	2.5	1 × 300	2.1
CIG 145	1 × 1200	1.7	1 × 900	1.7	1 × 420	1.6	1 × 300	1.6
CIG 156	2 × 600	1.9	2 × 300	1.7	2 × 180	1.7	2 × 120	1.6
CIG 191	1 × 1200	2.2	1 × 600	2.1	1 × 300	2.0	2 × 180	1.8
CIG 199	2 × 1200	1.9	2 × 600	1.8	2 × 300	1.7	2 × 300	1.6
CIG 309	1 × 1500	2.6	1 × 300	2.3	1 × 120	2.6	1 × 120	2.8
CIG 314	2 × 1500	2.4	1 × 600	2.3	1 × 420	2.5	1 × 420	2.1
CIG 392	1 × 1200	1.8	1 × 600	1.8	1 × 300	1.7	2 × 180	1.5
CIG 448	1 × 1200	2.1	1 × 600	2.2	1 × 300	1.9	2 × 180	1.9
CIG 477	1 × 1200	2.1	2 × 480	2.0	1 × 150	1.9	2 × 60	1.8
CIG 491	1 × 1200	1.5	1 × 900	1.6	1 × 300	1.5	1 × 300	1.5
CIG 500	1 × 1200	2.1	1 × 900	2.1	1 × 300	2.1	1 × 300	2.2
CIG 507	2 × 1200	2.1	2 × 600	2.1	2 × 300	2.0	2 × 300	1.9
CIG 512	2 × 1200	2.3	1 × 900	2.1	1 × 600	2.2	1 × 600	2.1
CIG 525	1 × 1200	2.0	2 × 600	1.9	2 × 300	1.8	2 × 300	1.7
CIG 539	1 × 1200	2.0	1 × 600	2.1	1 × 300	2.0	1 × 300	2.2
CIG 547	2 × 1200	2.4	1 × 900	1.9	1 × 600	1.9	1 × 600	1.8
CIG 575	1 × 1200	2.1	1 × 600	2.0	1 × 300	2.0	1 × 300	1.7
CIG 616	1 × 1200	2.0	2 × 600	2.0	1 × 480	2.0	1 × 300	1.8
CIG 624	1 × 900	1.5	1 × 600	1.8	1 × 300	1.7	1 × 300	1.8
CIG 630	1 × 1200	1.8	1 × 900	1.7	1 × 300	1.7	1 × 300	1.5
CIG 631	1 × 1200	1.7	1 × 600	1.6	1 × 300	1.6	1 × 300	1.5
CIG 712	1 × 1200	1.7	3 × 600	1.6	2 × 150	1.6	1 × 150	1.6
CIG 716	1 × 1200	2.4	1 × 600	2.2	2 × 150	2.1	2 × 150	1.9
CIG 744	1 × 1200	2.4	2 × 600	2.4	2 × 300	2.3	2 × 600	1.9
CIG 766	1 × 1200	2.3	1 × 600	2.3	1 × 300	2.0	1 × 300	1.7
CIG 772	1 × 1200	2.1	1 × 600	1.9	1 × 300	1.9	1 × 300	1.7
CIG 800	1 × 1200	1.9	1 × 900	1.7	1 × 300	1.8	1 × 300	1.7
CIG 805	1 × 1200	2.1	1 × 900	2.3	1 × 300	2.3	1 × 300	2.0
CIG 812	1 × 1200	2.3	1 × 600	2.4	1 × 300	2.5	1 × 300	2.3
CIG 838	1 × 1200	1.6	1 × 600	1.4	1 × 300	1.4	1 × 300	1.4
CIG 840	1 × 1200	1.8	2 × 300	2.0	2 × 150	1.9	2 × 150	1.6
CIG 858	1 × 1200	1.9	1 × 600	1.8	1 × 480	1.8	1 × 420	1.6
CIG 861	1 × 1200	2.2	1 × 600	2.2	1 × 300	2.1	1 × 300	1.9
CIG 862	1 × 1200	1.8	1 × 600	1.7	1 × 300	1.6	1 × 300	1.5
CIG 947	1 × 2400	1.7	1 × 1500	1.7	1 × 600	1.8	1 × 300	2.4

2.3. Errors

Apparent magnitudes for each galaxy were estimated in three concentric circular apertures. This was achieved in the *BVRI* bands by using the *phot* routines in IRAF. Here we report the total apparent magnitudes at the larger aperture, while in Appendix A we report apparent magnitudes at two other circular apertures, also in the *BVRI* bands (see Table A.1 in Appendix A).

An estimation of the errors in our photometry involves two parts: (1) the procedures to obtain instrumental magnitudes, and (2) the uncertainty when such instrumental magnitudes are transformed to the standard system.

For item 1, our estimate of the errors is mainly concerned with extinction corrections and the airmass terms. After a least-squares fit, the associated errors of the slope for each principal extinction coefficient are $\delta(k_B) \sim 0.031$, $\delta(k_V) \sim 0.022$, $\delta(k_R) \sim 0.025$ and $\delta(k_I) \sim 0.034$. An additional error δ(airmass) ~ 0.01 from the airmass routines in IRAF was also considered. For item 2, the zero point and first-order color terms are the most important to consider. The errors from the assumed relations for α and β were, 0.03, 0.03, 0.02, 0.03 and 0.02, 0.02, 0.04, 0.04 in B, V, R and I, respectively.

To estimate the total error in each band, it is necessary to propagate the above quoted errors according to the corresponding transformation equations. An additional estimate of the sky contribution is also necessary. This was achieved by estimating local and more general 2-D sky values on the images. Typical values $\delta(B) \sim 0.10$, $\delta(V) \sim 0.10$, $\delta(R) \sim 0.08$, and $\delta(I) \sim 0.10$ are obtained. Total typical uncertainties are 0.14, 0.12, 0.11, and 0.16 in the B, V, R, and I bands, respectively.

2.3.1. Isolated galaxies

Figure 1 shows a comparison of the estimated apparent magnitudes for the isolated galaxies in the B, V, R and I bands versus the corresponding values from similar aperture photometry when available in the HyperLeda database. An interpolation between adjacent aperture values was estimated when necessary.

We find a reasonable agreement with the available magnitudes from the literature, except for CIG 624, as shown in Fig. 1. We notice that the apparent diameter of this galaxy is larger than the CCD image size, difficulting a reliable estimate of the sky, thus causing an overestimation of the total magnitude at a similar aperture. A least square fit to the data in Fig. 1 shows rms

Table 2. General data for the observed isolated spiral galaxies.

CIG	ID	m_B mag (LEDA)	Type (LEDA)	m_B mag (NED)	$V_{\rm Rad}$ (km s^{-1})
CIG 72	UGC 01395	14.337	Sb	14.18	5150.9
CIG 89	NGC 0821	11.753	E	11.67	1747.6
CIG 103	NGC 0918	13.071	Sc	13.05	1536.2
CIG 109	NGC 0949	12.481	Sb	12.40	732.7
CIG 135	NGC 1474	14.842	Sa	14.66	5198.5
CIG 145	NGC 1542	14.858	Sab	14.83	3693.5
CIG 156	UGC 03258	13.733	SBab	13.98	2744
CIG 191	UGC 03863	14.202	SBa	14.01	6084.7
CIG 199	UGC 03944	14.968	Sc	14.60	4016.8
CIG 309	NGC 2775	11.143	Sab	11.03	1346.3
CIG 314	NGC 2776	12.204	SABc	12.14	2797.3
CIG 392	PGC 029147	14.755	Sbc	14.99	7612.4
CIG 448	NGC 3437	12.532	SABc	12.75	1379.7
CIG 477	NGC 3655	12.317	Sc	12.30	1525.4
CIG 491	UGC 06608	14.318	SABa	14.23	6246.2
CIG 500	UGC 06771	14.452	Sab	13.60	6001.5
CIG 507	UGC 06847	14.988	Sbc	14.97	5072.6
CIG 512	UGC 06903	13.929	Sc	13.00	1915.8
CIG 525	UGC 07416	13.791	Sb	13.78	7106.9
CIG 539	NGC 4566	13.962	Sbc	13.87	5590.4
CIG 547	NGC 4635	13.271	SABc	13.20	1083.9
CIG 575	NGC 5016	13.37	SABb	13.49	2761.1
CIG 616	UGC 09088	14.445	SO-a	14.40	6452.5
CIG 624	NGC 5585	11.391	SABc	11.20	573.2
CIG 630	NGC 5622	13.981	Sb	13.99	4122.6
CIG 631	NGC 5633	13.109	Sb	13.06	2581
CIG 712	NGC 6012	12.871	SBab	12.96	2004.2
CIG 716	UGC 10104	14.336	Sc	14.26	10 056.2
CIG 744	UGC 10437	15.107	Sc	14.70	2854.1
CIG 766	NGC 6207	11.857	Sc	12.16	1090.3
CIG 772	IC 1231	13.692	Sc	13.59	5538.9
CIG 800	NGC 6347	14.404	SBb	14.47	6307.9
CIG 805	IC 1256	14.189	Sb	14.00	4937.8
CIG 812	NGC 6389	12.839	Sbc	12.82	3281.5
CIG 838	IC 1269	13.428	Sbc	13.40	6296
CIG 840	UGC 11058	13.476	Sb	13.29	4977.6
CIG 858	NGC 6695	14.314	SBb	14.28	5734.7
CIG 861	UGC 11352	15.324	SBbc	15.29	6894.1
CIG 862	NGC 6711	13.715	Sbc	13.70	4929.6
CIG 947	NGC 7217	11.033	Sab	11.02	1118.2

errors of 0.13, 0.15, 0.06 and 0.07 mag in the B, V, R and I bands respectively, in close agreement with our total errors above estimated. Additional magnitudes at two other concentric circular apertures in B, V, R, and I for all the isolated galaxies in this study are reported in the Appendix A. A logarithmic aperture size in 0.1′ units was adopted according to the HyperLeda convention.

3. Magnitudes and colors

The estimated apparent magnitudes and the colors of the galaxies in the sample are presented in Table 3. Entries are as follows: Col. (1) gives the CIG number, Col. (2) gives the logarithmic aperture size in 0.1′ units as defined in HyperLeda, and Cols. (3)–(6) give the observed integrated apparent magnitudes in the B, V, R, and I bands. Finally, Cols. (7)–(9) give the observed $(B-V)$, $(B-R)$, and $(B-I)$ color indices.

The fraction of dust seems to be higher for bigger galaxies, according to empirical (e.g., Giovanelli et al. 1995; Wang & Heckman 1996; Tully et al. 1998) and theoretical (e.g., Shustov et al. 1997) arguments. Therefore, the internal extinction correction should depend not only on inclination but also on galaxy scale: $A^{\rm i}_{\lambda}[\rm mag] = \gamma_{\lambda} \log(a/b)$, where a/b is the major-to-minor axis ratio, and γ_{λ} is a scale-dependent coefficient in the given passband λ. From an empirical analysis, Tully et al. (1998) inferred the coefficients γ_{λ} in the *BRIK* bands as a function of the galaxy maximum circular velocity. From their data (given in Tully & Pierce 2000) we have carried out linear correlations of these coefficients with the corresponding magnitudes *not corrected* for internal extinction:

$$\begin{aligned}
\gamma_B[\rm mag] &= -6.30 - 0.40 M_B, \quad M_B < -16.7,\\
\gamma_R[\rm mag] &= -4.20 - 0.26 M_B, \quad M_R < -17.7,\\
\gamma_I[\rm mag] &= -3.40 - 0.20 M_I, \quad M_I < -18.0,\\
\gamma_K[\rm mag] &= -0.85 - 0.05 M_K, \quad M_K < -19.7.
\end{aligned} \tag{2}$$

For values of the magnitudes higher than the limits given in Eq. (2), γ_{λ} is assumed to be 0 (no extinction correction). For band V, the line coefficients of γ_V were obtained by a simple

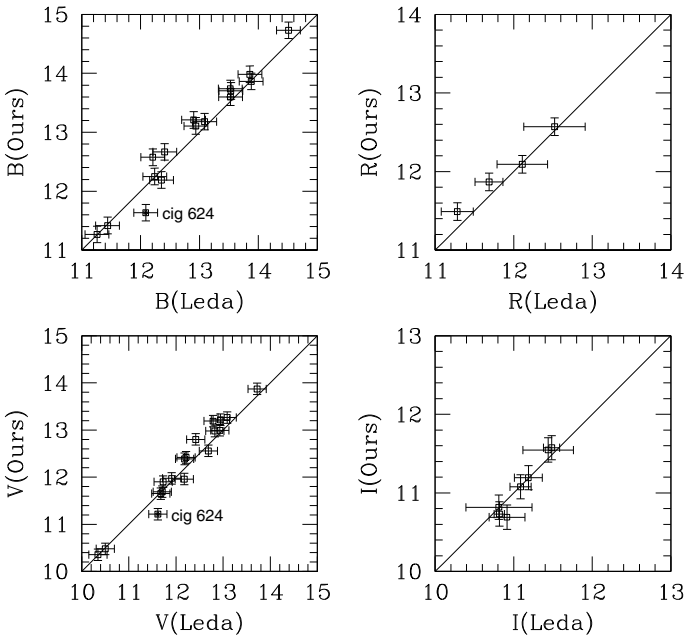

Fig. 1. Comparison between our total B, V, R and I apparent magnitudes and the available photometry of similar aperture from the HyperLeda Database. A discrepant case (CIG 624) is indicated.

interpolation of those in bands B, R, I, and K: $\gamma_V[\mathrm{mag}] = -4.67 - 0.29M_V$, $M_V < -17.5$. The a/b ratios estimated at the B-band 25 mag/arcsec^2 isophote were taken from the HyperLeda database.

Table 4 shows foreground – and internal – extinction-corrected color indices and absolute magnitudes. Corrections are based on data generated from the dust galaxy maps given in Schlegel et al. (1998) and available in NED. Entries are as follows: Col. (1) gives the identification CIG number, Cols. (2)–(4) give the corrected $(B-V)$, $(B-R)$, and $(B-I)$ color indices. Finally, Cols. (5)–(8) report the corrected absolute magnitudes in the B, V, R, and I bands. A Hubble constant value of 70 km s^{-1} Mpc^{-1} was adopted.

The $(B-V)$-corrected colors span the range of 0.15−1.0 mag, comparable to that reported in de Jong (1996), Verheijen (1997) and more recently Hernández-Toledo et al. (2007). A more physical correction applied to the luminosities yields a B-band luminosity range ($-17.5 \leq M_B \leq -22.05$), indicating no faint spirals in this sample, except perhaps for the case of CIG 547.

In Fig. 2 we plot different extinction-corrected color-magnitude diagrams (M_R vs. $(B-V)$,$(B-R)$, and $(B-I)$ colors) for our sample of isolated galaxies. We find a loose correlation of colors with magnitude. Some authors (e.g., Avila-Reese & Firmani 2000) have stated that a significant dependence of color on luminosity for normal isolated disks is not expected.

4. Optical and near-infrared (NIR) morphology

To discuss the optical morphology we present an image processing scheme that enhances high/low surface brightness morphological components in galaxies. For each isolated galaxy, a mosaic like the one shown in Fig. 3 is presented. Each mosaic includes, from top-left to bottom-right, (1) a logarithmic gray scale R-band image to look for both internal and external details; (2) an R-band filter-enhanced image to look for internal structure in the form of star-forming regions and/or structure embedded in dusty regions (the filtering-enhancing techniques Sofue 1993, allow to subtract the diffuse background in a convenient way for discussing the different morphological details); (3) a $(B-I)$ color index map to visualize the spatial distribution of dusty and SF regions (light-gray is for blue colors, while dark-gray is for red colors); (4) a composed (filter-enhanced) NIR *JHK* image which is a combination of the archived J-, H-, and K-band images from 2MASS (Skrutskie et al. 2006) to complement the structural and morphological analysis. At the far right, (5) the ellipticity ϵ and position angle (PA) radial profiles from the R and composed *JHK* images to provide evidence of the presence of some structural components like bars, rings and other features. Finally (6), an *RGB* image from the SDSS database is included (when available) to visualize the color distribution of the different structural components in these galaxies and at the same time to have a wider view of their local environment. This is usefull to identify possible dwarf galaxies interacting with CIG objects but that are not visible in our narrow optical images. The *RGB* images allow us either to explore the close environment of an isolated galaxy (see square symbols on the *RGB* images indicating a few objects identified as galaxies, according to SDSS) or take a look at the spatial distribution of different stellar populations, dust lanes and SF regions, according to their color distribution. Notice that there is no radial velocity information for those objects identified as galaxies and that we do not pretend to give an exhaustive list of such objects (see Verley et al. 2007).

We identify a bar signature if the ellipticity radial profile ϵ rises to a maximum ϵ_{max} required to be above that of the outer disk, while the PA radial profile shows a plateau (within ±20°) along the bar (Wozniak et al. 1995).

All the images are oriented according to the standard (north-east) astronomical convention. The NIR images are approximately at the same scale as the optical images. For the sake of not crowding, the major diameter (in arcmin) of the optical images is specified in the caption for each galaxy. In some cases, not all the foreground stars in each field have been removed.

In the following discussion, we use the fact that the median value of the $(B-V)$ color declines systematically as the morphological type T increases along the morphological sequence (Roberts & Haynes 1994).

4.1. Comments on individual objects

CIG 72. The galaxy was previously classified as SA(rs)b Sy1.9 by NED. In the composed *JHK* and the optical filter-enhanced images we find evidence of a bar structure, as well as an inner ring. The $B-V$ color index corresponds to those for Sa/Sab types. The geometric profiles confirm the presence of a bar structure at a radius of approx. 16 arcsec. We classify this object as SB(r)b. Notice the degree of global asymmetry. This object has been flagged as possibly interacting by Sulentic et al. (2006). We notice an asymmetric pattern in the arms.

CIG 89. NED reports this galaxy as E6? In the optical and NIR images we see a disk structure. The whole disk shows uniform colors in the $B-I$ color map. The total $B-V$ color index is similar to the S0a/Sa types. Our classification for this galaxy is S0.

CIG 103. According to NED this is a SAB(rs)c galaxy. The filter-enhanced images show evidence of an ovally-shaped bulge region. The $B-V$ color index is representative of the Scd-Sd types. The geometric profile in both the *JHK* and R bands show weak evidence of a bar in the first 10 arcsec. We classify this galaxy as SAB(r)cd.

Table 3. Apparent magnitudes and color indices.

CIG	Log (A)	B	V	R	I	$B-V$	$B-R$	$B-I$
CIG 72	1.181	14.449	13.619	13.090	12.381	0.830	1.359	2.068
CIG 89	1.385	12.210	11.310	10.739	9.744	0.900	1.470	2.466
CIG 103	1.497	13.359	12.440	11.811	11.078	0.919	1.548	2.280
CIG 109	1.376	12.667	11.975	11.490	10.790	0.691	1.177	1.876
CIG 135	1.223	14.662	13.762	13.190	12.419	0.900	1.472	2.244
CIG 145	1.284	15.020	13.886	13.228	12.363	1.134	1.792	2.657
CIG 156	1.102	13.597	12.967	12.520	11.812	0.630	1.078	1.786
CIG 191	1.223	14.497	13.481	13.327	11.922	1.016	1.170	2.575
CIG 199	1.327	14.481	13.889	13.424	12.761	0.592	1.057	1.720
CIG 309	1.403	11.417	10.481	9.920	8.994	0.936	1.497	2.422
CIG 314	1.591	12.249	11.693	11.285	...	0.555	0.963	...
CIG 392	1.102	14.952	14.077	13.544	12.833	0.875	1.408	2.119
CIG 448	1.482	12.575	11.961	11.474	10.818	0.614	1.101	1.758
CIG 477	1.306	12.575	11.904	11.366	10.732	0.671	1.210	1.844
CIG 491	1.066	14.602	13.915	13.411	12.776	0.687	1.191	1.826
CIG 500	1.272	13.911	13.018	12.471	11.812	0.893	1.440	2.099
CIG 507	1.306	15.299	14.698	14.206	13.386	0.601	1.093	1.913
CIG 512	1.428	13.623	13.011	12.508	11.890	0.613	1.115	1.733
CIG 525	1.248	13.863	13.190	12.673	12.059	0.673	1.190	1.805
CIG 539	1.248	14.171	13.307	12.774	12.094	0.864	1.397	2.077
CIG 547	1.403	13.597	12.995	12.571	12.082	0.602	1.026	1.515
CIG 575	1.357	13.180	12.558	12.093	11.547	0.622	1.088	1.633
CIG 616	1.445	14.380	13.245	12.646	11.886	1.135	1.735	2.495
CIG 624	1.482	11.634	11.216	10.814	10.123	0.418	0.820	1.512
CIG 630	1.385	14.105	13.440	12.948	12.412	0.665	1.157	1.693
CIG 631	1.357	13.176	12.932	12.449	11.575	0.244	0.727	1.601
CIG 712	1.357	13.209	12.420	11.870	11.195	0.789	1.339	2.013
CIG 716	1.181	14.730	13.874	13.344	12.636	0.856	1.387	2.094
CIG 744	1.428	14.550	14.045	13.686	13.193	0.505	0.864	1.357
CIG 766	1.357	12.189	11.651	11.240	10.691	0.538	0.949	1.497
CIG 772	1.403	13.846	13.203	12.705	12.175	0.643	1.141	1.672
CIG 800	1.223	14.263	13.450	12.890	12.218	0.813	1.373	2.045
CIG 805	1.248	14.297	13.551	13.022	12.434	0.746	1.275	1.863
CIG 812	1.445	13.107	12.389	11.848	11.211	0.718	1.259	1.896
CIG 838	1.338	14.026	13.218	12.709	12.189	0.808	1.317	1.837
CIG 840	1.306	13.701	12.981	12.462	11.909	0.720	1.240	1.792
CIG 858	1.248	14.374	13.493	12.917	12.226	0.881	1.457	2.148
CIG 861	1.181	15.428	14.685	14.190	13.590	0.743	1.237	1.838
CIG 862	1.223	13.984	13.267	12.735	12.222	0.718	1.249	1.763
CIG 947	1.489	11.265	10.355	...	...	0.910	...	...

CIG 109. NED classified this galaxy as SA(rs)b. The geometric profiles resemble a bar but a careful examination of our images indicate that two strong knots at opposite sides in the bulge region produce an almost constant PA. The $B-V$ color index is representative of Sbc-Sc types. The $B-I$ color map shows a central region with a mixture of dust and SF regions, and also evidence of an outer and smoother structure (arms?). We classify this object as (R)SA(s)ab.

CIG 135. NED classification for this galaxy is SBa. The composed *JHK* image shows evidence of a bar and an inner ring more clearly than the optical filter-enhanced one. The outer arms are fragmented, resembling tidal disturbances. The $B-V$ color index is representative of the Sab/Sb types. We classify this galaxy as SB(r)ab. This object has been flagged as possibly interacting by Sulentic et al. (2006).

CIG 145. According to NED this is a Sab galaxy. In spite of the high inclination, the *R* band filter-enhanced image show a prominent dust lane and a structure that resembles an arm. The $B-V$ color index is probably reddened and is characteristic of the S0a/Sa types. We classify this galaxy as Sa.

CIG 156. The NED classification for this galaxy is SB(r)ab pec. The optical and near-infrared images as well as the geometric profiles show a strong bar. The shape of the arms resembles an outer ring. The $B-I$ color map shows that in general the galaxy has blue colors, except in the nuclear region where it is reddened. The $B-V$ color is consistent with the Sbc/Sc types. We classify this object as (R)SBbc. This object has been flagged as possibly interacting by Sulentic et al. (2006).

CIG 191. The NED classification for this object is (R′)SBa. We observe a bar structure in the filter-enhanced images. The $B-V$ color index is representative of S0a/Sa galaxies. The geometric profiles also confirm the existence of a bar in both *R* and *JHK* filter-enhanced images. We classify this galaxy as (R)SBa.

CIG 199. NED reports this object as Scd. The optical and filter-enhanced images show a set of clumpy and blue arms. The *R* filter-enhanced image as well as the geometric profiles show weak evidence of an inner bar. The *RGB* color image shows something similar to an inner pseudo-ring and makes more evident the fragmentation of the outer arms. The squares show the position of three objects classified as galaxies in the field of CIG 199. The $B-V$ color index is representative of the Sm/Im types. We classify this galaxy as SAB(r)cd.

CIG 309. The NED classification for this galaxy is SA(r)ab. Tight arms with strong inner star forming regions and dust lanes

Table 4. Corrected colors and absolute magnitudes.

CIG	$(B-V)_c$	$(B-R)_c$	$(B-I)_c$	M_B	M_V	M_R	M_I
CIG 72	0.689	1.170	1.766	–20.496	–21.185	–21.665	–22.261
CIG 89	0.763	1.264	2.157	–20.371	–21.135	–21.636	–22.529
CIG 103	0.471	0.877	1.270	–20.241	–20.712	–21.118	–21.511
CIG 109	0.588	1.054	1.657	–17.890	–18.478	–18.944	–19.547
CIG 135	0.648	1.094	1.674	–20.777	–21.425	–21.871	–22.451
CIG 145	0.797	1.332	1.898	–20.190	–20.987	–21.522	–22.088
CIG 156	0.519	0.922	1.548	–19.826	–20.346	–20.749	–21.375
CIG 191	0.793	0.842	2.101	–21.214	–22.007	–22.056	–23.315
CIG 199	0.370	0.799	1.293	–20.192	–20.563	–20.992	–21.486
CIG 309	0.854	1.389	2.249	–20.377	–21.231	–21.765	–22.626
CIG 314	0.345	0.730	...	–21.569	–21.914	–22.300	...
CIG 392	0.820	1.346	2.008	–20.487	–21.307	–21.833	–22.495
CIG 448	0.450	0.941	1.457	–19.576	–20.026	–20.518	–21.033
CIG 477	0.593	1.121	1.688	–19.446	–20.038	–20.567	–21.134
CIG 491	0.588	1.081	1.635	–20.566	–21.154	–21.648	–22.201
CIG 500	0.613	1.136	1.541	–22.043	–22.656	–23.179	–23.584
CIG 507	0.403	0.900	1.572	–19.807	–20.210	–20.707	–21.379
CIG 512	0.568	1.062	1.643	–18.747	–19.315	–19.810	–20.390
CIG 525	0.586	1.086	1.635	–21.523	–22.109	–22.609	–23.158
CIG 539	0.778	1.298	1.901	–20.732	–21.510	–22.029	–22.633
CIG 547	0.554	0.970	1.410	–17.568	–18.122	–18.538	–18.978
CIG 575	0.552	1.008	1.496	–20.094	–20.646	–21.102	–21.589
CIG 616	0.985	1.578	2.168	–21.292	–22.277	–22.870	–23.461
CIG 624	0.347	0.750	1.388	–18.191	–18.538	–18.940	–19.578
CIG 630	0.540	1.021	1.449	–20.260	–20.800	–21.281	–21.709
CIG 631	0.127	0.604	1.415	–20.047	–20.174	–20.651	–21.463
CIG 712	0.710	1.243	1.847	–19.433	–20.143	–20.676	–21.280
CIG 716	0.776	1.280	1.925	–21.405	–22.181	–22.685	–23.330
CIG 744	0.471	0.825	1.288	–18.637	–19.108	–19.462	–19.925
CIG 766	0.408	0.819	1.256	–19.280	–19.689	–20.099	–20.537
CIG 772	0.461	0.945	1.327	–21.381	–21.841	–22.326	–22.707
CIG 800	0.591	1.097	1.591	–21.460	–22.050	–22.557	–23.051
CIG 805	0.613	1.111	1.589	–20.514	–21.128	–21.625	–22.103
CIG 812	0.539	1.015	1.516	–20.991	–21.530	–22.006	–22.507
CIG 838	0.631	1.076	1.453	–21.499	–22.130	–22.575	–22.952
CIG 840	0.604	1.090	1.552	–21.043	–21.647	–22.134	–22.595
CIG 858	0.716	1.245	1.798	–20.925	–21.641	–22.171	–22.723
CIG 861	0.543	0.993	1.425	–20.392	–20.935	–21.386	–21.817
CIG 862	0.616	1.097	1.533	–20.686	–21.301	–21.783	–22.219
CIG 947	0.796	...	...	–20.251	–21.048	...	...

can be appreciated forming a ring that encloses a uniformly redder and soft bulge. Our optical images as well as the *RGB* color image show how the spatial distribution of the inner star forming regions and dust lanes trace the arms. A few small galaxies (square symbols) can be appreciated in the neighborhood of this galaxy. The total $B-V$ color index is representative of the E/S0 types. We classify this galaxy as SA(r)a.

CIG 314. NED classifies this galaxy as SAB(rs)c. A set of multiple fragmented arms with star formation and blue colors can be seen in our optical images as well as in the color image from SDSS, while the central region appears redder. The composed *JHK* image shows an inner ring, and this is also appreciated from the corresponding geometric profiles. A few dwarf galaxies (square symbols) are indicated in the *RGB* image. The total $B-V$ color index is similar to the Sm/Im types. Our classification for this galaxy is SA(r)d.

CIG 392. NED classifies this galaxy as S0. The logarithmic, filter-enhanced *R* band and *RGB* images show a pair of tightly wounded arms, an elongated central region and an inner ring that appears blue in the $B-I$ color map and the *RGB* image. The composed *JHK* image gives strong evidence about the bar and the ring, confirmed by the geometric profiles. The total $B-V$ color index is representative of the S0a/Sa types. We classify this galaxy as SB(r)a. Notice a filamentary structure coming out of the ring in the southern part.

CIG 448. The NED classification for this object is SAB(rs)c. This inclined galaxy shows a set of multiple and clumpy arms that appear blue in both the $B-I$ color map and the *RGB* image. These images also allow to appreciate dust lanes along the disk. Notice how the bulge region is emphasized in the *RGB* and *JHK* images. Contrary to the optical images, the *JHK* image shows two main arms and weak evidence of a bar, instead. A few dim galaxies are appreciated in the neighborhood. The total $B-V$ color index is intermediate between the Scd/Sd and the Sm/Im types. We classify this galaxy as SABc.

CIG 477. SA(s)c HII is the classification reported by NED. While our optical and the *RGB* images show a multiple and fragmented set of arms with a small bulge, the near-infrared image describes three arms and a slightly more prominent bulge. A field star near the center is masking some details inside that region. There is a faint dwarf galaxy in the field, from the SDSS image. The total $B-V$ color index is intermediate between Sab/Sb and Sbc/Sc types. We classify this galaxy as Sc.

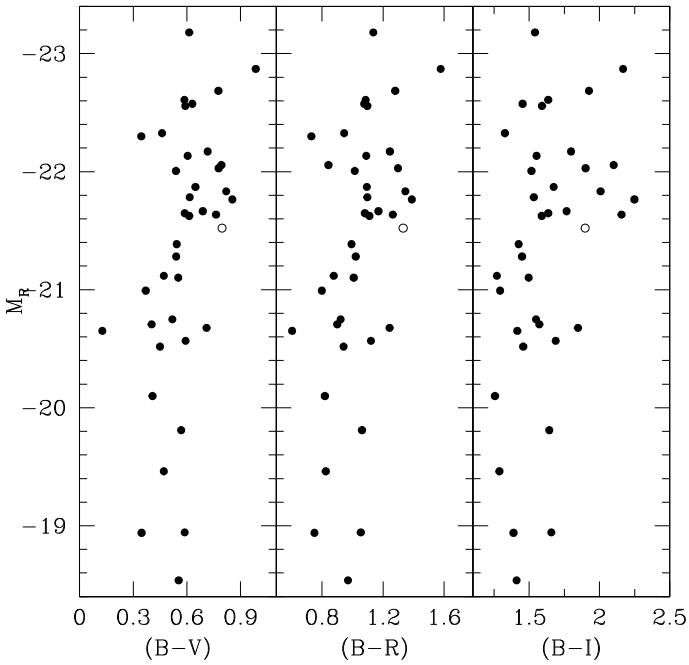

Fig. 2. Color-magnitude diagrams for the 40 isolated spirals after galactic and internal extinction corrections. Galaxies with inclination higher than 80° are shown with (open) circles.

CIG 491. The NED classification for this galaxy is SAB(r)ab? This galaxy shows a set of multiple and fragmented arms as well as an apparent inner ring, as seen in the *R* filter-enhanced image. Although the *R* filter-enhanced image seems to show an ovally-distorted central region, neither the composed *JHK* image nor its corresponding geometric profile confirm this. There is no information in the image from SDSS about faint galaxies close to CIG 491. The total $B-V$ color is similar to the Sbc/Sc types. SABc(r) is our classification for this object.

CIG 500. NED reports this galaxy as (R')SAB(r)ab. A well-defined bar encircled by a ring structure is shown in the optical, *JHK* and *RGB* images. The arms appear to emerge from the opposite sides of the bar. From the *RGB* image, a few dwarf galaxies can be seen projected along the face of this galaxy. The total $B-V$ color index corresponds to the Sa/Sab types. We classify this galaxy as SB(r)b.

CIG 507. NED reports this galaxy as Sbc. Although this is a highly inclined galaxy, the optical and *RGB* images show blue, fragmented and clumpy arms and a non-prominent bulge. The composed *JHK* image shows an elongated central region, and the geometric profiles resemble a large-scale bar-like structure. If not due to projection effects, this may be suggesting the presence of a bar. There are several dwarf galaxies identified in the image from SDSS. The total $B-V$ color index is similar to the Sm/Im types. We classify this galaxy as SABcd. This object has been flagged as possibly interacting by Sulentic et al. (2006).

CIG 512. According to NED this is a SB(s)cd galaxy. A pair of arms emerge from opposite sides of a bar. These arms become fragmented and clumpy in the outer regions, as can be seen in the optical images and more clearly in the image from SDSS. Notice the blue color of the bar in the $B-I$ color map and the *RGB* image. The image from SDSS also shows some faint galaxies. The total $B-V$ color index is characteristic of the Sbc/Sc types. SBcd is our classification for this galaxy.

CIG 525. NED reports this object as SB(r)b. A symmetric multi-arm spiral pattern is seen emerging from opposite sides of a bar. Both the ring and the bar are confirmed by the geometric profiles, the *JHK* and the *RGB* images. We also notice two dwarf galaxy candidates at the end of the north-east set of arms in the optical images, but the image from SDSS only identifies one. The total $B-V$ color index is similar to the Sbc/Sc types. Our classification for this galaxy is SB(r)bc.

CIG 539. NED reports this object as Sb. A set of two tightly wounded arms forming a ring are appreciated in all of the images. In contrast to the *RGB* image, the diffuse outskirts are only seen in our optical images, illustrating their deeper nature. The *R*-band filter-enhanced and *JHK* images show clear evidence of a slightly twisted bar. The *RGB* image shows 3 dwarf galaxies in the field. The total $B-V$ color index is characteristic of the S0a/Sa types. We classify this galaxy as SB(r)ab. This object has been flagged as possibly interacting by Sulentic et al. (2006).

CIG 547. The NED classification for this galaxy is SAB(s)d. Two adjacent bright knots near the central region may give the appearance of an ovally-distorted region. However, from our images and profiles there is no evidence of a bar-like structure. Both the *R* band filter-enhanced and the *RGB* image shows a pattern of blue fragmented clumpy arms and strong dust lane structures. A couple of red faint galaxies are seen in the SDSS image at the south-west set of arms. The total $B-V$ color index is characteristic of the Sbc/Sc morphological types. We classify this galaxy as Sd.

CIG 575. This galaxy is reported by NED as SAB(rs)c SBNG. The optical images show a set of fragmented arms and only weak evidence of a bar. The geometric profiles and the *JHK* image confirm this, and the *RGB* image shows strong dust lane structures. From this image, there is no information about possible dwarf galaxies. The total $B-V$ color index is representative of the Sbc/Sc types. Our classification for this object is SABc.

CIG 616. NED reports this object as S0/a. This is a highly inclined galaxy. However the optical images show weak evidence of outer spiral blue arms as judged by the filter-enhanced and $B-I$ images, and a chain of SF regions at the south-west side. The optical filter-enhanced and composed *JHK* images show an inner region that resembles either a spiral pattern or a bar structure. There are a couple dim galaxies shown in the *RGB* image. The total $B-V$ color index is similar to the E/S0 types. We classify this galaxy as SABab.

CIG 624. SAB(s)d HII is the NED classification for this galaxy. A fragmented spiral arm pattern and regions of star formation all along the disk are appreciated both in our optical and *RGB* images. The total $B-V$ color index is similar to the Sm/Im types. SABdm is our classification for this galaxy. Note that the angular scale of this galaxy is larger than our CCD size (5.8 arcmin). However a wider view from the SDSS image allows us to barely identify the global spiral and fragmented pattern, and a few dwarf galaxies (green boxes) at the outskirts.

CIG 630. The NED classification for this object is Sb. Both the *R* band filter-enhanced and the *RGB* images show two well-defined symmetric arms spiraling twice around the central region. There is no evidence of a bar. Two faint galaxies are identified in the image from SDSS, one of them apparently over an arm of CIG 630. The $B-V$ total color index is representative of the Sbc/Sc types. We classify this galaxy as SA(rs)bc.

CIG 631. (R)SA(rs)b is the NED classification for this object. A couple of tight arms emerge from the central region forming an apparent ring. These arms appear fragmented in the inner region and become smoother towards the external parts. The apparent ring is clearly seen in the *RGB* and composed *JHK* images, and also confirmed by the geometric profiles. The image

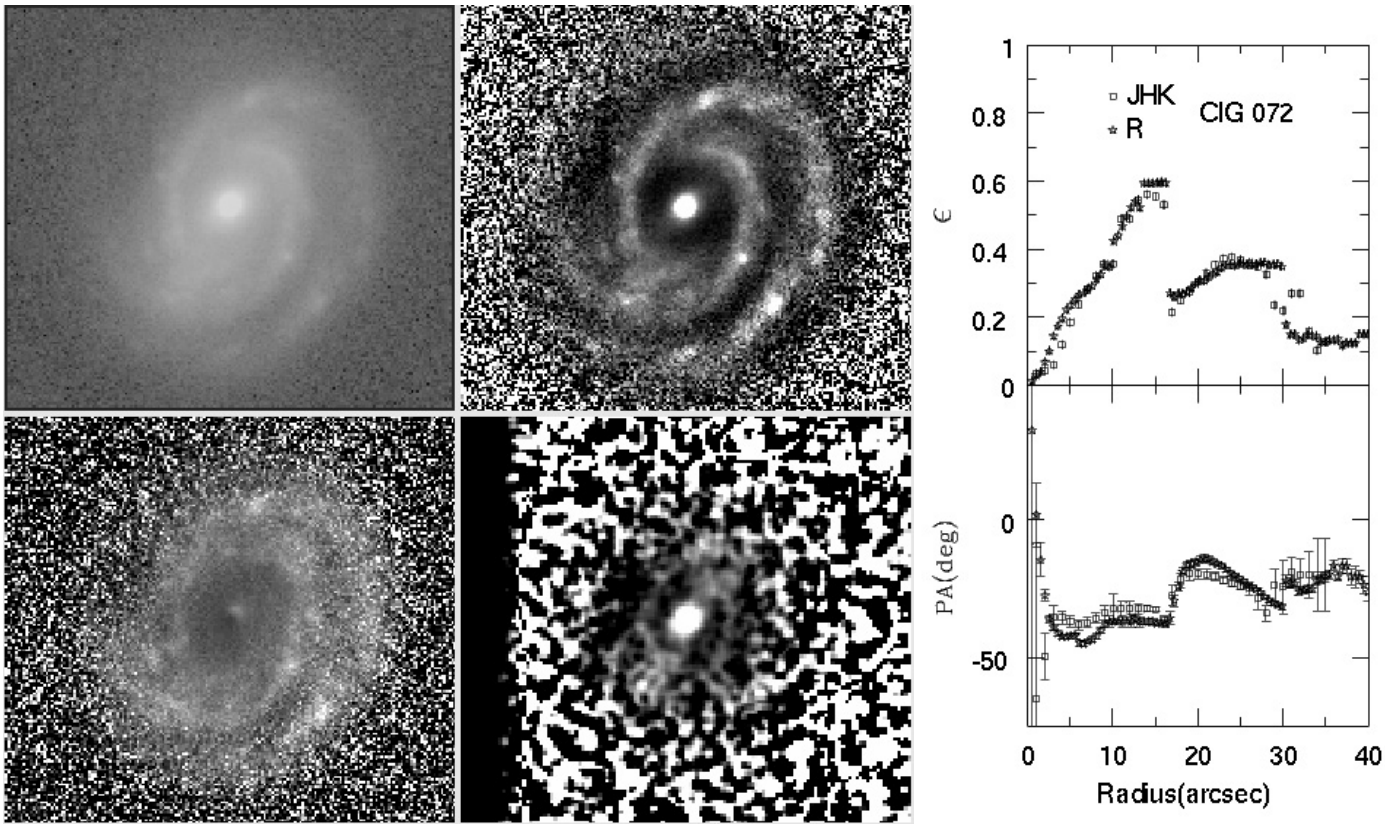

Fig. 3. CIG 72 Mosaic. *Upper-left*: a gray scale *R*-band image displayed in logarithmic scale. *Upper-right*: an *R* band filter-enhanced image. *Lower-left*: a $(B-I)$ color index map. *Lower-right*: a composed (filter-enhanced) NIR *JHK* image. *Right-most panel*: the photometric ϵ and PA radial profiles from the *R*-band and composed *JHK*-band images. Images are oriented according to the astronomical convention. The major diameter of the galaxy in the optical images is 1.3 arcmin.

from SDSS gives no information about possible dwarf galaxies. The total $B-V$ color index is similar to the Sm/Im types. We classify this galaxy as SA(r)bc.

CIG 712. This object is reported as (R)SB(r)ab: LINER by NED. The optical, *RGB* and near-infrared images show a strongly elongated inner ring along the bar and another round-shaped ring encircling the first. The geometric profiles confirm a large-scale bar and the rings. The inner ring shows blue $B-I$ colors. The optical images show evidence of a diffuse outer set of arms. The *RGB* image shows 5 galaxies in the field, and one of them, flagged with a "B", superposed on a bright star. The magnitudes in the SDSS *ugriz* system for "B" are 15.27, 13.76, 12.16, 14.80 and 13.68, respectively. The total $B-V$ color index is consistent with S0a/Sa and Sab/Sb types. We classify this galaxy as SB(r)b.

CIG 716. NED reports this object as SA(rs)bc. Two symmetric and continuous arms emerge from an inner ring. However this pattern becomes fragmented and strongly asymmetric in the outer regions. The absence of a clear underlying disk and their morphology, suggests a possible tidal origin of these pseudo-arms. Five dwarf galaxies can be appreciated in the image from SDSS. The total $B-V$ color index is characteristic of the S0a/Sa types. We classify this galaxy as SA(r)b.

CIG 744. NED reports this galaxy as Sc. Our optical and *RGB* images allow us to appreciate a set of 3 arms emerging from an inner ring that encloses a faint bulge, barely visible in the image from SDSS. Notice some filamentaty structurew emerging perpendicular to the north-west arm. There is no evidence of a bar either in the images or the geometric profiles. The total $B-V$ color index is representative of the Scd/Sd types. The image from SDSS shows several dwarf galaxies. We classify this galaxy as Sd. This object has been flagged as possibly interacting by Sulentic et al. (2006).

CIG 766. The NED classification for this galaxy is SA(s)c HII. A pattern of multiple, fragmented and dusty structures along the arms are shown above an underlying smooth disk in our optical and *RGB* images. In contrast, the near-infrared image shows evidence of a single inner spiral pattern that probably bifurcates outwards and also suggests for a elongated central region. A star close to the central region is masking some morphological details, as seen in the optical and *RGB* images, where 5 dwarf galaxies can be appreciated. The north-eastern arms appear brighter than their south-western contraparts. The total $B-V$ color index is characteristic of the Sm/Im types. SABcd is our classification for this galaxy.

CIG 772. NED reports this galaxy as Scd. A set of multiple arms that become fragmented in the outer regions can be seen in the optical images. The *R* band filter-enhanced image shows an s-shaped central region. We find no evidence of a bar in any of the images, and the geometric profiles confirm this. The total $B-V$ color index is similar to the Scd/Sd types. We classify this galaxy as SA(s)cd.

CIG 800. SBb is the NED classification for this galaxy. The optical images show two main blue arms that bifurcate outwards, with an s-shaped central region. The composed *JHK* image shows the main arms and a elongated central region suggested as a bar by the geometric profiles. The total $B-V$ color index corresponds to the Sab/Sb or Sbc/Sc types. We classify this galaxy as a SB(s)bc.

CIG 805. According to NED this is an Sb galaxy. An inner ring and two arms that bifurcate and become diffuse outwards are appreciated in the optical and *RGB* images. The composed *JHK* image reveals what might be interpreted as an ovally distorted central region, also seen in the *RGB* image, but there is not clear evidence of a bar in the geometric profiles. The image from SDSS shows some dwarf galaxies in the field. The total $B-V$ color index is representative of the Sab/Sb types. Our classification for this galaxy is SAB(rs)bc.

CIG 812. NED classifies this galaxy as Sbc. A set of multiple and fragmented arms that appear blue in the $B-I$ color map, are appreciated. An inner ring, confirmed in the geometric profiles, is also appreciated. The total $B-V$ color index is characteristic of the Sbc/Sc types. We classify this galaxy as SA(r)c.

CIG 838. This galaxy is reported as Sbc in NED. This is a clear case of a galaxy that appears multi-armed in the optical images, but that shows only two main arms in the near-infrared. We find evidence of a bar in the optical images that is confirmed by both the *JHK* image and the geometric profiles. The $B-I$ color map shows the two main arms forming a clumpy pseudo-ring. The total $B-V$ color index is similar to the Sab/Sb types. We classify this galaxy as SB(r)bc. Notice the apparently disturbed end of the arm at the west. This object has been flagged as possibly interacting by Sulentic et al. (2006).

CIG 840. The NED classification for this galaxy is SB(s)b. There are several field-stars. A pair of two main arms emerge from an inner ring. These arms become fragmented in the outer regions. The *R* band filter-enhanced image gives evidence of a bar, which is confirmed in the *JHK* image and the geometric profiles. The total $B-V$ color index is similar to the Sa/Sab types. We classify this galaxy as SB(r)bc.

CIG 858. NED reports this galaxy as SBb. Two prominent arms are shown in the optical images that appear blue in the $B-I$ color map. We find evidence of a bar in both the optical and the *JHK* images. This is reinforced by the geometric profiles. A dust lane dividing the southern arm into two components is evident in the optical images. The total $B-V$ color index is consistent with SOa/Sa and Sab/Sb types. We classify this galaxy as SBb.

CIG 861. The NED classification for this galaxy is SBbc. The optical images show two prominent arms and an elongated central region that is not aligned with the bar. The composed *JHK* image shows only the central region, and a bar that is confirmed by the geometric profiles. The total $B-V$ color index is representative of the Sbc/Sc types. Our classification for this galaxy is SBbc.

CIG 862. NED reports this galaxy as SBbc. A pair of arms emerging from the south side of a bar are appreciated in the optical images. In contrast, the *JHK* image shows the arms emerging from opposite sides of the bar. These arms become fragmented and clumpy in the outer regions. The geometric profiles confirm the bar. The total $B-V$ color index is similar to the Sab/Sb types. SBbc is our classification for this galaxy.

CIG 947. The NED classification for this galaxy is (R)SA(r)ab; Sy LINER. In the optical images we appreciate a tight spiral structure and a ring in the inner regions. The $B-I$ color map shows uniform colors inside, and redder colors in the arms. The total $B-V$ color index is similar to the S0a/Sa types. The composed *JHK* image shows a smooth central region. We classify this galaxy as SA(r)ab.

5. Optical morphology: results

Table 5 is a summary of the morphological results found in this work. Column (1) gives the CIG catalog number, Col. (2) gives the Hubble type as reported in NED, Col. (3) gives the Hubble type as estimated in this work, Col. (4) indicates the presence of bars/rings, and Col. (5) reports the bar ellipticity (corrected for inclination). Finally, Col. (6) gives the apparent inclination, taken from LEDA.

NED contains morphological information on subtypes for all these isolated galaxies. From our image analysis, we find that 37.5% of the galaxies are earlier than Sbc and 62.5% are of Sbc type or later. The catalog information concerning bars (confirmed and presumed) comprised 19 galaxies before this work, and we were able to add this information to 7 other galaxies. This indicates that up to 65% of the isolated galaxies in this subsample show evidence of barred structure: for 40% the evidence is clear (SB galaxies), and for 25% the bars are weak or suspected (SAB galaxies). The bar fraction is 68% for late-types and 60% for early-types. We have measured the *R*-band and *JHK* isophotal ellipticities associated with a bar and estimated the maximum ellipticity, $\epsilon_{\rm max}$. This quantity (corrected by inclination) is related to a measure of bar strength, such as gravitational bar torque (Laurikainen et al. 2002). Column 5 in Table 5 gives the values of $\epsilon_{\rm max}$ for our sample. Among barred galaxies, the average value of $\epsilon_{\rm max}$ is 0.35 ± 0.13. Two early-type galaxies and four late-type galaxies have $\epsilon_{\rm max} \geq 0.4$, which is commonly considered as evidence of a strong bar. Similarly, the catalog information for rings in our sample previously comprised 16 galaxies; in this work, this information has been added to 7 other galaxies, now accounting for 57.5% of the sample. Notice in Table 5, that galaxies with inclination higher than 80° may not have a reliable classification.

5.1. Morphology, bars, and rings in isolated galaxies

The reclassification presented here (see Table 5) preserves the optically observed morphology but takes into account the NIR bar morphology. In general, the results concerning differences in morphology when passing from the optical to the NIR bands (Eskridge et al. 2000) agree with those in our subsample of isolated galaxies. While the reported fraction of barred galaxies in the optical is almost a factor of 2 smaller than that in the NIR (Eskridge et al. 2000), in our case the fraction is actually small (~20%).

The fraction of galaxies in our sample with clear evidence of optical/IR bars (SB galaxies) is 40%, while 25% more show some evidence of weak bars (SAB galaxies). These fractions are in agreement with estimates from other samples of galaxies (Eskridge et al. 2000; Hernández-Toledo et al. 2007; Verley et al. 2007). We also report the presence of inner (*r*) and outer (*R*) rings when possible, but a detailed ring morphology (Buta 1986, 1995) was not attempted. The fraction of galaxies with rings in our sample is 57.5%. Note that the observed fraction of bars and rings in the present paper can hardly be a bias of our observing procedure, since we simply selected objects according to their availability in the sky.

Bars can be characterized as strong when they are long (relative to the scale-length of the disk), have large $m = 2, 4$ Fourier density amplitudes (typical values for the relative component $m = 2$ between 0.4–0.8, Athanassoula & Misiriotis 2002), and also when they have high ellipticities since the orbital families of bars strongly depend on the underlying gravitational potential. On the other hand, high-resolution *N*-body simulations of isolated disks embedded in CDM halos show that extended strong bars almost always form, but they slow down as a result of angular momentum transport to the disk and halo (Debattista & Sellwood 2000; Athanassoula & Misiriotis 2002;

Table 5. Final morphological classification.

CIG	Type (NED)	Type (This work)	Bars/Rings	Bar ellipticity ϵ_{max}	Inclination
CIG 72	SA(rs)b Sy1.9	SB(r)b	B/R	0.286	54.77
CIG 89	E6?	S0			43.92
CIG 103	SAB(rs)c	SAB(r)cd	B/R	0.464	57.55
CIG 109	SA(rs)b	(R)SA(s)ab	R		68.21
CIG 135	SBa	SB(r)ab	B/R	0.327	51.15
CIG 145	Sab	Sa			80.69
CIG 156	SB(r)ab pec	(R)SBbc	B/R	0.482	42.06
CIG 191	(R')SBa	(R)SBa	B/R	0.255	65.86
CIG 199	Scd	SAB(r)cd	B/R	0.321	72.21
CIG 309	SA(r)ab	SA(r)a	R		40.60
CIG 314	SAB(rs)c	SA(r)d	R		67.33
CIG 392	S0	SB(r)a	B/R	0.265	39.23
CIG 448	SAB(rs)c	SABc	B	–	72.8
CIG 477	SA(s)c HII	Sc			47.55
CIG 491	SAB(r)ab?	SAB(r)c	B/R	–	52.68
CIG 500	(R')SAB(r)ab	SB(r)b	B/R	–	...
CIG 507	Sbc	SABcd	B	–	78.86
CIG 512	SB(s)cd	SBcd	B	0.254	29.2
CIG 525	SB(r)b	SB(r)bc	B/R	0.372	42.57
CIG 539	Sb	SB(r)ab	B/R	0.243	49.37
CIG 547	SAB(s)d	Sd			44.34
CIG 575	SAB(rs)c SBNG	SABc	B	–	44.86
CIG 616	S0/a	SABab	B	–	70.95
CIG 624	SAB(s)d HII	SABdm	B	0.203	53.20
CIG 630	Sb	SA(rs)bc	R		58.25
CIG 631	(R)SA(rs)b	SA(r)bc	R		50.8
CIG 712	(R)SB(r)ab: LINER:	SB(r)b	B/R	0.467	46.77
CIG 716	SA(rs)bc	SA(r)b	R		37.48
CIG 744	Sc	Sd			32.9
CIG 766	SA(s)c HII	SABcd	B	–	70.99
CIG 772	Scd	SA(s)cd			64.66
CIG 800	SBb	SB(s)bc	B	0.513	66.35
CIG 805	Sb	SAB(rs)bc	B/R	0.285	56.86
CIG 812	Sbc	SA(r)c	R		41.09
CIG 838	Sbc	SB(r)bc	B/R	0.289	51.48
CIG 840	SB(s)b	SB(r)bc	B/R	0.348	46.46
CIG 858	SBb	SBb	B	0.601	59.23
CIG 861	SBbc	SBbc	B	0.541	64.43
CIG 862	SBbc	SBbc	B	0.156	24.96
CIG 947	(R)SA(r)ab; Sy LINER	SA(r)ab	R		36.2

Valenzuela & Klypin 2003); eventually, the bars may dissolve, forming a pseudo bulge (e.g., Avila-Reese et al. 2005; Berentzen et al. 2006).

For our sample, we have estimated the bar de-projected maximum ellipticity, ϵ_{max}. We do not find differences in ϵ_{max} as a function of morphological type.

5.2. Distorted morphology and bright/dark galaxies

As discussed in Karachentsev et al. (2006) and according to recent cosmological models, apart from dark halos with normal (luminous) galaxies in their centers, completely dark clumps (sub-halos) should also exist (van den Bosch et al. 2003; Tully 2005; Yang et al. 2005). Apparently, the completely dark galaxies (subhalos) may be detected via gravitational effects (Trentham et al. 2001), thus providing the possibility that the phenomena of interaction will occur even in the case of an isolated galaxy. Hence, a relative number of peculiar shapes among our isolated galaxies may be expected.

We inspected our images to identify visible distortions, asymmetries and structures resembling a tidal origin and/or possible double nuclei or recent merger candidates. Thin open and relatively featureless structures not associated to any underlying disk, and distorted spiral arms, were also interpreted as interaction-induced features. We have classified our sample according to moderate and strong distortions. In Fig. 4 we show 5 cases, among our 40 galaxies, where we have found moderated distortions: CIG 109, CIG 135, CIG 539, CIG 631, and CIG 744 (see Figs. B.3, B.4, B.19, B.25 and B.28 in the electronic version), in the form of slightly distorted arms, low surface brightness and asymmetric bright halos, and a peculiar case of a galaxy with a central clumpy region surrounded by a smooth symmetric envelope.

In contrast, Fig. 5 shows 4 cases of galaxies where the evidence of morphological distortions was stronger: CIG 72, CIG 716, CIG 812, and CIG 838 (see Figs. 3, B.27, B.33, and B.34 in the electronic version), in the form of clear asymmetries and thin filamentary arms resembling tidal features, similar to those features reported in Karachenstsev et al. (2007).

Table 6 reports some structural, photometric and gas content properties for our 40 CIG galaxies that are useful to understand something about the physical nature of these 9 morphologically-distorted isolated galaxies. Column (1) gives the original CIG number, Col. (2) gives the absolute *I* band magnitude (from

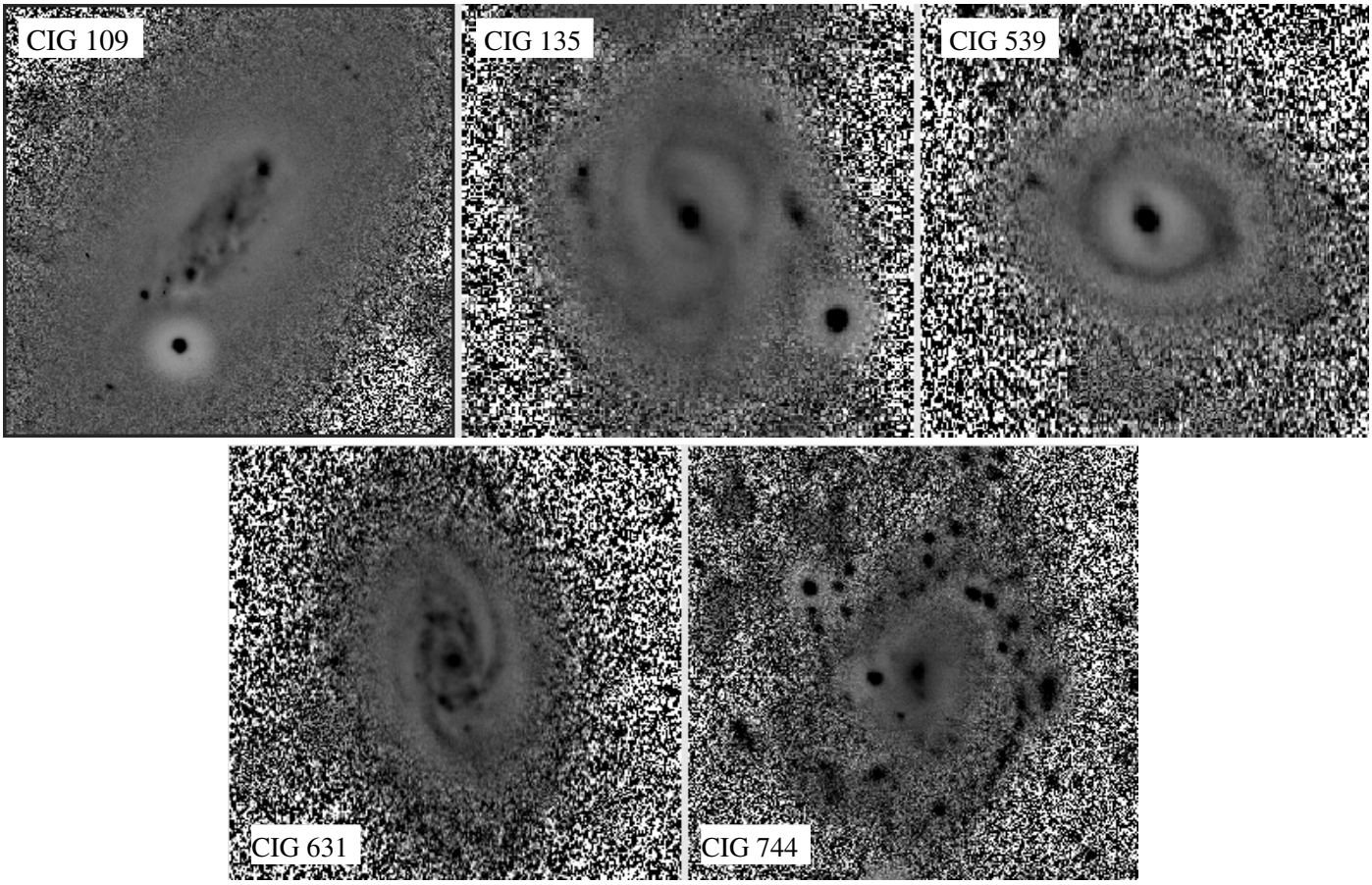

Fig. 4. Galaxies with moderated morphological distortions, CIG 109, CIG 135, CIG 539, CIG 631 and CIG 744. *R*-band filter-enhanced images.

our photometry data), Col. (3) gives the $M_{\rm HI}/L_I$ ratio estimated from our photometry and from data available in the HyperLeda database, Col. (4) gives the central disk surface brightness in the I band (from our surface photometry) and Col. (5) is the category in which the 9 distorted galaxies fall (in accordance to Karachenstsev et al. 2007): (A) galaxies with ripples, plumes, loops or tidal tails caused apparently by a recent merging/close encounter; (B) galaxies of asymmetric shape and star formation, (C) galaxies with peculiar or distorted arms.

In most of the cases, the morphological distortions of the galaxies in Table 6 are moderate and could be evidencing some level of dynamical disturbance.

Although the CIG selection criteria warranties that these galaxies have not suffered perturbations of similar size galaxies over some gigayears, it is now known that the presence of small neighbors could cause a notable effect on the observed morphology. Verley et al. (2007) quantified the isolation degree for all the CIG sample providing 2 parameters (the local number density of neighbor galaxies of comparable or smaller size and the corresponding tidal strength) to estimate the influence of neighbor galaxies on the evolution, and in particular on the observed morphology. Furthermore, by using the complementarity of these parameters, the CIG sample was refined from 950 to 750 galaxies proposed as more dominated by their intrinsic properties.

Our results yield 9 distorted galaxy candidates, 5 of them are also in the list given by Sulentic et al. (2006) of possible interacting candidates in the CIG sample. These 9 distorted candidates were first reviewed for the local number density and tidal strength parameters, finding that 4 of them violate the refinement criteria proposed by Verley et al. (2007) (CIG 72, 539, 631 and 812).

Figure 6 shows a plot of the local number density ($\eta_{\rm k}$) versus the tidal strength (Q) for the refined sample of 791 more likely isolated galaxies from the CIG galaxies. The data has been taken from the published Table 4 in Verley et al. (2007). The solid line and the adjacent dashed lines represent a least square fit to the data along with the corresponding 2 sigma region. Solid triangles represent the position of the morphologically distorted galaxies (CIG 135, CIG 744 and CIG 838) found in our study that do not violate the refinement criteria proposed by Verley et al. (2007) (that is, $Q > -2$ and $\eta_{\rm k} > 2.4$). The solid pentagon symbol represents the position of CIG 716. Notice that since there is no estimate of $\eta_{\rm k}$ for this galaxy, we adopted the mean value for the given Q. Figure 6 shows that all our candidates fall within the 2 sigma dispersion limits despite of being morphologically distorted.

From Table 6, we see that CIG 744 has $M_{\rm HI}/L_I > 1$. From our surface photometry, the disk parameters μ_0 (central surface brightness) and h (scale length) were estimated. We also have explored their trends with other global properties like the gas content or the absolute luminosity. Although it is not the scope of this paper to present a detailed analysis of these correlations, here we will focus on a correlation found between the central disk surface brightness and the content of gas as devised by the $M_{\rm HI}/L_B$ and $M_{\rm HI}/L_I$ ratios.

Figure 7 shows the mass-to-light ratio as a function of disk central surface brightness in the B and I bands. A strong correlation between the gas content of the spirals in our study and their surface brightness is appreciated. To reinforce the correlation,

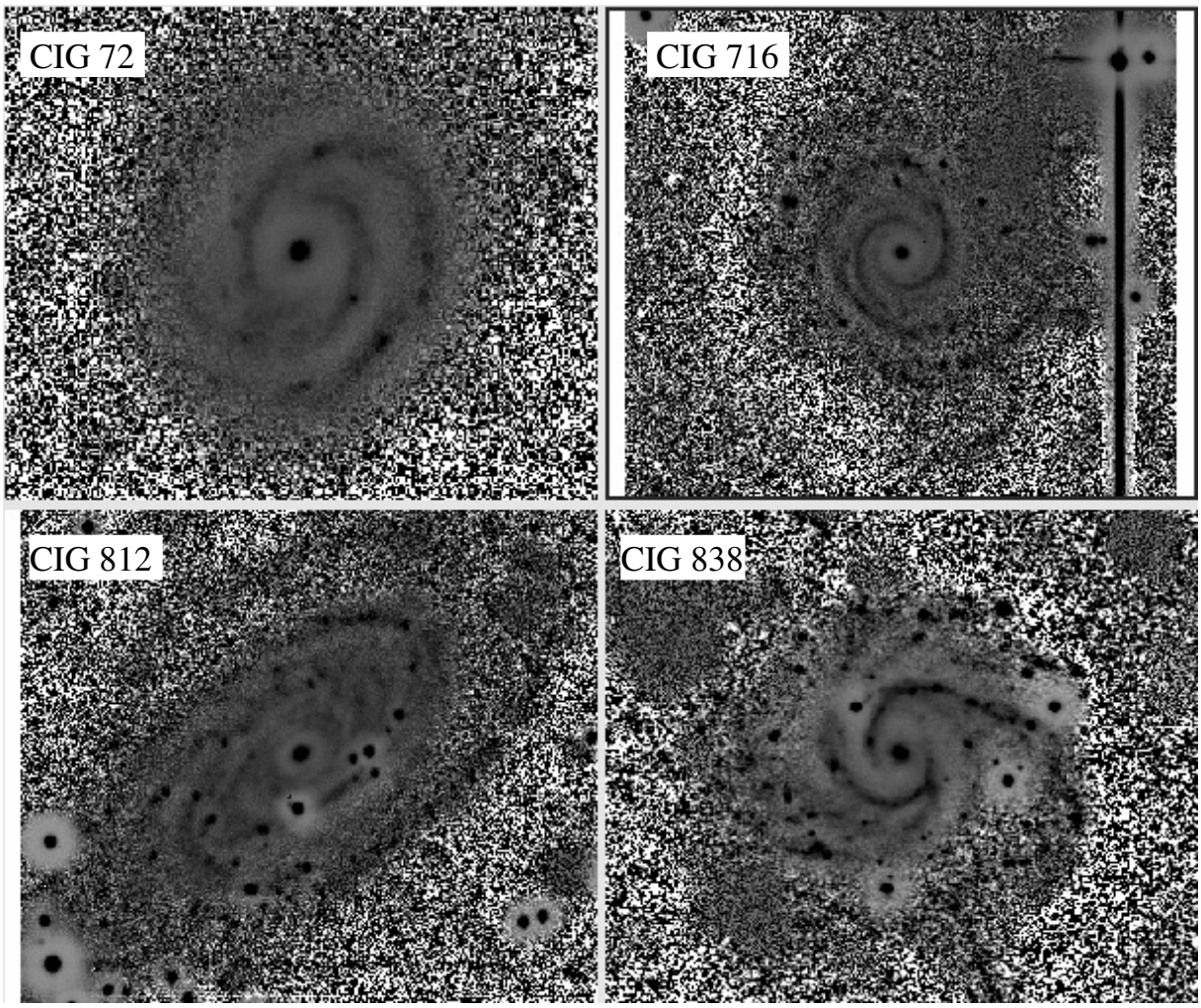

Fig. 5. Galaxies with strong morphological distortions, CIG 72, CIG 716, CIG 812 and CIG 838. *R*-band filter-enhanced images.

we have included the data in McGaugh & de Blok (1997) for a sample of field spiral galaxies. Figure 7 also shows the loci of our 9 morphologically distorted galaxies. Surprisingly CIG 744 is an example of a galaxy in our sample with a very low surface brightness disk and with intrinsically high gas-content.

As discussed in McGaugh & de Blok (1997), there could be some bias behind that correlation but from Tables 5 and 6, it is clear that the galaxies in our study show a wide range in luminosity, span a wide range of morphologies from Sa to Sm/Im and also (Fig. 5) a wide range in surface brightness, allowing us to have a less-biassed interpretation. This correlation reflects real differences in the gas content of all these galaxies and emphasizes the role of the surface brightness of a disk as a fundamental parameter and good indicator of the evolutionary status of a galaxy (Zavala et al. 2003; and Avila-Reese et al. 2008). According to McGaugh & de Blok (1997) lower surface brightness and lower luminosity spirals have consumed less of their gas and are less evolved than brighter systems and perhaps form late. On line to this, CIG 744 is a gas-rich but possibly a less-evolved system than the other galaxies in our sample. Although it is still possible to invoke the existence of dark objects in the neighborhood of CIG 744 as an explanation for its observed distorted morphology, it is first necessary to carefully review the intrinsic physical properties of this galaxy and furthermore, explore other possible causes, to mention; minor mergers in its neighborhood. We notice that from the SDSS images, several dwarf galaxies can still be appreciated, and that, in addition, this object has been flagged as possibly interacting by Sulentic et al. (2006).

6. Physical morphology

Physical morphology has emerged as a useful framework for classifying galaxies on the basis of their underlying physical properties (Morgan & Osterbrock 1969; Abraham et al. 1996; Conselice 1997; Bershady et al. 2000). More recently, Conselice (2003, hereafter C03) has shown that the major ongoing and past formation modes of galaxies can be distinguished by using three model-independent structural (photometric) parameters, which allow to have a robust classification system. These parameters are the concentration of stellar light (C), its asymmetric distribution (A), and a measure of its clumpiness (S).

We present the *CAS* parameters measured at various passband for our observed sample of isolated galaxies. The measurement of the *CAS* parameters for the isolated spiral galaxies was carried out in several steps:

(1) close field stars were removed from each image; (2) sky background was removed from the images; (3) the center of each galaxy was considered as the barycenter of the light distribution and the starting point for measurements; (4) the *CAS* parameters for all the spiral isolated galaxies were estimated directly, i.e. isolated galaxies were not influenced by light contamination

Table 6. Luminosity, gas content, central disk surface brightness and category of morphology distortion.

CIG	$M_{\rm I}$	$M_{\rm HI}/L_I$	$\mu_0^{\rm I}$	Category
CIG 72	–22.261	0.083	19.25	A
CIG 89	–22.529	–	–	–
CIG 103	–21.511	0.125	19.5	–
CIG 109	–19.547	0.167	18.25	B
CIG 135	–22.451	0.175	19.0	A
CIG 145	–22.088	0.024	18.75	–
CIG 156	–21.375	0.028	17.5	–
CIG 191	–23.315	0.044	18.0	–
CIG 199	–21.486	0.283	19.0	–
CIG 309	–22.626	0.006	–	–
CIG 314	–	–	–	–
CIG 392	–22.495	–	19.0	–
CIG 448	–21.033	0.080	17.5	–
CIG 477	–21.134	0.073	17.75	–
CIG 491	–22.201	0.142	18.75	–
CIG 500	–23.584	0.045	19.75	–
CIG 507	–21.379	0.256	20.0	–
CIG 512	–20.390	0.333	21.0	–
CIG 525	–23.158	0.123	19.75	–
CIG 539	–22.633	0.317	18.5	A
CIG 547	–18.978	0.124	20.0	–
CIG 575	–21.589	0.134	18.5	–
CIG 616	–23.461	–	19.5	–
CIG 624	–19.578	0.255	–	–
CIG 630	–21.709	0.163	18.75	–
CIG 631	–21.463	0.143	18.0	B
CIG 712	–21.280	0.155	18.75	–
CIG 716	–23.330	0.291	20.5	A
CIG 744	–19.925	1.052	22.75	C
CIG 766	–20.537	0.146	18.0	–
CIG 772	–22.707	0.002	19.0	–
CIG 800	–23.051	0.068	18.5	–
CIG 805	–22.103	0.275	19.25	–
CIG 812	–22.507	0.304	19.0	A, B
CIG 838	–22.952	0.207	19.5	A
CIG 840	–22.595	0.093	19.25	–
CIG 858	–22.723	0.121	19.0	–
CIG 861	–21.817	–	19.25	–
CIG 862	–22.219	0.081	19.0	–
CIG 947	–	–	–	–

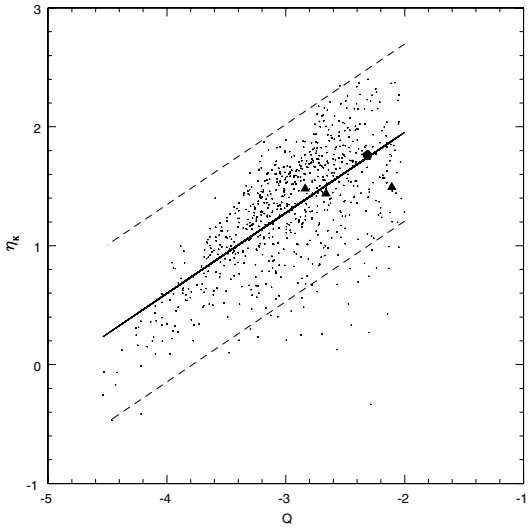

Fig. 6. Local number density $\eta_{\rm k}$ versus tidal strength Q. Solid triangle symbols represent the position of the morphologically distorted galaxies that do not violate the $Q > -2$ rule; the solid pentagon symbol represents CIG 716. Since there is no estimate of $\eta_{\rm k}$ for this galaxy, we adopted the mean value for the given Q.

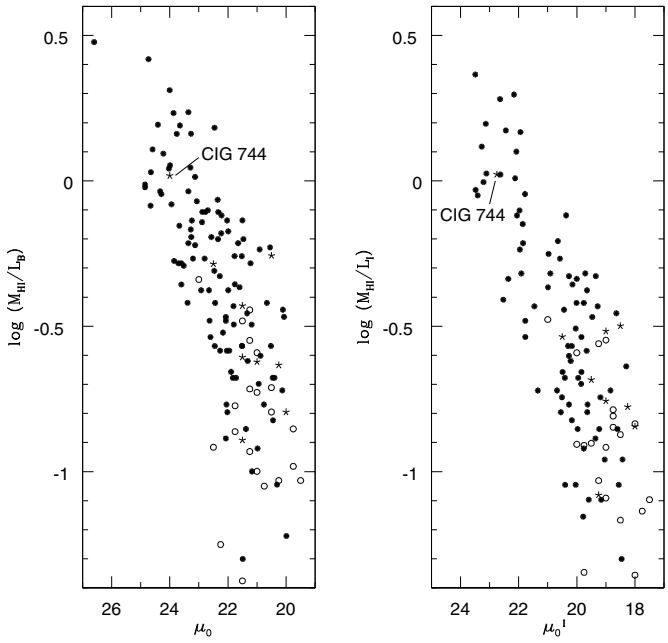

Fig. 7. HI mass-to-light ratio as a function of disk central surface brightness: *B* band (*left*), *I* band (*right*). Solid circles are for data taken from McGaugh & de Blok (1997) for a sample of field spiral galaxies; open circles represent the CIG galaxies from this study and star symbols represent our 9 morphologically distorted galaxies.

from any other galaxy of similar size in the neighborhood (isolation criteria); and (5) galaxies with high inclinations or axis ratios could introduce systematic biased trends in the values of the *CAS* parameters (C03). Isolated galaxies whose apparent axial ratios yield "inclinations" higher than 80° are represented by open circles in the corresponding plots.

6.1. CAS results

In the present analysis we use the *R* band *CAS* parameters and their errors (Table 7). The *CAS* values in the other bands can be provided upon request. Column (1) in Table 7 gives the CIG catalog number, and Cols. (2)–(4) report the *CAS* values with their respective errors, in the *R*-band.

By sorting the sample into early- and late-type spirals (SaSb and SbcSm, respectively), the corresponding average and standard deviation values of the *CAS* parameters are: $\langle C(R)\rangle$(SaSb) = 3.74 ± 0.40, $\langle A(R)\rangle$(SaSb) = 0.09 ± 0.06, $\langle S(R)\rangle$(SaSb) = 0.23 ± 0.21, and $\langle C(R)\rangle$(SbcSm) = 3.19 ± 0.36, $\langle A(R)\rangle$(SbcSm) = 0.16 ± 0.07, $\langle S(R)\rangle$(SbcSm) = 0.38 ± 0.23. Our mean values are consistent with those reported in C03 for the Frei et al. (1996) sample of non-interacting galaxies and also with those reported in Hernández-Toledo et al. (2007). Note that irregulars were included in SbcSm class, while in C03 these galaxies are separated.

Table 7. *R*-Band *CAS* parameters for isolated spiral galaxies.

CIG	$C(R)$	$A(R)$	$S(R)$
CIG 72	3.209 ± 0.097	0.091 ± 0.019	–0.05 ± 0.002
CIG 89	4.28 ± 0.061	0.006 ± 0.008	0.09 ± 0.01
CIG 103	3.052 ± 0.044	0.245 ± 0.016	0.60 ± 0.011
CIG 109	3.491 ± 0.075	0.206 ± 0.007	0.54 ± 0.006
CIG 135	3.443 ± 0.128	0.039 ± 0.008	0.07 ± 0.002
CIG 145	3.409 ± 0.139	0.275 ± 0.011	0.26 ± 0.004
CIG 156	3.403 ± 0.086	0.252 ± 0.003	0.62 ± 0.008
CIG 191	4.131 ± 0.169	0.075 ± 0.009	0.17 ± 0.003
CIG 199	3.292 ± 0.104	0.107 ± 0.019	0.37 ± 0.01
CIG 309	3.892 ± 0.06	0.011 ± 0.008	0.05 ± 0.004
CIG 314	3.306 ± 0.058	0.17 ± 0.014	0.16 ± 0.008
CIG 392	3.824 ± 0.233	0.096 ± 0.007	0.08 ± 0.002
CIG 448	3.357 ± 0.094	0.208 ± 0.006	0.33 ± 0.004
CIG 477	3.672 ± 0.132	0.21 ± 0.004	0.56 ± 0.005
CIG 491	3.05 ± 0.152	0.092 ± 0.013	0.02 ± 0.002
CIG 500	3.519 ± 0.106	0.021 ± 0.03	–0.07 ± 0.01
CIG 507	3.483 ± 0.115	0.108 ± 0.036	0.38 ± 0.02
CIG 512	2.602 ± 0.035	0.026 ± 0.066	–0.06 ± 0.03
CIG 525	3.828 ± 0.109	0.174 ± 0.009	0.46 ± 0.008
CIG 539	4.205 ± 0.196	0.056 ± 0.006	0.06 ± 0.002
CIG 547	2.827 ± 0.049	0.058 ± 0.038	0.37 ± 0.01
CIG 575	3.167 ± 0.089	0.058 ± 0.013	0.06 ± 0.003
CIG 616	4.433 ± 0.19	0.11 ± 0.004	0.08 ± 0.002
CIG 624	3.328 ± 0.041	0.308 ± 0.012	0.71 ± 0.008
CIG 630	3.094 ± 0.104	0.154 ± 0.01	0.46 ± 0.01
CIG 631	2.783 ± 0.114	0.091 ± 0.007	0.25 ± 0.005
CIG 712	3.635 ± 0.046	0.182 ± 0.014	0.44 ± 0.014
CIG 716	3.849 ± 0.05	0.106 ± 0.052	0.07 ± 0.025
CIG 744	3.898 ± 0.083	0.203 ± 0.062	0.18 ± 0.011
CIG 766	2.96 ± 0.076	0.243 ± 0.005	0.60 ± 0.006
CIG 772	3.129 ± 0.089	0.065 ± 0.018	0.14 ± 0.005
CIG 800	2.675 ± 0.091	0.238 ± 0.008	0.59 ± 0.009
CIG 805	3.066 ± 0.098	0.169 ± 0.022	0.17 ± 0.006
CIG 812	3.543 ± 0.063	0.164 ± 0.018	0.60 ± 0.009
CIG 838	3.26 ± 0.067	0.291 ± 0.023	0.68 ± 0.017
CIG 840	2.52 ± 0.065	0.235 ± 0.005	0.59 ± 0.014
CIG 858	3.388 ± 0.125	0.053 ± 0.013	0.43 ± 0.006
CIG 861	3.403 ± 0.311	–0.053 ± 0.277	0.11 ± 0.001
CIG 862	2.97 ± 0.101	0.323 ± 0.01	0.57 ± 0.008
CIG 947	3.748 ± 0.066	0.083 ± 0.011	0.05 ± 0.003

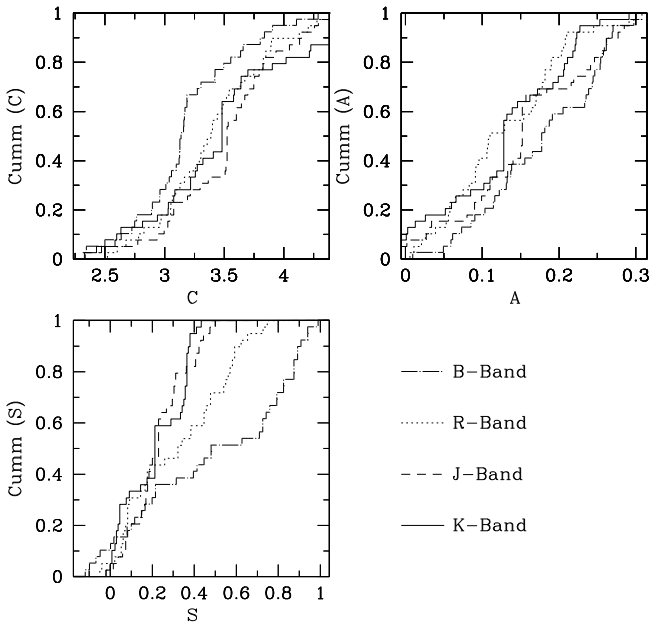

Fig. 8. Cumulative distribution function of *CAS* parameters in the bands *B*, *R*, *J* and *K* bands.

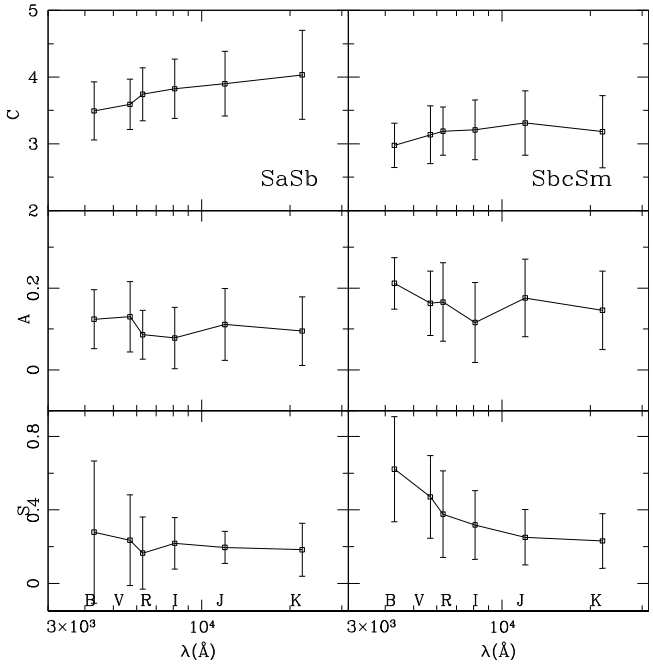

Fig. 9. Average and standard deviation values of the *CAS* parameters as a function of the central wavelength λ(Å). *Left and right columns* are for the subsamples of early (SaSbc) and late (ScSm) isolated galaxies.

Figure 8 shows the cumulative distribution function of the *CAS* parameters at the *B*, *R*, *J* and *K* bands. The concentration *C* becomes higher from bluer to redder bands. In the case of the asymmetry *A* and clumpiness *S* parameters, their values decrease from bluer to redder bands.

In Fig. 9 we plot the average and standard deviation values of the *CAS* parameters versus wavelength for our sample, sorted into early- and late-type spirals (SaSb (*left panel*) and SbcSm (*right panel*), respectively). The *CAS* parameters of later types show, on average, slightly more dependence on wavelength than the early types. Among the *CAS* parameters, clumpiness is the most sensitive to wavelength, although a high scatter is observed in this parameter.

Despite the small number of galaxies in our current sample, we introduce an indicative discussion of the measured *CAS* parameters in different color bands and their trends with other galaxy properties.

Figure 10 shows the loci of the isolated SaSb and SbcSm galaxies in the projected planes of the *R*-band *CAS* space.

The large boxes indicate the amplitude of variation of the *CAS* parameters (lower and upper limits) from the *B* up to the *K* bands. For comparison, the *R*-band averages and standard deviations of galaxies in interacting S+S pairs (Hernández-Toledo et al. 2005), and starburst and ultra luminous infrared galaxies (ULIRGs) (C03) are also plotted.

As appreciated in Fig. 10, the representative values of the *CAS* parameters for our isolated galaxies are significantly lower than the correspondent values observed in interacting/starburst galaxies (Hernández-Toledo et al. 2005).

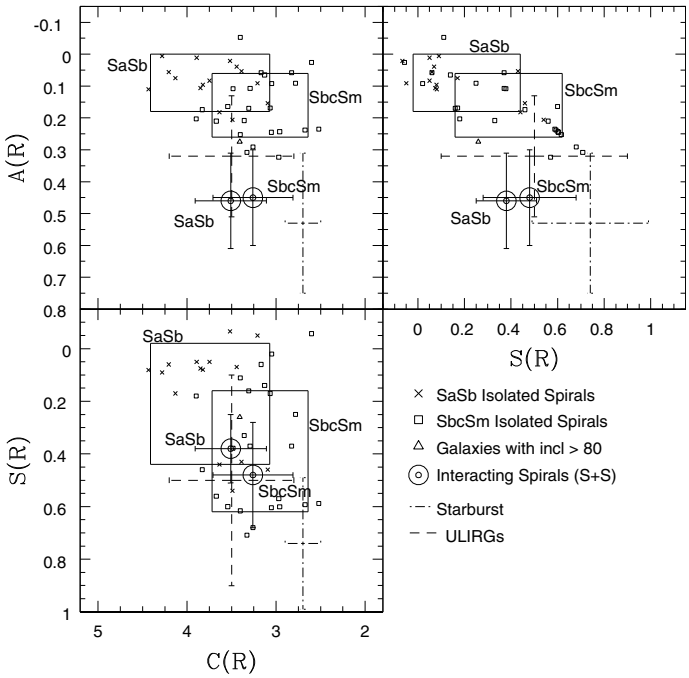

Fig. 10. Loci of the *R*-band *CAS* values and their 1σ dispersion for our isolated SaSb (crosses) and SbcSm (open squares) galaxies in the *CAS* planes. The large boxes illustrate the amplitude of variation of the *CAS* values from all the bands (*B*, *V*, *R*, *I* to *J* and *K*, as estimated in this work). The corresponding *R*-band values for the interacting SaSb and SbcSm galaxies are shown with circles and solid error bars (Hernández-Toledo et al. 2005). Dot-dash-dot and long-dash error bars are for ULIR and starburst galaxies, respectively (C03).

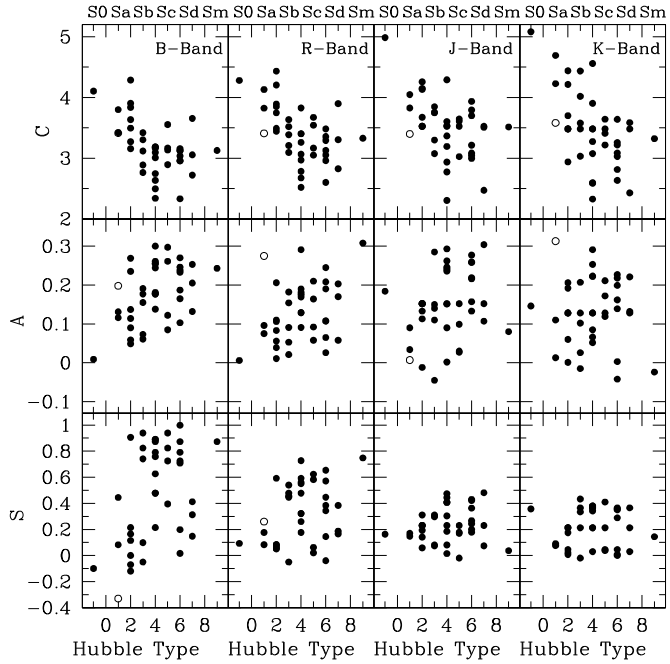

Fig. 11. *CAS* parameters in the *B*, *R*, *J* and *K* bands versus the Hubble type. Galaxies with inclination higher than 80° are shown with (open) circles.

6.1.1. Concentration

The quantitative measure of *C* in our isolated spirals span the range $2.8 \leq C(R) \leq 4.2$. The average and standard deviation values are $\langle C(R) \rangle = 3.4 \pm 0.47$. We have also found that in general *C* systematically increases with the passband (Fig. 9).

According to our current understanding of galaxy formation, disks generally form from the inside out within growing CDM halos (Avila-Reese 2006). Their concentrations (or surface brightnesses) depend mainly on the spin parameter of the halo. CDM halos span a wide log-normal distribution of the spin parameter; hence, one also expects a wide range of concentrations for the disks. Most likely, the observed distribution of concentrations for isolated disk galaxies is not as wide as we would expect from theory. It should also be taken into account that internal secular processes after disk formation rearrange the mass (light) distribution, and that the presence of a big bulge in early-type spirals tends to increase their *C*-parameter with respect to galaxies with smaller bulges. In the case of ellipticals (and probably the bulges of early-type galaxies), theory suggests that they are more concentrated due to the violent and dissipative processes that are at the basis of their formation: major mergers of gaseous disks.

6.1.2. Asymmetry

Some studies have shown that important deviations from axisymmetry exist in the optical and other wavelengths (Rix & Zaritsky 1995; Richter & Sancisi 1994; C03). The asymmetry parameter *A* has been shown to be sensitive mainly to galaxy interactions and mergers but is also influenced by SF clumps, dust lanes, and projection effects (C03; Hernández-Toledo et al. 2005). The quantitative measure of *A* in the present sample of isolated galaxies roughly spans the range $0.03 \leq A(R) \leq 0.23$, the average and standard deviation being $\langle A(R) \rangle = 0.13 \pm 0.08$. The later types are slightly more asymmetric, on average, than the earlier types. The asymmetries reported here are definitively lower than those typical of interacting disk galaxies (see Fig. 10). The *A*-parameter decreases as the passband is redder (Fig. 9). Lower asymmetry values are in part related to SF effects; reflecting the sensitivity of *A* to the passband.

6.1.3. Clumpiness

For our sample of isolated galaxies, $S(R)$ ranges roughly from 0.0 to 0.6, the average and standard deviation values being $\langle S(R) \rangle = 0.31 \pm 0.23$. The *S*-parameter is, on average, higher and more scattered in later types than in earlier types, as seen in Fig. 9 (see also below). Late-type galaxies present more current SF activity than early-type galaxies. Although the parameter *S* in our isolated galaxies is typically lower than in interacting spirals, the differences are actually small and not as significant as in the case of the asymmetry parameter (Fig. 10).

6.1.4. Correlations

Figures 11 and 12 show the *B*-, *R*-, *J*- and *K*- band *CAS* parameters versus morphological type *T* and corrected total $(B-I)$ color. Nearly edge-on galaxies (inclination $\geq 80°$) are plotted with open circles.

From Figs. 11 and 12 the trend of the *C* and *A* parameters with *T* and total $(B-I)$ color typically tends to be more robust in the redder bands, emphasizing the merits of IR wavelengths, which are less contaminated from (transient) SF effects and better represent the basic structure of galaxies. The images from the 2MASS have a noisy background, especially in the *K*-band.

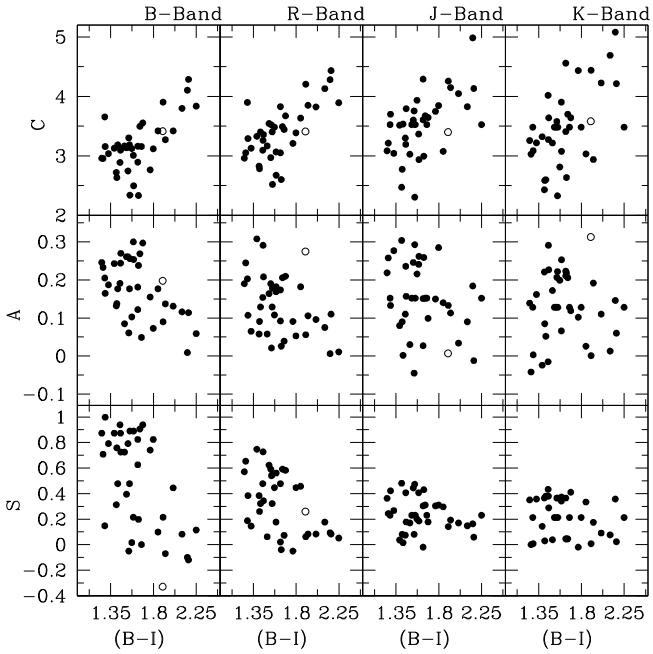

Fig. 12. *CAS* parameters in the *B*, *R*, *J* and *K* bands versus the corrected total $(B-I)$ color. Galaxies with inclination higher than 80° are shown with (open) circles.

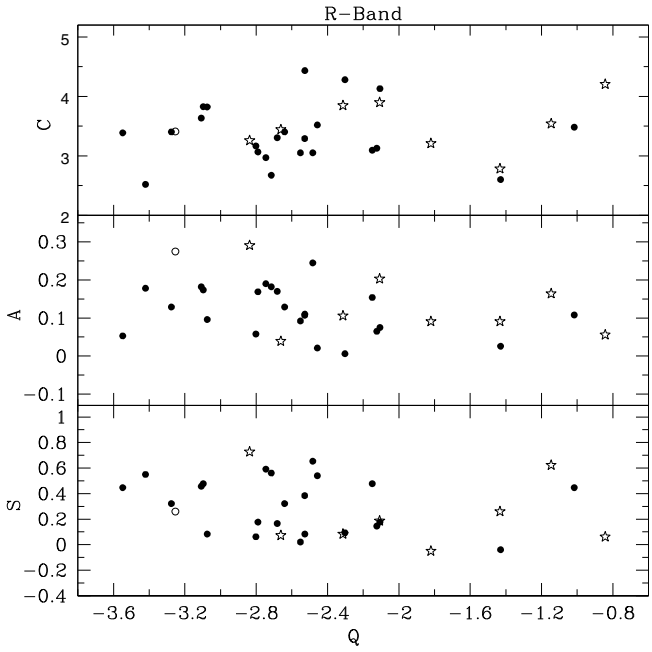

Fig. 13. *CAS* parameters in the *R* band versus tidal strength *Q* (as reported by Verheijen 1997). Galaxies with inclination higher than 80° are shown with open circles, disturbed candidates are shown with open stars.

Therefore, the *K*-band data discussed here should be taken only as indicative.

The morphological type is led mainly by the bulge-to-disk ratio. The global color is also affected by this ratio. Therefore, it is expected that earlier types will be more concentrated and redder. However, the *C*-parameter and the global color are not too sensitive to the bulge-to-disk ratio for galaxies with intermediate-to-low values of this ratio (say, Sb types and later); therefore, in these cases, the measured *C* and global color reflect mostly the pure disk concentration and color. Thus, that *C* depends on *T* for late types mainly implies a connection between the spiral arm properties and the disk concentration. The dependence of *C* on color would mainly imply that less concentrated disks have a more constant SF history, probably because their gas surface densities are low.

Concerning asymmetry, the observed dependence on *T* indicates that most of the asymmetry of our isolated spirals is associated with the natural flocculency in later type galaxies, as well as with SF, which is more active for later types (as it is also evidenced by the trend of higher *S*-values as the types are later and the colors bluer). In this interpretation, the effect of large-scale perturbations (cf. interactions) is neglected.

Finally Fig. 13 shows a plot of the *CAS* parameters vs. the tidal strength *Q* parameter (as given in Verley et al. 2007). Galaxies with inclination higher than 80° are shown with open circles. The disturbed candidates found in this study are shown as open-star symbols. Since values of *Q* higher than –2 are indicative of galaxies being in interacting states (Athanassoula 1984), it is reasonable to expect some visible signs of morphological distortions in their optical images. Figure 13 shows no trend of *Q* with any of the *CAS* parameters.

Among our 9 morphologically distorted candidates with available *Q*, even those with a $Q > -2$ do not show a significantly higher *A* or *S* values, confirming that the *CAS* parameters are not sensitive enough for detecting low intensity distortions.

7. Summary and conclusions

We present results of our *BVRI* CCD photometry for a set of 40 isolated galaxies selected from the CIG (Karachentseva 1973). We have shown that our derived parameters are generally in good agreement with the aperture photometry reported in the HyperLeda database and other individual photometric works. In addition, we present multi-aperture photometry (Appendix A) in order to facilitate further comparisons and contribute to the existing databases of aperture photometry (e.g., HyperLeda).

We have reevaluated the morphology of each of the galaxies based on our mosaic *R*-band and filter-enhanced *R*-band images, two-dimensional $(B-I)$ color maps, composed NIR *JHK* images from the 2MASS archives, photometric ϵ and PA radial profiles, and *RGB* images from SDSS. Emphasis on structural features such as bars, rings and global disturbances was given.

We have demonstrated the convenience of analyzing the morphology through the combination of optical, near-infrared and SDSS *RGB* images.

The sample morphological types range from Sa to Sm, 37.5% of the galaxies being SaSb, and 62.5% being of Sbc or later types. After our reclassification, we found that ~40% of the galaxies are clearly barred (SB), while ~25% more show some evidence of a suspected bar (SAB). The bar fraction is 68% for late-types and 60% for early-types. The average and standard deviation values of the *R*-band de-projected maximum ellipticity of the bars, $\epsilon_{\rm max}$, is 0.35 ± 0.1 for both early and late types, indicating that there is no trend of $\epsilon_{\rm max}$ with the morphological type. We have also found that 57.5% of the isolated galaxies in our sample show ring structures.

From our image analysis we found 9 candidates of isolated galaxies (CIG 539, 631, 744, 109, 135, 72, 716, 812, 838) with disturbed morphology. After reviewing those galaxies for the presence of equal and smaller size galaxies in their neighborhood (cf. Verley et al. 2007), we found CIG 744 having

$M_{\rm HI}/L_B > 1$ as a possible candidate to interact with a gas-rich dark object. However, after studying the HI mass-to-light ratio as a function of disk central surface brightness for our 40 CIG galaxies, CIG 744 is interpreted rather as an intrinsically gas-rich but possibly less evolved system, instead.

We have also calculated the *BVRI*-, *J*, *H* and *K*-band *CAS* parameters for the sample. The *CAS* averages and standard deviations in the *R*-band for the SaSb and SbcSm subsamples are: $\langle C(R)\rangle$(SaSb) = 3.74 ± 0.40, $\langle A(R)\rangle$(SaSb) = 0.09 ± 0.06, $\langle S(R)\rangle$(SaSb) = 0.23 ± 0.21 and $\langle C(R)\rangle$(SbcSm) = 3.19 ± 0.36, $\langle A(R)\rangle$(SbcSm) = 0.16 ± 0.07, $\langle S(R)\rangle$(SbcSm) = 0.38 ± 0.23, respectively. These values are in good agreement with previous results for a similarly selected subsample of isolated galaxies and other studies of non-interacting galaxies. The results of the *S* parameter should be taken only as indicative due to the noisy nature of the *J*, *H* and *K* images.

While *C* systematically increases from bluer to redder bands, both *A* and *S* decrease. The *C* and *A* parameters present more robust trends with the morphological type *T* and the total $(B-I)$ color in the redder bands, suggesting that the basic structure of galaxies is revealed better towards the infrared bands. The *C*-parameter tends to be higher for earlier type and redder galaxies, while *A* and *S* tend to be lower.

Through the loci of our isolated galaxies in the projected planes of the *CAS* space, we have tested the ability of these diagrams to differentiate between isolated and interacting/starburst spirals. The observed values of the *CAS* parameters for these isolated galaxies are always lower than the expected values for interacting galaxies. The distortions seen in our nine morphologically distorted candidates are not strong enough to be detected by the *CAS* parameters.

This paper is a step in the building of a well-defined sample of local isolated galaxies with uniform and detailed photometric information. This is relevant because it provides a fair database for comparison with model predictions, as well as with observed samples of galaxies in other environments and at higher redshifts.

Through our image procedures we were able to detect a set of morphologically distorted galaxy candidates. However, a more careful and detailed analysis involving our surface photometry and other physical properties is required. A study like this will provide better constraints on the end product of galaxy-galaxy merging and how this is changing the morphological properties of the isolated galaxy population.

Acknowledgements. H.M.H.T. thanks the staff of the Observatorio Astronómico Nacional in San Pedro Mártir, Baja California, for the help with the observation runs. This work was funded by CONACyT grant 42810 to H.M.H.T. This research has made use of the NASA/IPAC Extragalactic Database (NED) which is operated by the Jet Propulsion Laboratory, California Institute of Technology, under contract with the National Aeronautics and Space Administration. We acknowledge use of the HyperLeda database (http://leda.univ-lyon1.fr). This publication makes use of data products from the Two Micron All Sky Survey, which is a joint project of the University of Massachusetts and the Infrared Processing and Analysis Center, California Institute of Technology, funded by the National Aeronautics and Space Administration and the National Science Foundation. Funding for the Sloan Digital Sky Survey (SDSS) has been provided by the Alfred P. Sloan Foundation, the Participating Institutions, the National Aeronautics and Space Administration, the National Science Foundation, the US Department of Energy, the Japanese Monbukagakusho, and the Max Planck Society. The SDSS Web site is http://www.sdss.org/. The SDSS is managed by the Astrophysical Research Consortium (ARC) for the Participating Institutions. The Participating Institutions are The University of Chicago, Fermilab, the Institute for Advanced Study, the Japan Participation Group, The Johns Hopkins University, Los Alamos National Laboratory, the Max-Planck-Institute for Astronomy (MPIA), the Max-Planck-Institute for Astrophysics (MPA), New Mexico State University, University of Pittsburgh, Princeton University, the United States Naval Observatory, and the University of Washington. S.O.E. thanks CONACyT through grant 42810 for the financial support during the preparation of this paper.

References

Abraham, R. G., Tanvir, N. R., Santiago, B. X., et al. 1996, MNRAS, 279, L47
Athanassoula, E. 1984, Phys. Rep., 114, 321
Athanassoula, E., & Misiriotis, A. 2002, MNRAS, 330, 35
Avila-Reese, V. 2006, preprint [arXiv:astro-ph/0605212]
Avila-Reese, V., & Firmani, C. 2000, RMxAA, 36, 23A
Avila-Reese, V., Carrillo, A., Valenzuela, O., & Klypin, A. 2005, MNRAS, 361, 997
Avila-Reese, V., Zavala, J., Firmani, C., & Hernández-Toledo, H. 2008, AJ, submitted
Berentzen, I., Shlosman, I., & Jogee, S. 2006, ApJ, 637, 582
Bershady, M. A., Jangren, A., & Conselice, C. J. 2000, AJ, 119, 2645
Buta, R. 1986, ApJS, 61, 609
Buta, R. 1995, ApJS, 96, 39
Chevalier, C., & Ilovaisky, S. A. 1991, A&A, 90, 225
Conselice, C. J. 1997, PASP, 109, 1251
Conselice, C. J. 2003, ApJS, 147, 1 (C03)
Debattista, V. P., & Sellwood, J. A. 2000, ApJ, 543, 704
de Jong, R. S. 1996, A&A, 313, 377
Dressler, A. 1980, ApJ, 236, 351
Eskridge, P. B., Frogel, J. A., Pogge, R. W., et al. 2000, AJ, 119, 536
Firmani, C., & Avila-Reese, V. 2000, MNRAS, 315, 457
Frei, Z., Guhathakurta, P., Gunn, J. E., & Tyson, J. A. 1996, AJ, 111, 174
Giovanelli, R., Haynes, M. P., Salzer, J. J., et al. 1995, AJ, 110, 1059
Hernández-Toledo, H. M., Dultzin-Hacyan, D., González, J. J., & Sulentic, J. 1999, AJ, 118, 108
Hernández-Toledo, H. M., Avila-Reese, V., Conselice, C. J., & Puerari, I. 2005, AJ, 129, 682
Hernández-Toledo, H. M., Zendejas-Dominguez, J., & Avila-Reese, V. 2007, AJ, 135, 2286
Karachentsev, I. D., Karachentseva, V. E., & Huchtmeier, W. K. 2006, A&A, 451, 817
Karachentsev, I. D., Karachentseva, V. E., & Huchtmeier, W. K. 2007, ed. D. I. Makarov, & S. S. Kaisin [arXiv:astro-ph/0708.1046v1]
Karachentseva, V. E. 1973, Astrof. Issledovanija Byu. Spec. Ast. Obs., 8, 3
Klypin, A. A., Kravtsov, A. V., Valenzuela, O., & Prada, F. 1999, ApJ, 522, 82
Landolt, A. U. 1992, AJ, 104, 340L
Laurikainen, E., Salo, H., & Rautiainen, P. 2002, MNRAS, 331, 880
McGaugh, S. S., & de Blok, W. J. G. 1997, ApJ, 481, 689
Moore, B., Ghigna, S., Governato, F., et al. 1999, ApJ, 524, L19
Morgan, W. W., & Osterbrock, D. E. 1969, AJ, 74, 515
Park, C., Gott, J. R., & Choi, Y. [arXiv:0708.4118]
Pisano, D. J., Wilcots, E. M., & Liu, C. T. 2002, ApJS, 142, 161
Postman, M., & Geller, M. J. 1984, ApJ, 281, 95
Prugniel, P. 1987, CDS Bull., 33, 17
Richter, O., & Sancisi, R. 1994, A&A, 290, L9
Rix, H., & Zaritsky, D. 1995, ApJ, 447, 82
Roberts, M. S., & Haynes, M. P. 1994, ARA&A, 32, 115
Schlegel, D. J., Finkbeiner, D. P., & Davis, M. 1998 ApJ, 500, 525
Shustov, B., Wiebe, D., & Tutukov, A. 1997, A&A, 317, 397
Skrutskie, M. F., Cutri, R. M., Stiening, R., et al. 2006, AJ, 131, 1163
Sofue, Y. 1993, PASP, 105, 308
Sulentic, J. W., Verdes-Montenegro, L., Bergond, G., et al. 2006, A&A, 449, 937
Trentham, N., Möller, O., & Ramirez-Ruiz, E. 2001, MNRAS, 322, 658
Tully, R. B. 2005, ApJ, 618, 214
Tully, R. B., & Pierce, M. J. 2000, ApJ, 533, 744
Tully, R. B., Pierce, M. J., Huang, J., et al. 1998, AJ, 115, 2264
Valenzuela, O., & Klypin, A. 2003, MNRAS, 345, 406
van den Bosch, F., Yang, X., & Mo, H. J. MNRAS, 340, 771
Verheijen, M. A. W. 1997, Ph.D. Thesis,
Verley, S., Leon, S., Verdes-Montenegro, L., et al. 2007, A&A, 472, 121
Wang, B., & Heckman, T. M. 1996, ApJ, 457, 645
Whitford, A. E. 1936, ApJ, 83, 424
Wozniak, H., Friedli, D., Martinet, L., Martin, P., & Bratschi, P. 1995, A&AS, 111, 115
Yang, X., Mo, H. J., & van den Bosch, F. C. 2005, MNRAS, 358, 217
Zavala, J., Avila-Reese, V., Hernández-Toledo, H., & Firmani, C. 2003, A&A, 412, 633

Appendix A: Aperture photometry

Since the birth of galaxy photometry (Whitford 1936), the amount of photometric data has increased exponentially (Prugniel 1987). However, these data are inhomogeneous in both quality and format: photographic, photoelectric, or more recently, CCD observations. The data are usually presented as centered aperture photometry through circular or elliptical apertures or as photometric profiles. In order to take into account the continuously growing amount of photometric data and at the same time make different photometric data reports somehow comparable, we present in Table A.1 our estimations of integrated magnitudes in two additional concentric circular apertures. Column (1) is the original CIG number, Cols. (2) and (7) give the logarithm of the aperture radius (in units of $0.1'$, see the HyperLeda convention) for each isolated spiral galaxy. Columns (3)–(6) and (8)–(11) give their corresponding magnitudes in the *B*, *V*, *R*, and *I* bands. Typical uncertainties in the magnitudes are 0.11, 0.12, 0.11, and 0.12 in *B*, *V*, *R*, and *I* bands, respectively.

Table A.1. Magnitudes at two different circular apertures. $A2 > A1$.

CIG	Log $A2$	B	V	R	I	Log $A1$	B	V	R	I
CIG 72	1.00518	14.513	13.692	13.163	12.462	0.70415	15.235	14.339	13.781	13.071
CIG 89	1.209	12.475	11.530	10.962	10.026	0.908	12.956	11.951	11.386	10.520
CIG 103	1.32045	13.497	12.564	11.932	11.161	1.01942	14.245	13.257	12.613	11.800
CIG 109	1.20016	12.734	12.037	11.563	10.869	0.89913	13.091	12.446	11.958	11.302
CIG 135	1.04657	14.701	13.797	13.223	12.443	0.74554	15.168	14.219	13.615	12.840
CIG 145	1.10784	15.046	13.919	13.264	12.404	0.80681	15.329	14.194	13.531	12.671
CIG 156	0.92600	13.677	13.064	12.631	11.986	0.62497	14.150	13.564	13.172	12.609
CIG 191	1.04657	14.564	13.546	13.117	12.060	0.74554	14.904	13.873	13.298	12.419
CIG 199	1.15131	14.519	13.921	13.451	12.796	0.85028	14.908	14.247	13.754	13.102
CIG 309	1.227	11.644	10.698	10.143	9.249	0.926	12.240	11.259	10.711	9.855
CIG 314	1.415	12.331	11.749	11.344	...	1.114	12.788	12.143	11.716	...
CIG 392	0.92600	14.997	14.132	13.592	12.892	0.62497	15.290	14.428	13.876	13.197
CIG 448	1.30621	12.631	12.011	11.518	10.849	1.00518	12.904	12.260	11.749	11.078
CIG 477	1.13012	12.619	11.953	11.412	10.775	0.82909	12.986	12.297	11.745	11.111
CIG 491	0.88979	14.706	14.002	13.489	12.852	0.58876	15.243	14.484	13.936	13.296
CIG 500	1.09626	14.158	13.247	12.689	12.018	0.79523	14.940	13.954	13.371	12.676
CIG 507	1.13012	15.334	14.762	14.287	13.609	0.82909	15.674	15.086	14.639	14.083
CIG 512	1.25234	14.001	13.251	12.748	12.141	0.95131	15.104	14.203	13.662	13.041
CIG 525	1.07213	14.033	13.332	12.817	12.188	0.77110	14.689	13.892	13.343	12.689
CIG 539	1.07213	14.211	13.353	12.808	12.122	0.77110	14.568	13.660	13.092	12.406
CIG 547	1.22703	13.661	13.056	12.640	12.127	0.92600	14.394	13.749	13.312	12.773
CIG 575	1.18127	13.262	12.623	12.149	11.569	0.88024	13.692	13.021	12.522	11.918
CIG 616	1.26842	14.400	13.268	12.675	11.918	0.96739	14.579	13.657	13.034	12.251
CIG 624	1.306	11.970	11.538	11.138	10.491	1.005	12.714	12.208	11.785	11.182
CIG 630	1.10784	14.157	13.476	12.981	12.406	0.80681	14.655	13.925	13.400	12.778
CIG 631	1.18127	13.207	12.962	12.475	11.599	0.88024	13.411	13.157	12.662	11.799
CIG 712	1.18127	13.313	12.512	11.964	11.294	0.88024	13.958	13.118	12.553	11.878
CIG 716	1.00518	15.023	14.125	13.561	12.879	0.70415	15.829	14.807	14.179	13.489
CIG 744	1.25234	14.672	14.137	13.798	13.298	0.95131	15.204	14.600	14.226	13.725
CIG 766	1.18127	12.327	11.770	11.339	10.795	0.88024	12.880	12.292	11.841	11.295
CIG 772	1.22703	13.925	13.217	12.715	12.121	0.92600	14.384	13.618	13.086	12.432
CIG 800	1.04657	14.322	13.515	12.950	12.285	0.74554	15.074	14.229	13.639	12.930
CIG 805	1.07213	14.389	13.628	13.098	12.484	0.77110	14.887	14.090	13.540	12.896
CIG 812	1.26842	13.229	12.450	11.880	11.177	0.96739	13.802	12.931	12.326	11.569
CIG 838	1.16153	14.120	13.347	12.825	12.246	0.86050	14.623	13.830	13.284	12.656
CIG 840	1.13012	13.726	13.001	12.488	11.907	0.82909	14.659	13.890	13.340	12.680
CIG 858	1.07213	14.412	13.533	12.954	12.256	0.77110	14.937	13.991	13.383	12.668
CIG 861	1.00518	15.454	14.712	14.204	13.624	0.70415	15.831	15.079	14.553	13.948
CIG 862	1.04657	14.047	13.331	12.792	12.321	0.74554	14.642	13.874	13.306	12.708
CIG 947	1.313	11.560	10.660	...	...	1.012	12.140	11.145	...	...

Appendix B

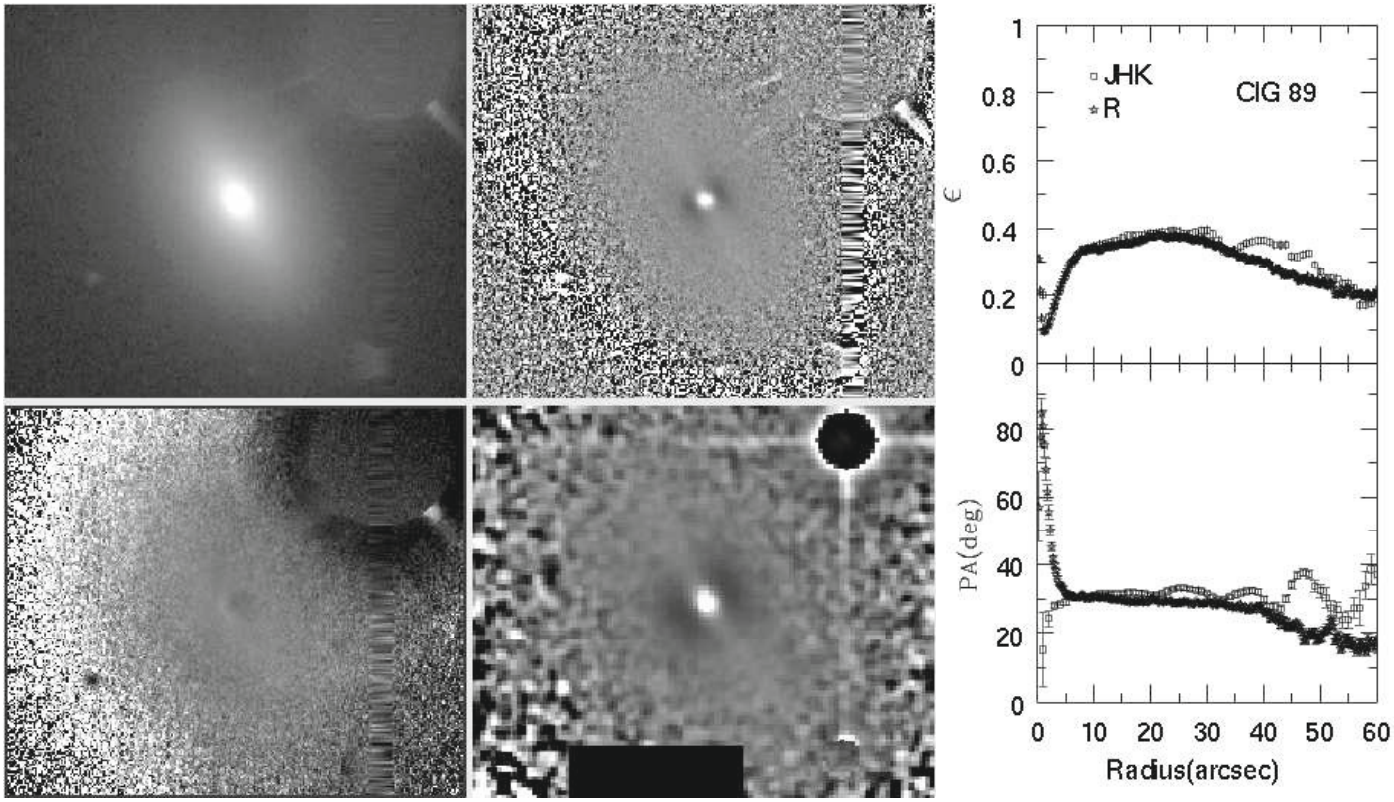

Fig. B.1. CIG 89 Mosaic. Same as Fig. 3. The major diameter of the galaxy in the optical images is 2.6 arcmin.

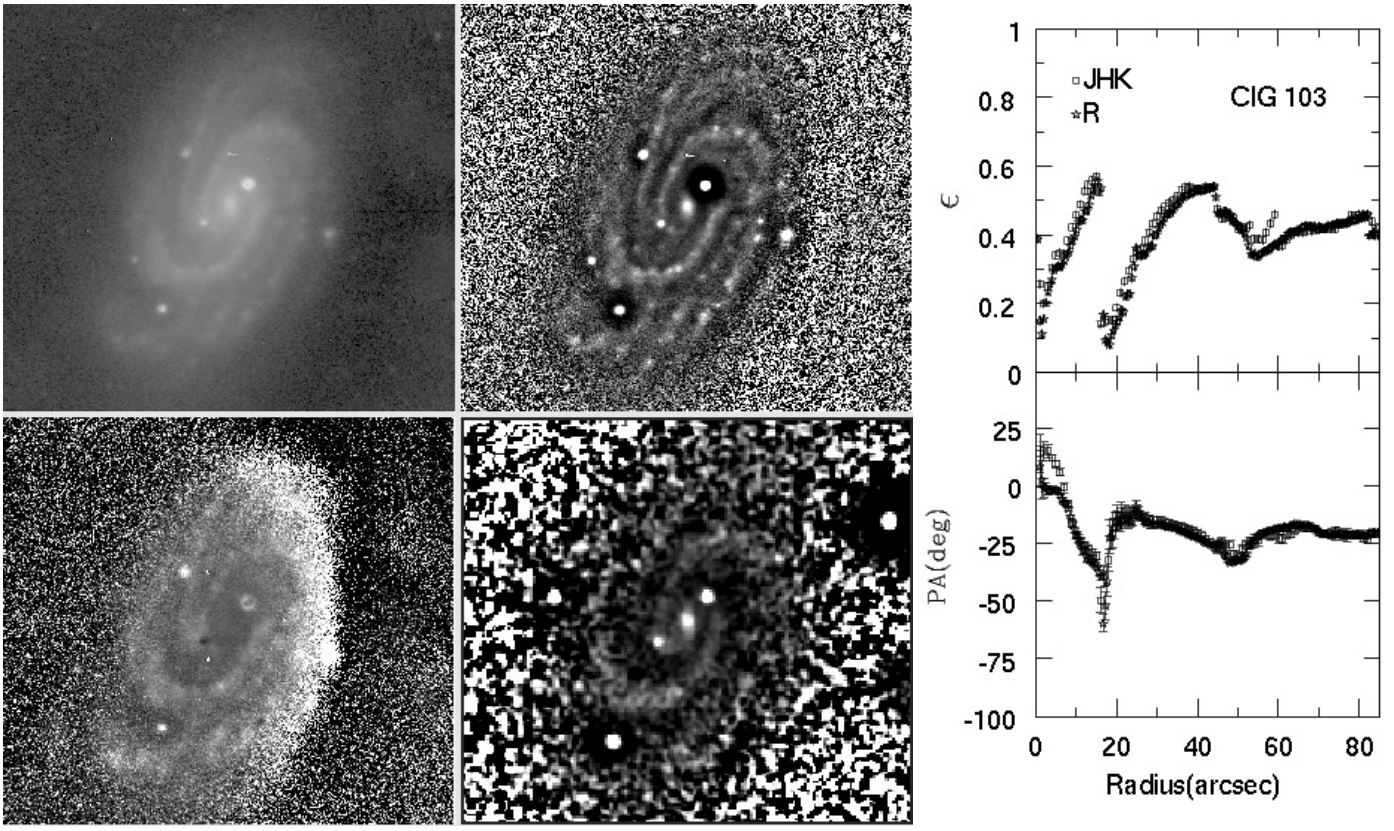

Fig. B.2. CIG 103 Mosaic. Same as Fig. 3. The major diameter of the galaxy in the optical images is 3.5 arcmin.

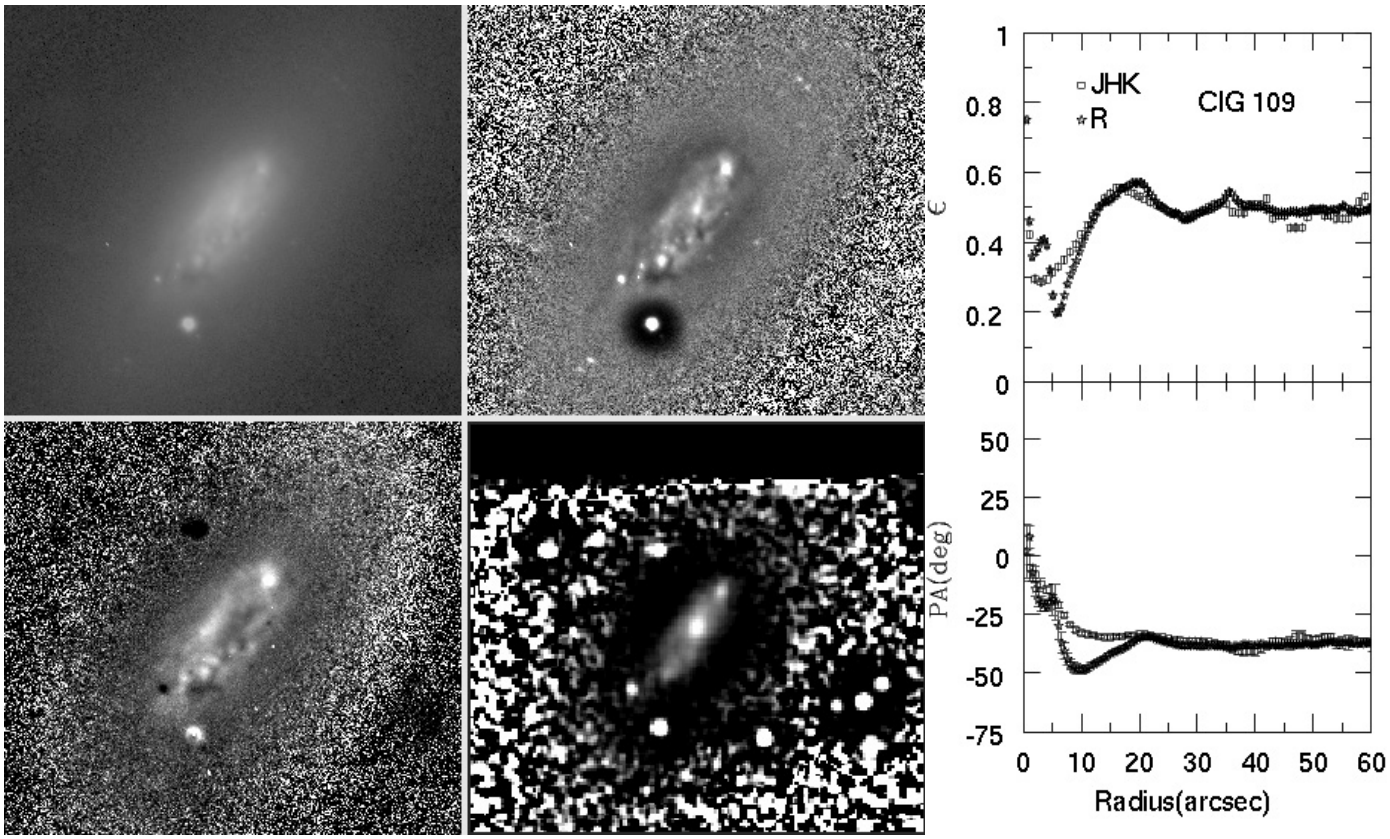

Fig. B.3. CIG 109 Mosaic. Same as Fig. 3. The major diameter of the galaxy in the optical images is 2.4 arcmin.

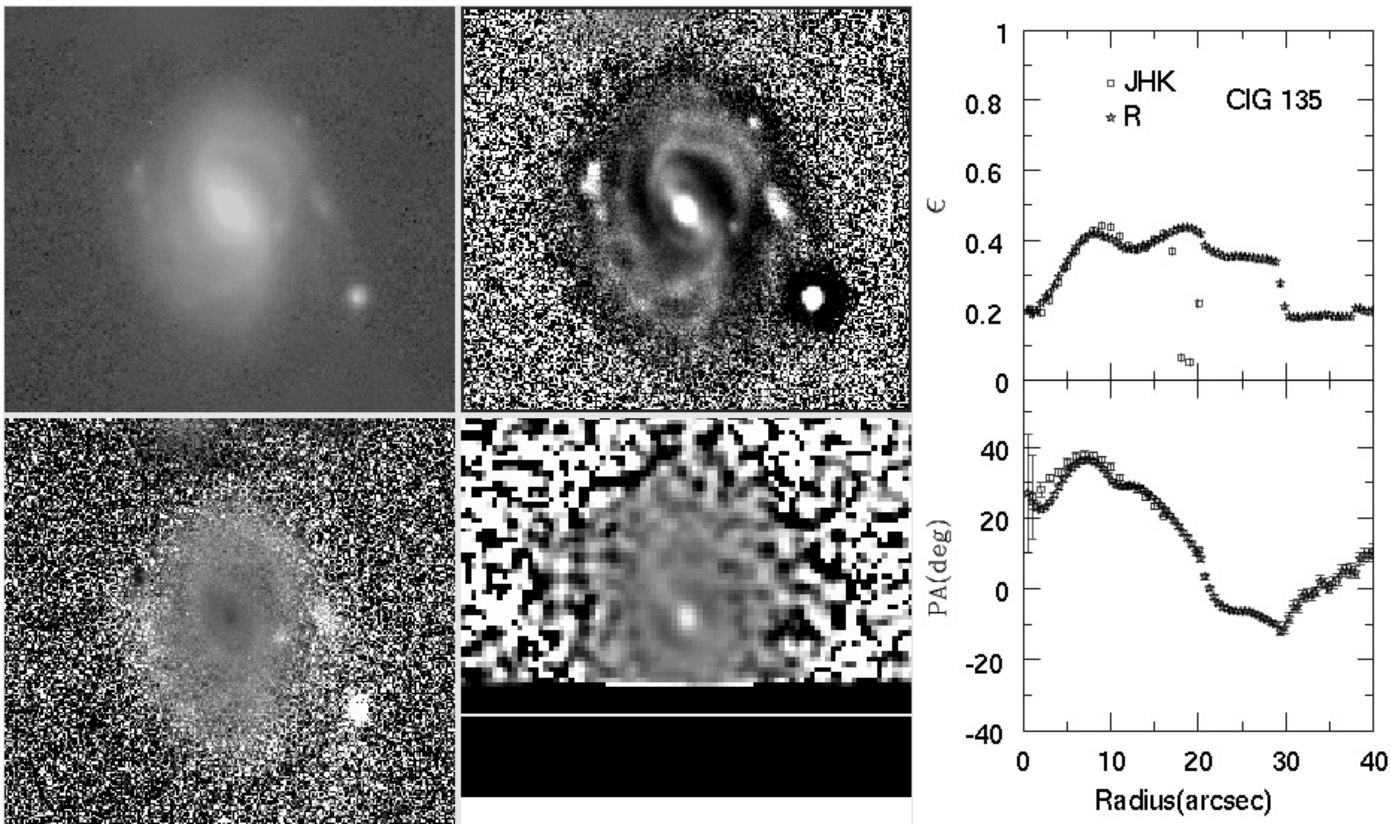

Fig. B.4. CIG 135 Mosaic. Same as Fig. 3. The major diameter of the galaxy in the optical images is 1.1 arcmin.

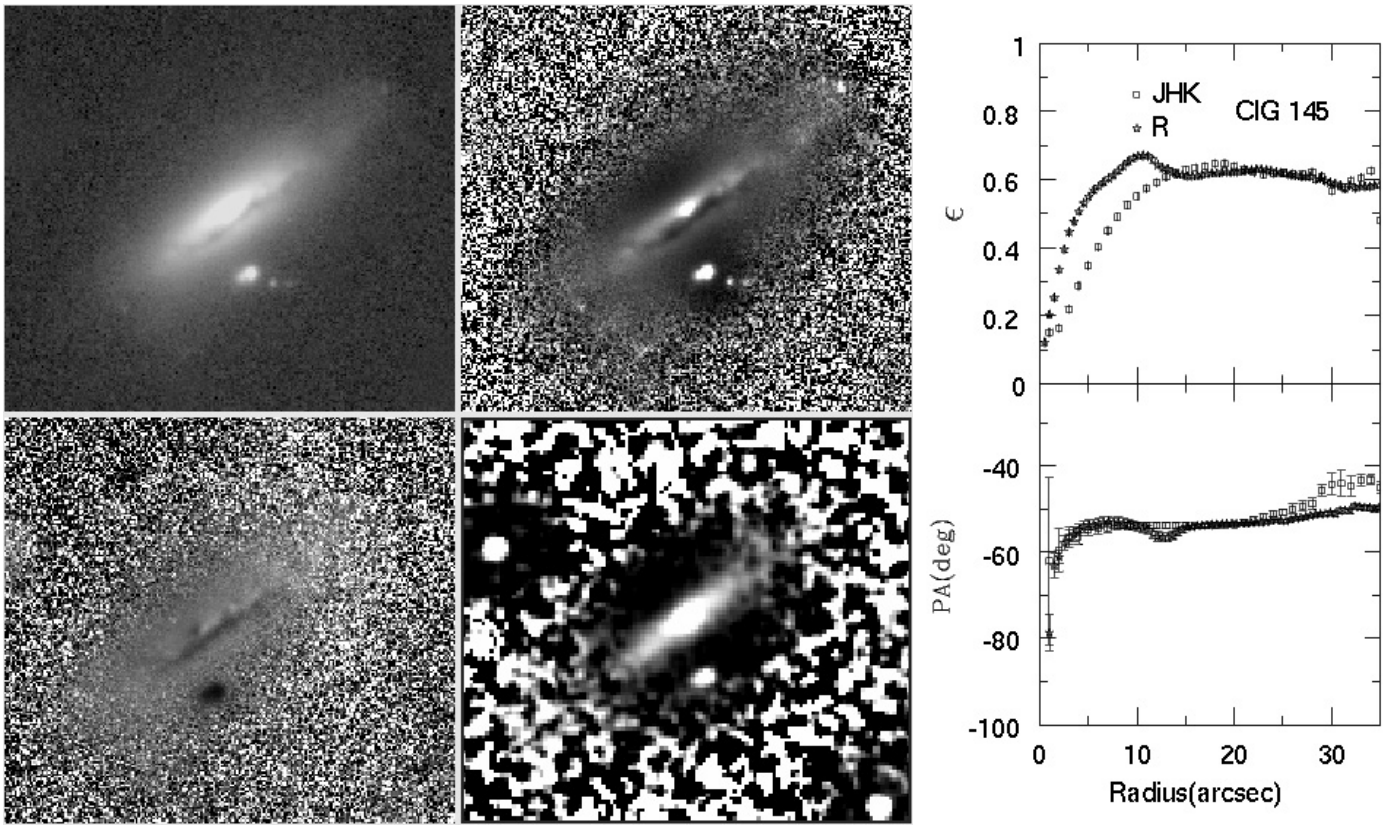

Fig. B.5. CIG 145 Mosaic. Same as Fig. 3. The major diameter of the galaxy in the optical images is 1.3 arcmin.

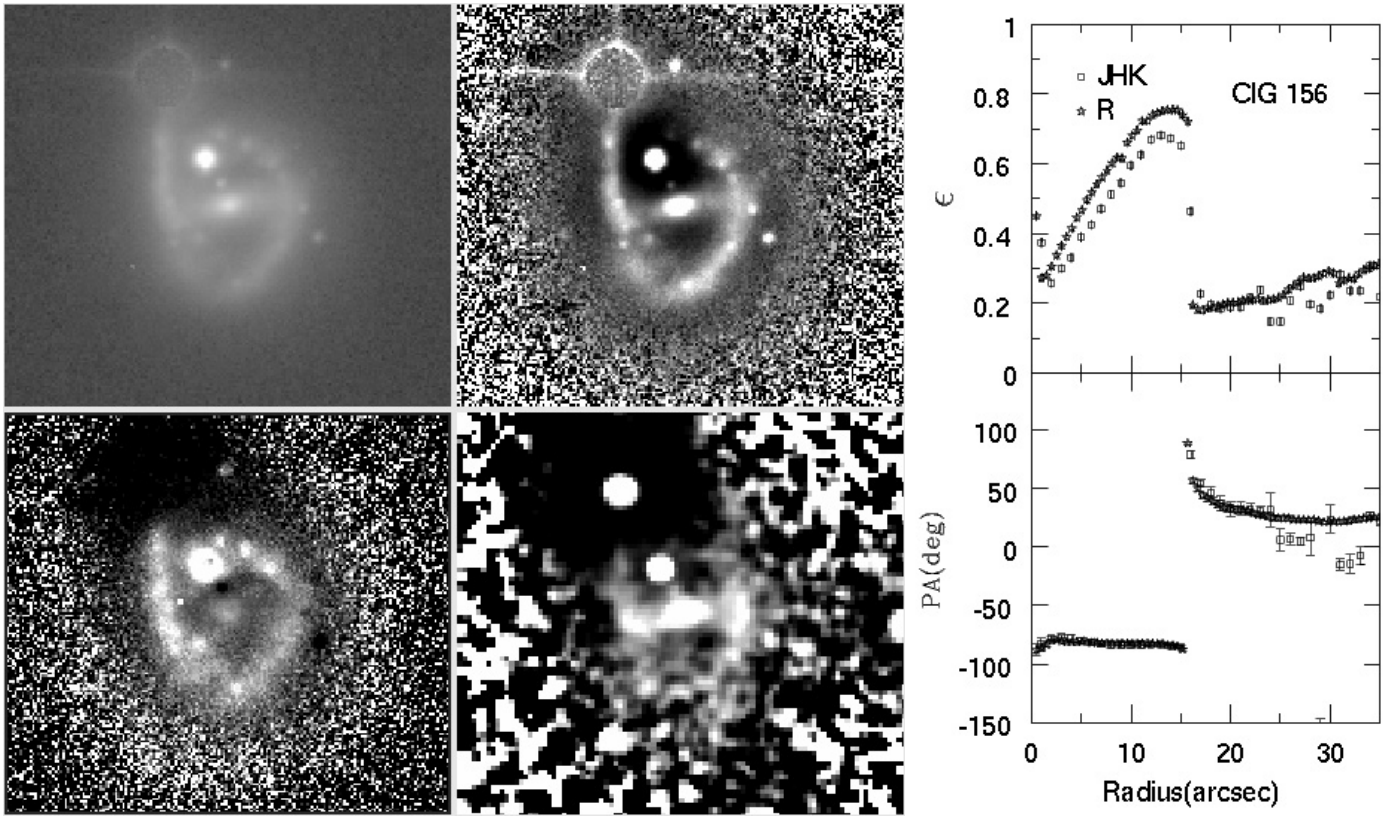

Fig. B.6. CIG 156 Mosaic. Same as Fig. 3. The major diameter of the galaxy in the optical images is 0.8 arcmin.

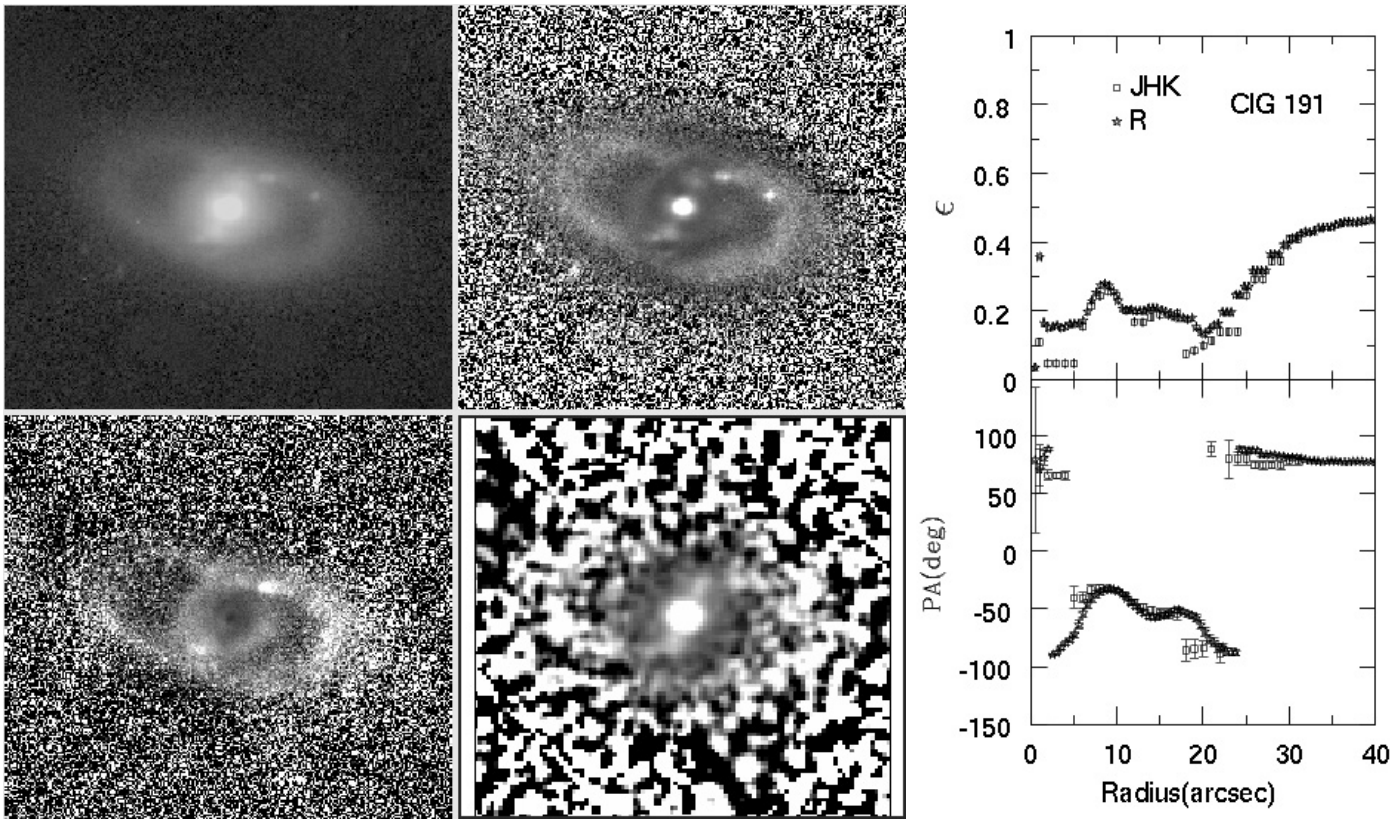

Fig. B.7. CIG 191 Mosaic. Same as Fig. 3. The major diameter of the galaxy in the optical images is 1.2 arcmin.

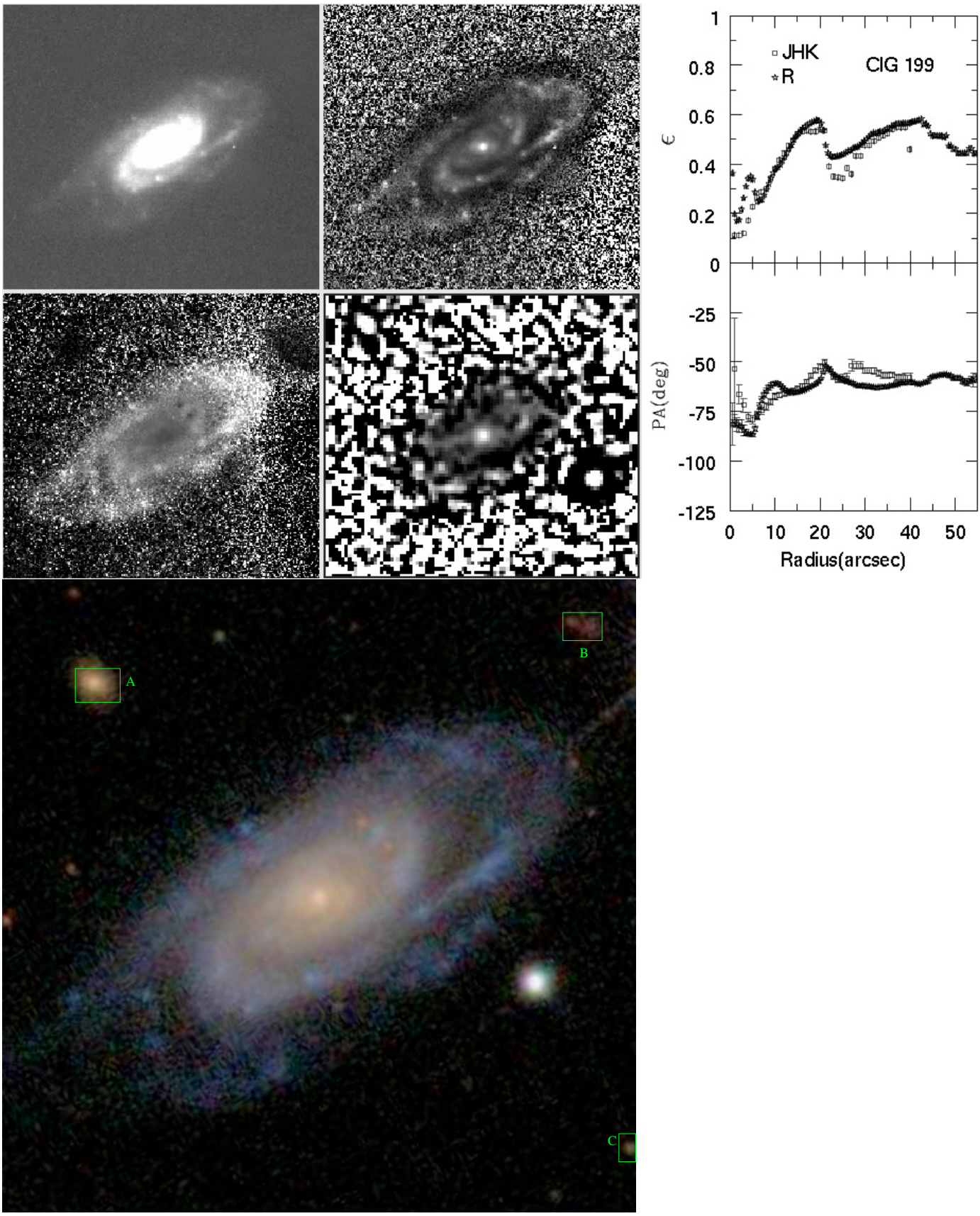

Fig. B.8. CIG 199 Mosaic. Same as Fig. 3. The major diameter of the galaxy in the optical images is 1.5 arcmin.

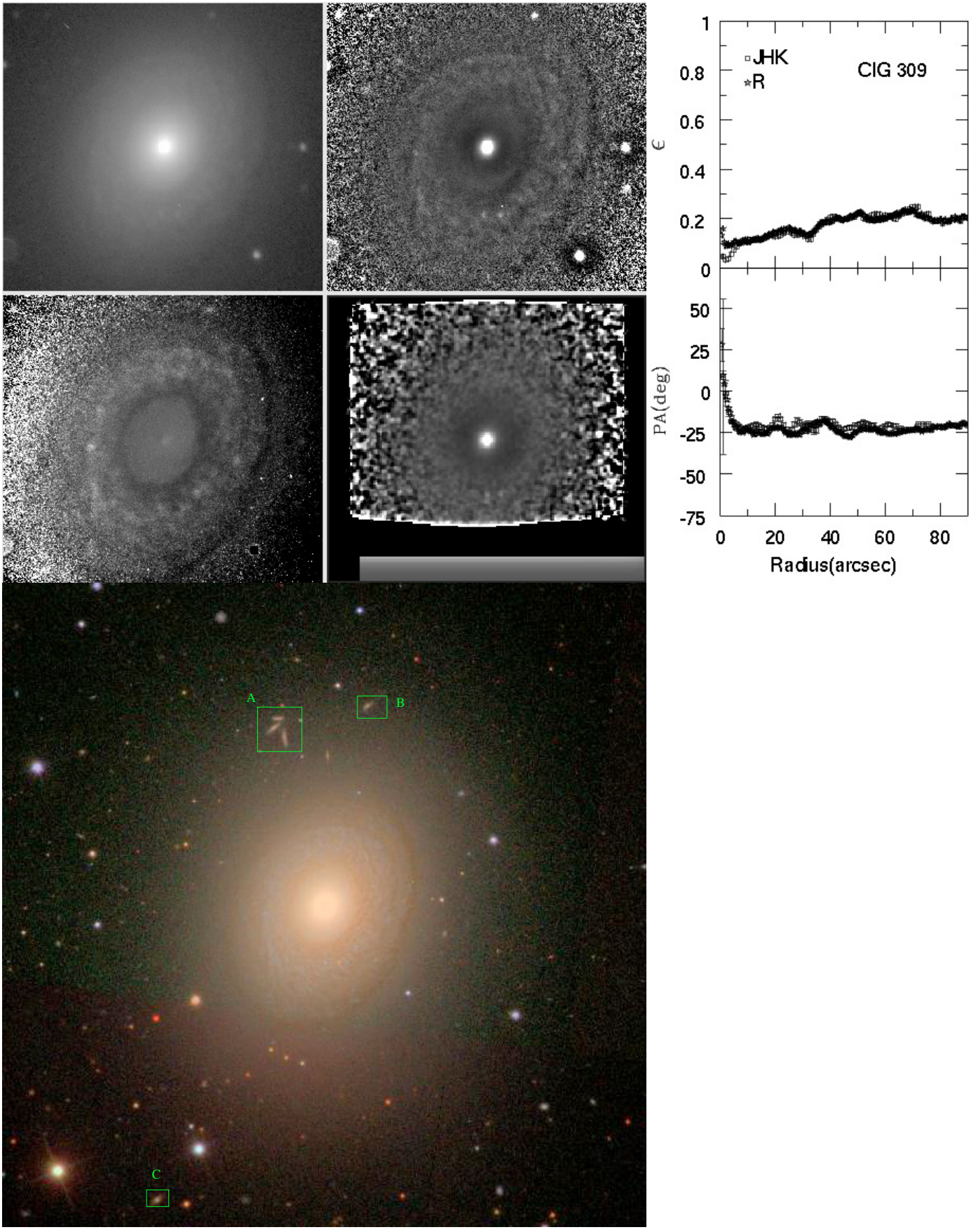

Fig. B.9. CIG 309 Mosaic. Same as Fig. 3. The major diameter of the galaxy in the optical images is 4.3 arcmin.

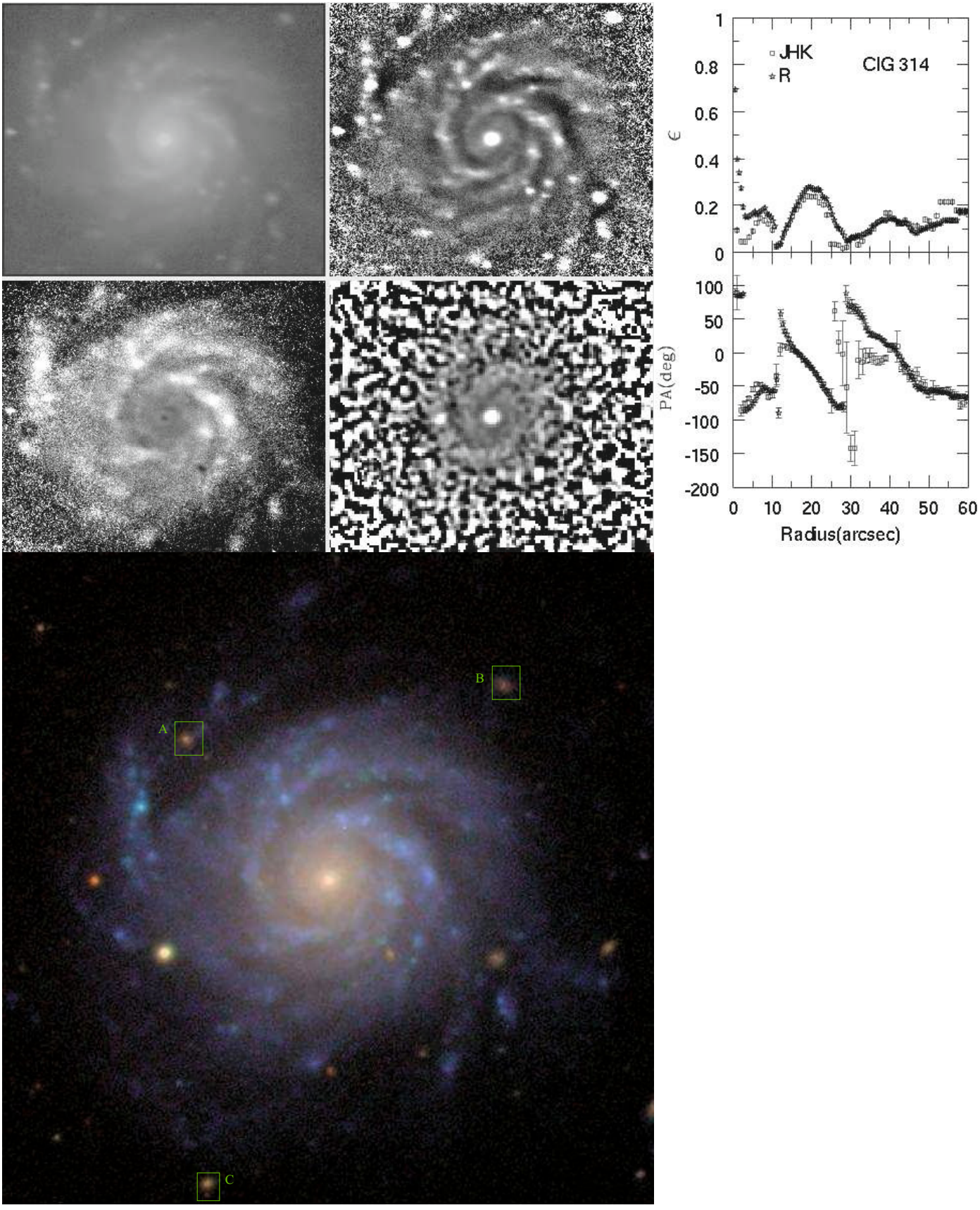

Fig. B.10. CIG 314 Mosaic. Same as Fig. 3. The major diameter of the galaxy in the optical images is 2.3 arcmin.

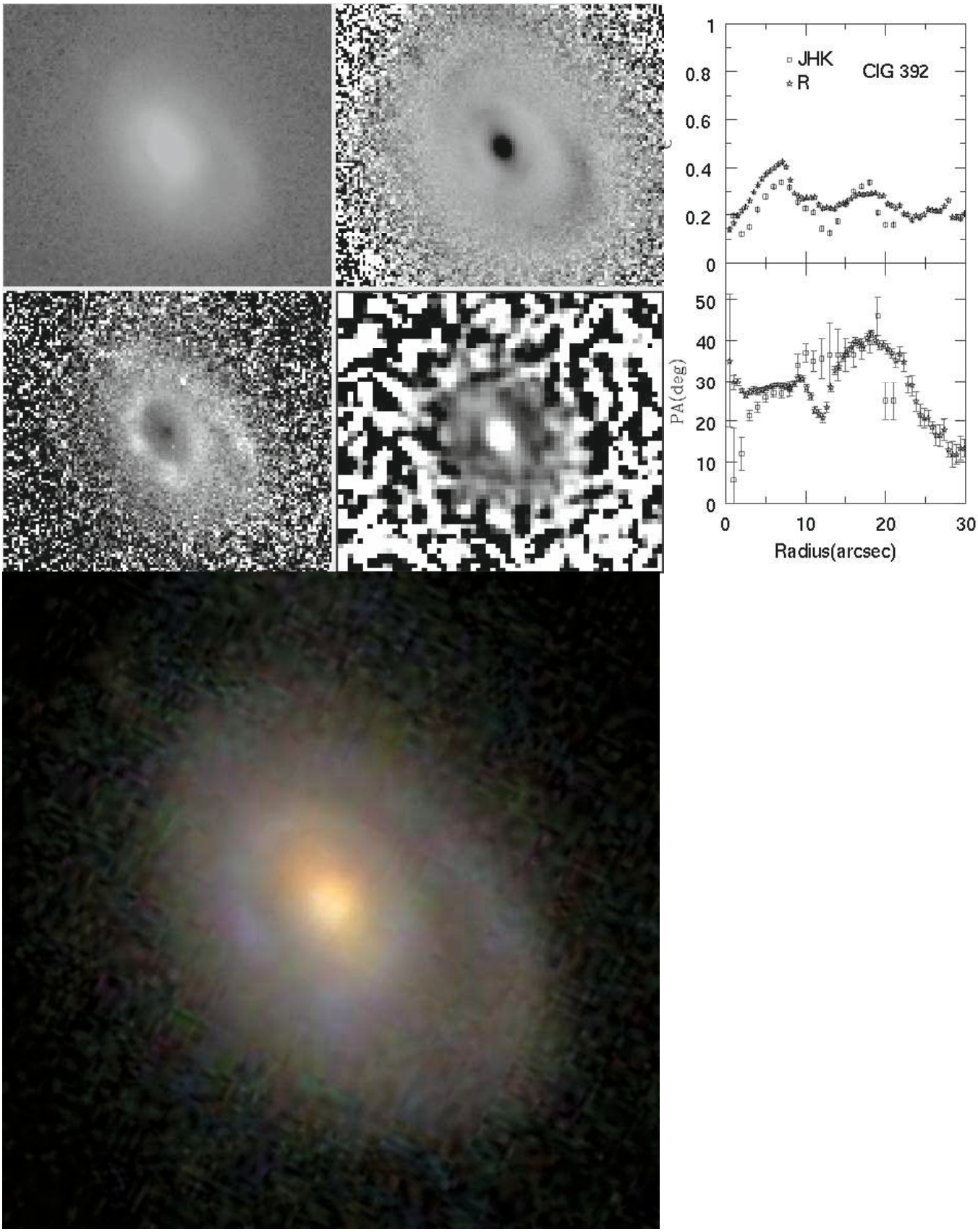

Fig. B.11. CIG 392 Mosaic. Same as Fig. 3. The major diameter of the galaxy in the optical images is 0.8 arcmin.

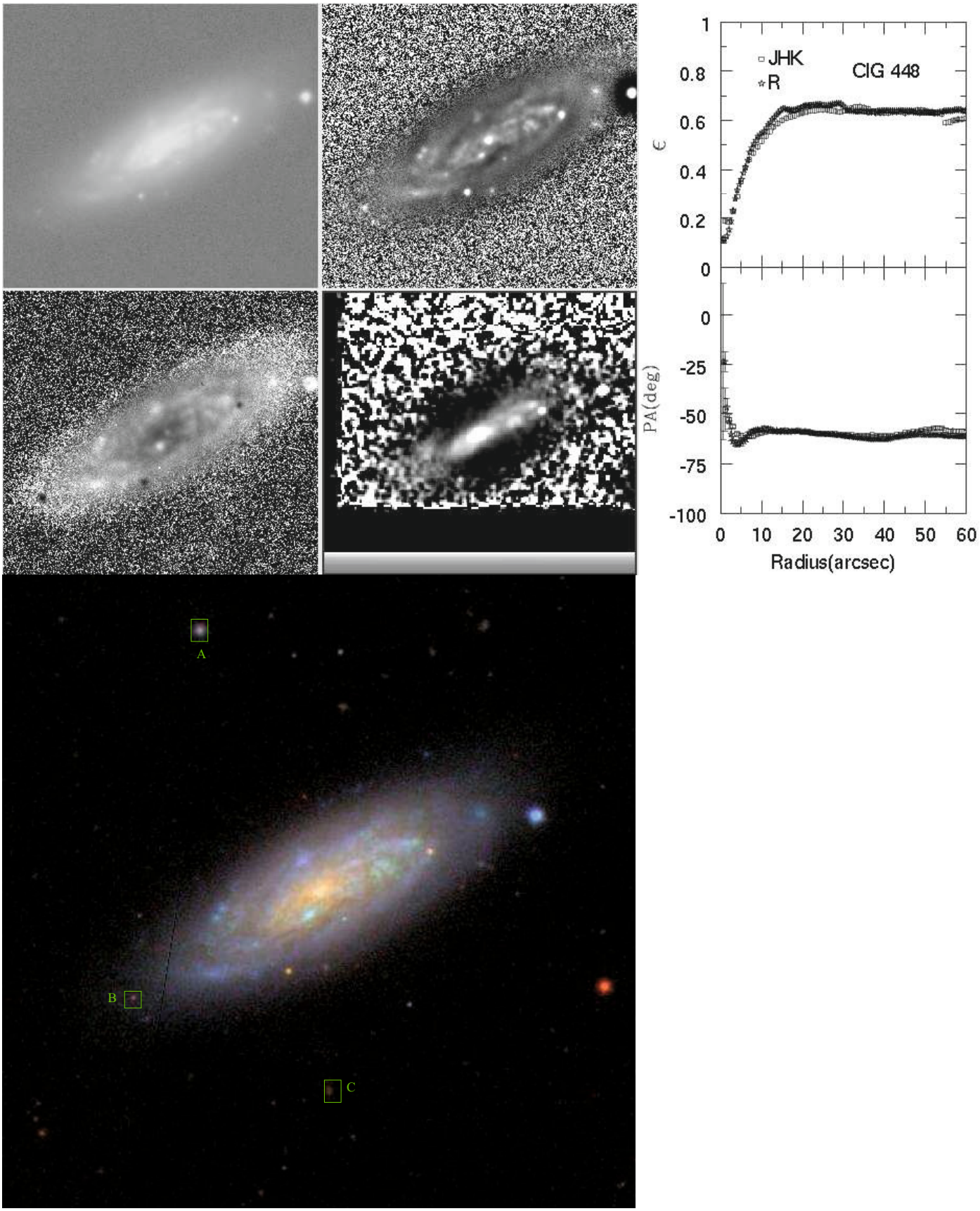

Fig. B.12. CIG 448 Mosaic. Same as Fig. 3. The major diameter of the galaxy in the optical images is 2.5 arcmin.

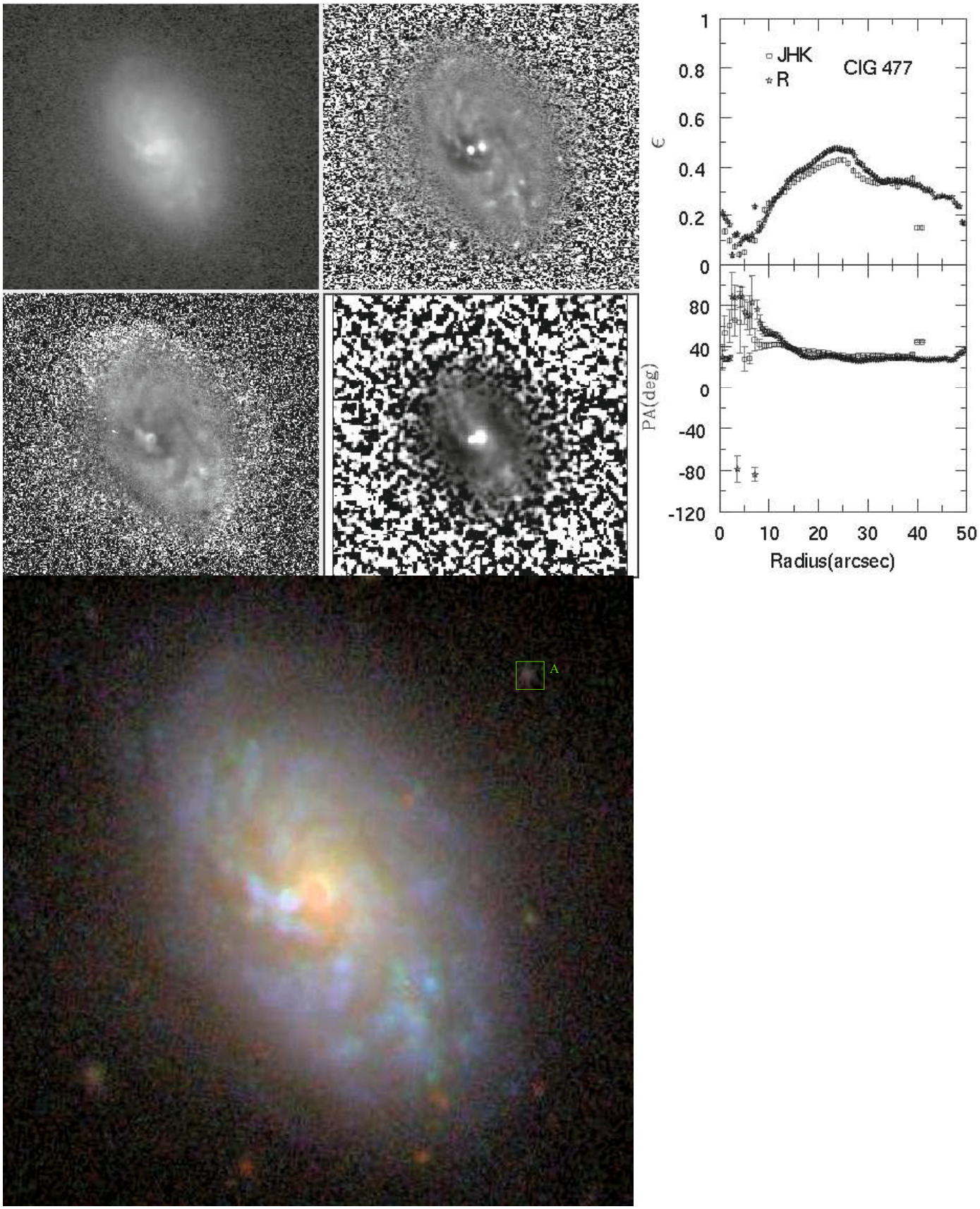

Fig. B.13. CIG 477 Mosaic. Same as Fig. 3. The major diameter of the galaxy in the optical images is 1.5 arcmin.

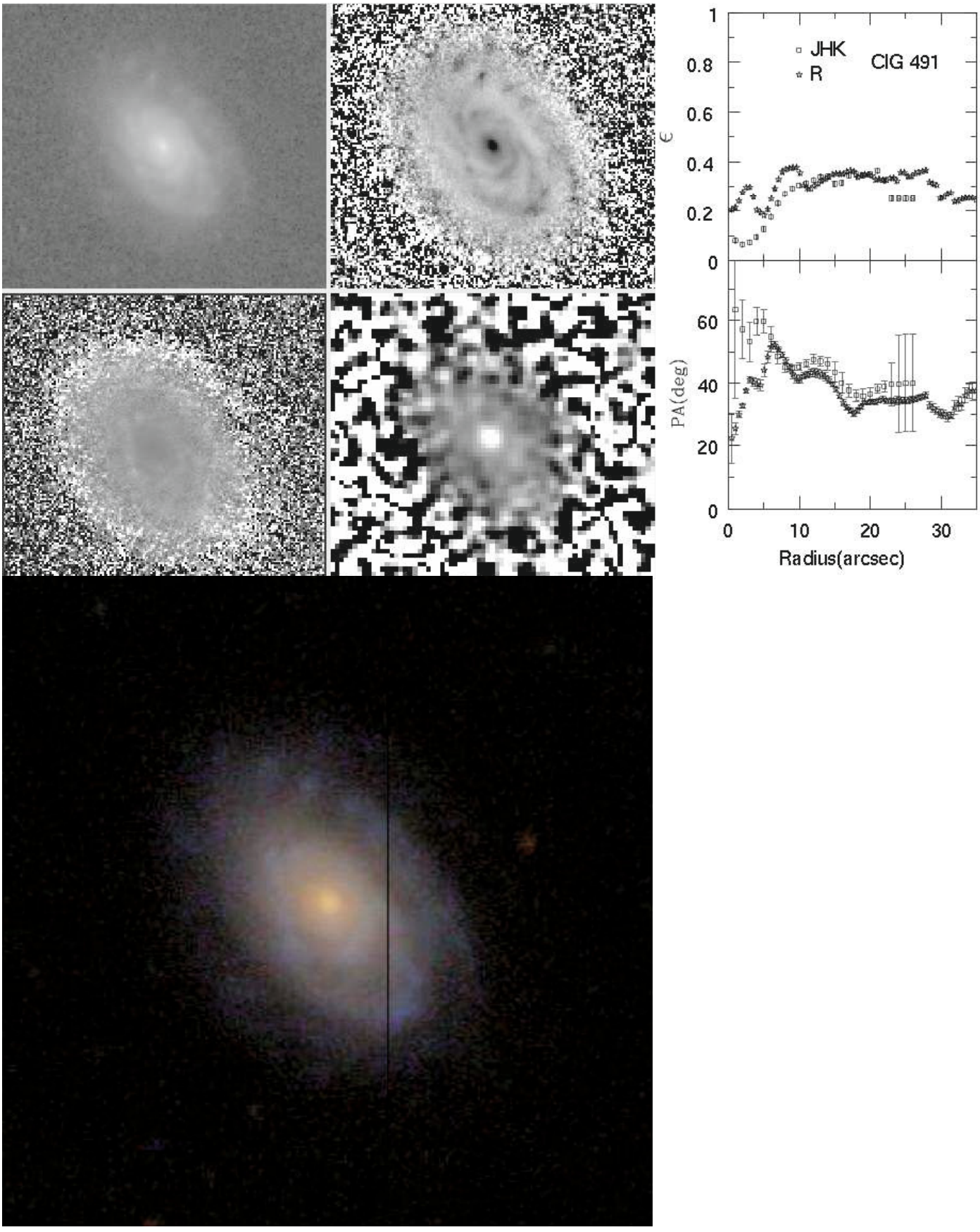

Fig. B.14. CIG 491 Mosaic. Same as Fig. 3. The major diameter of the galaxy in the optical images is 1.0 arcmin.

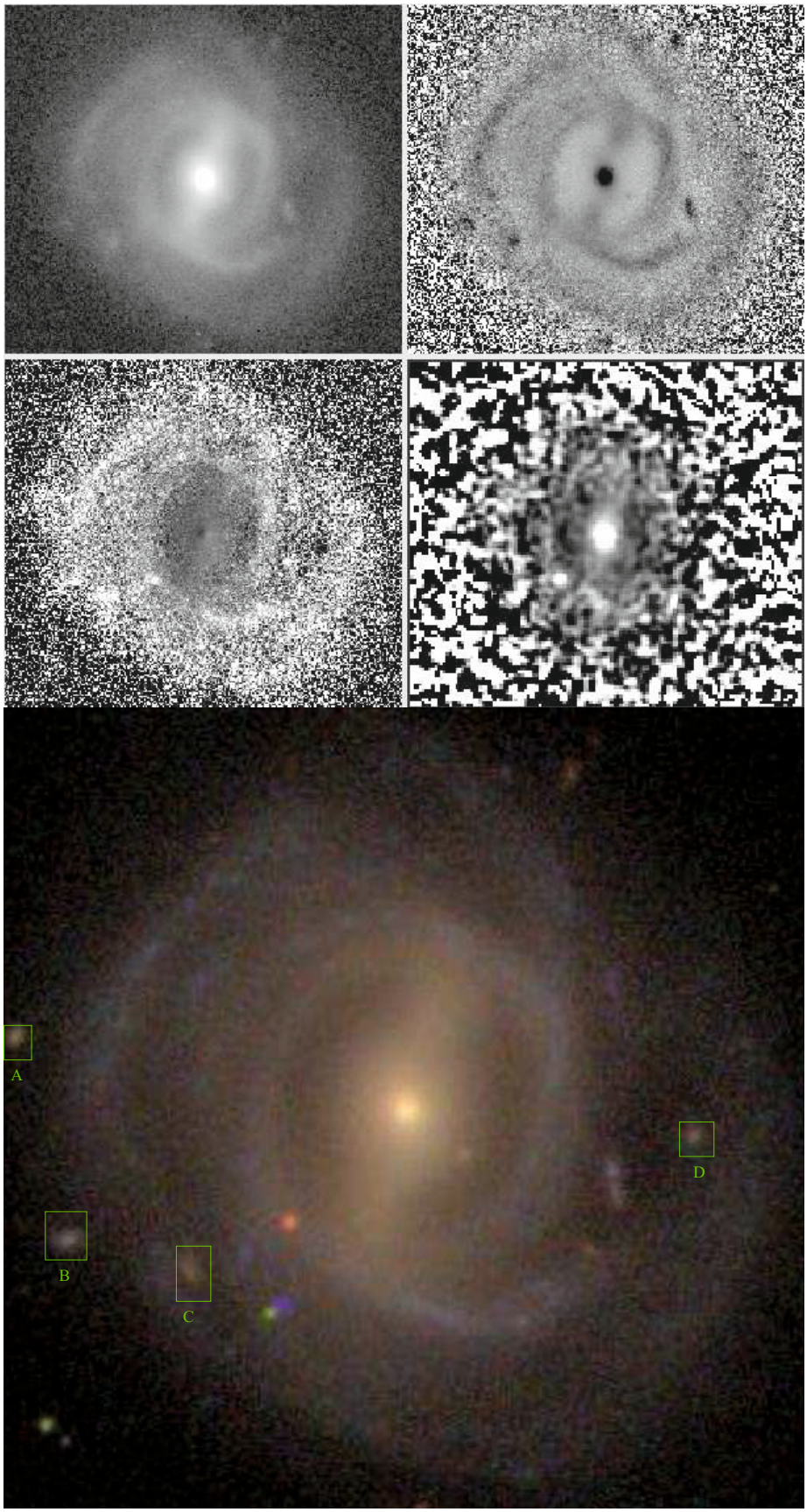

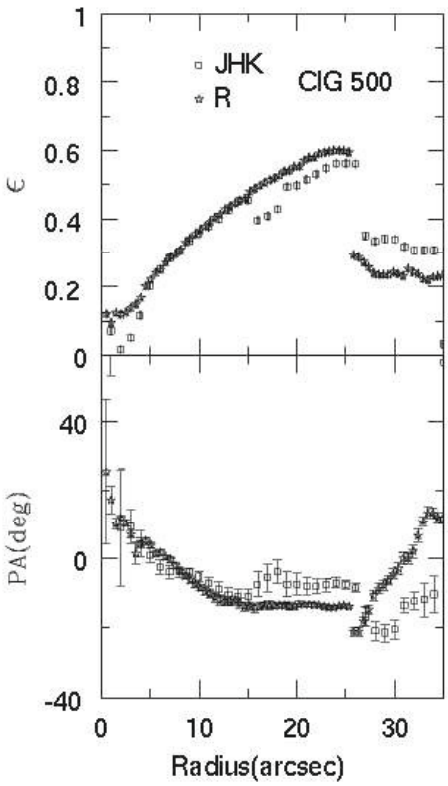

Fig. B.15. CIG 500 Mosaic. Same as Fig. 3. The major diameter of the galaxy in the optical images is 1.6 arcmin.

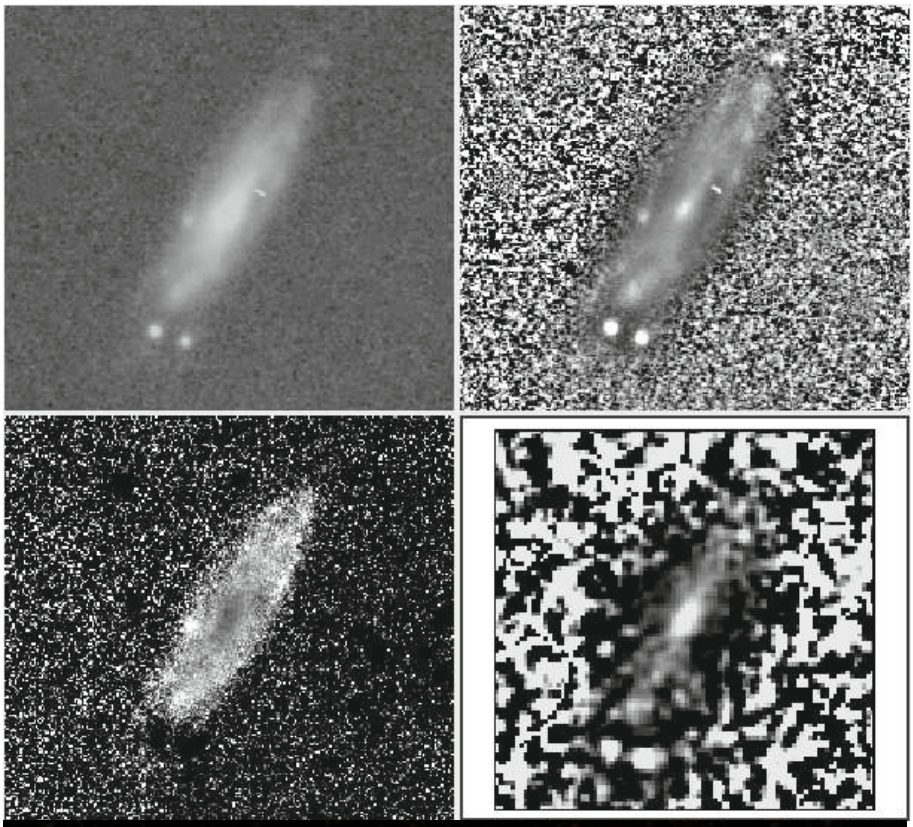

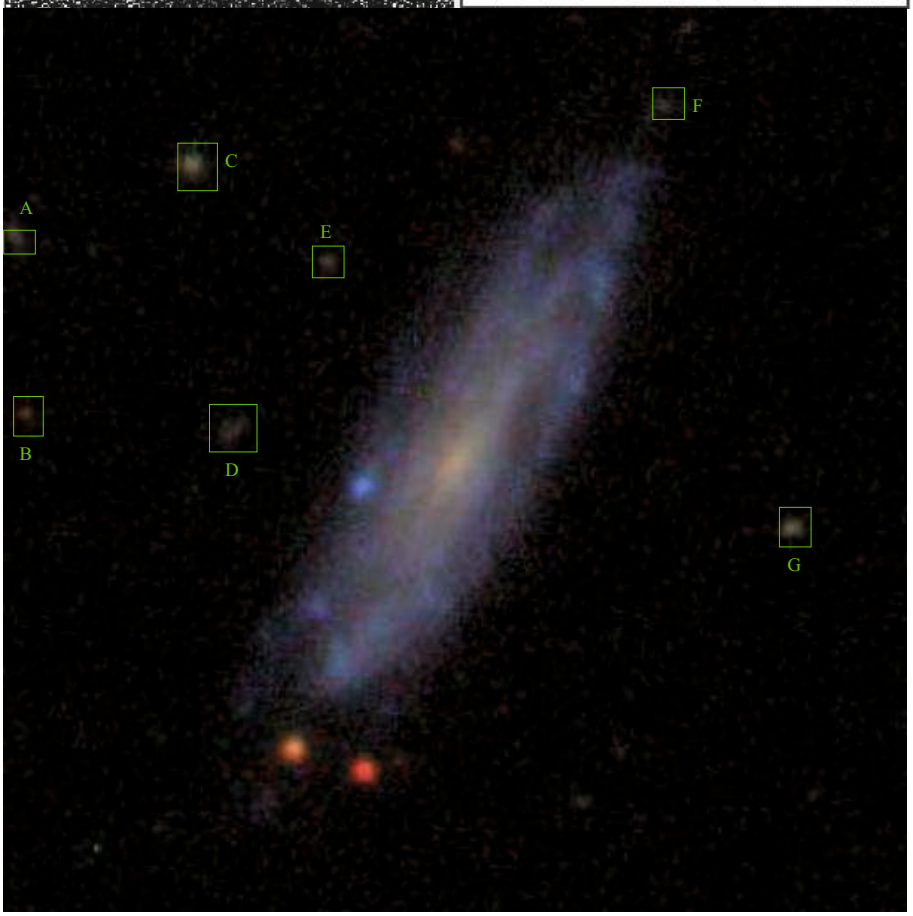

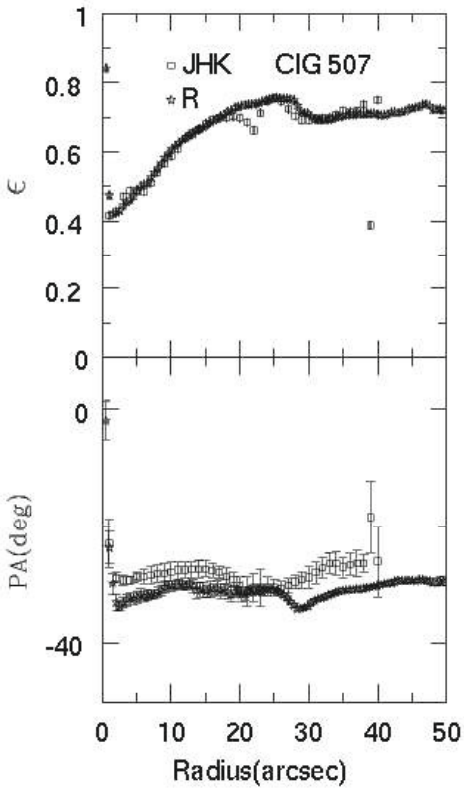

Fig. B.16. CIG 507 Mosaic. Same as Fig. 3. The major diameter of the galaxy in the optical images is 1.5 arcmin.

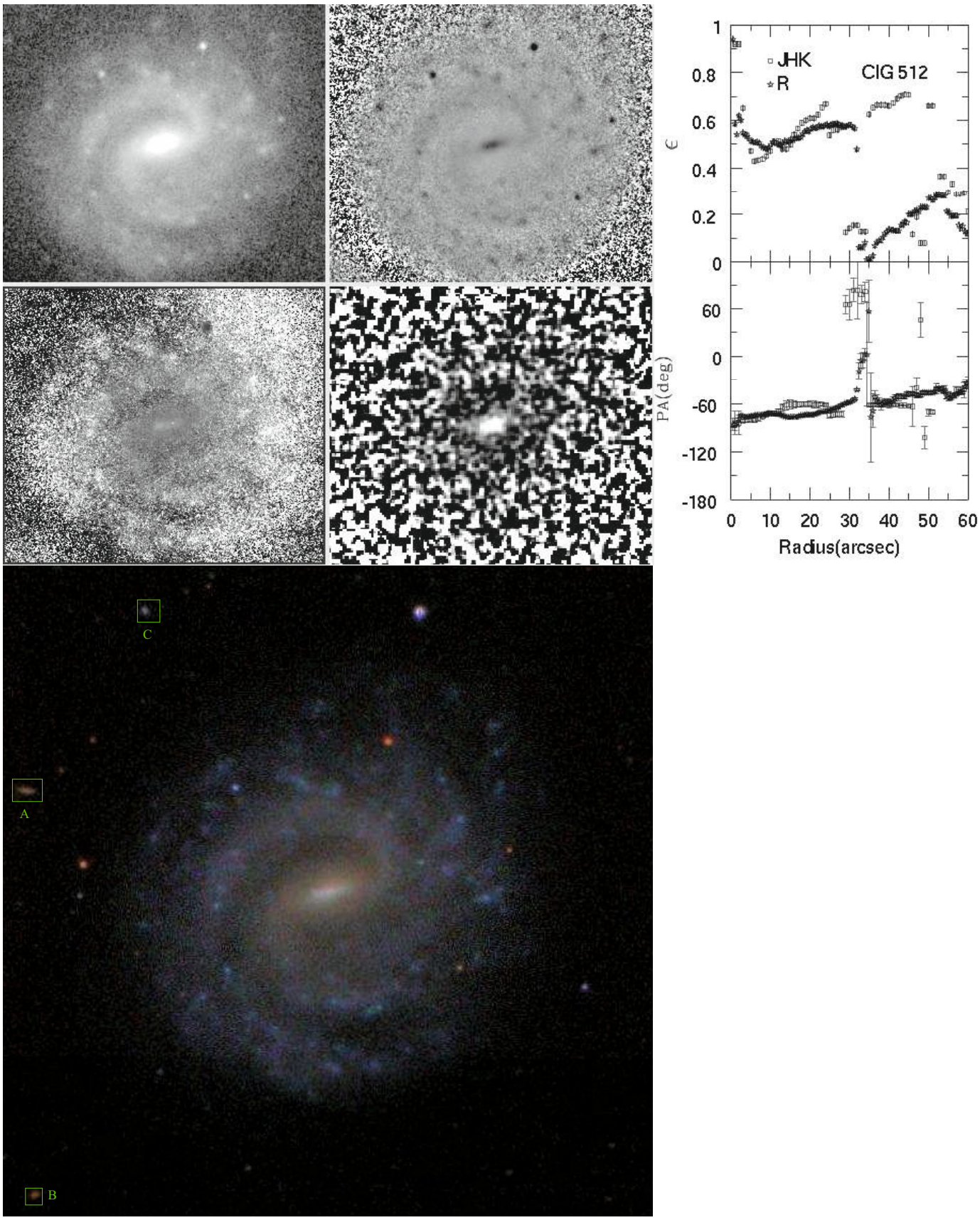

Fig. B.17. CIG 512 Mosaic. Same as Fig. 3. The major diameter of the galaxy in the optical images is 1.6 arcmin.

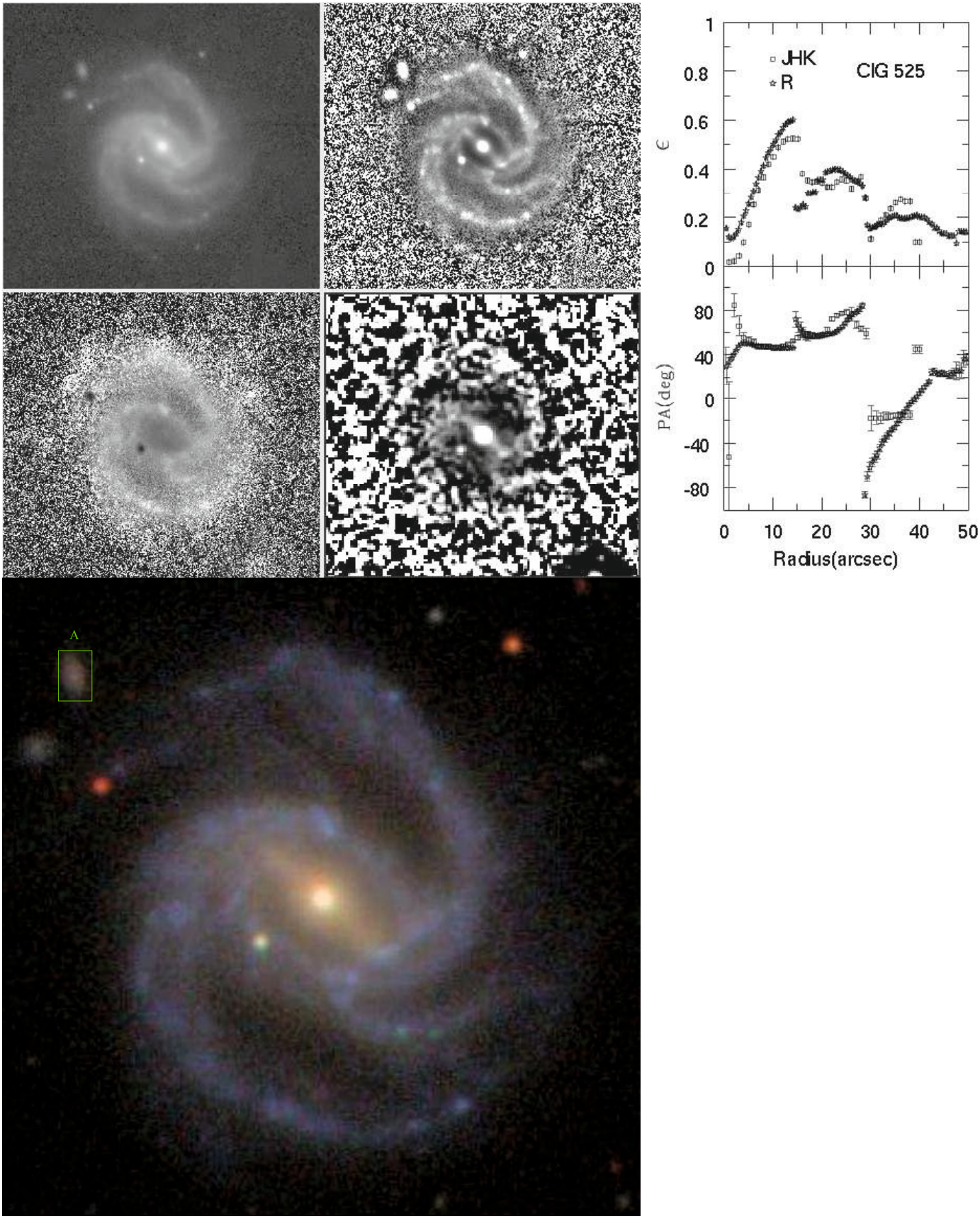

Fig. B.18. CIG 525 Mosaic. Same as Fig. 3. The major diameter of the galaxy in the optical images is 1.4 arcmin.

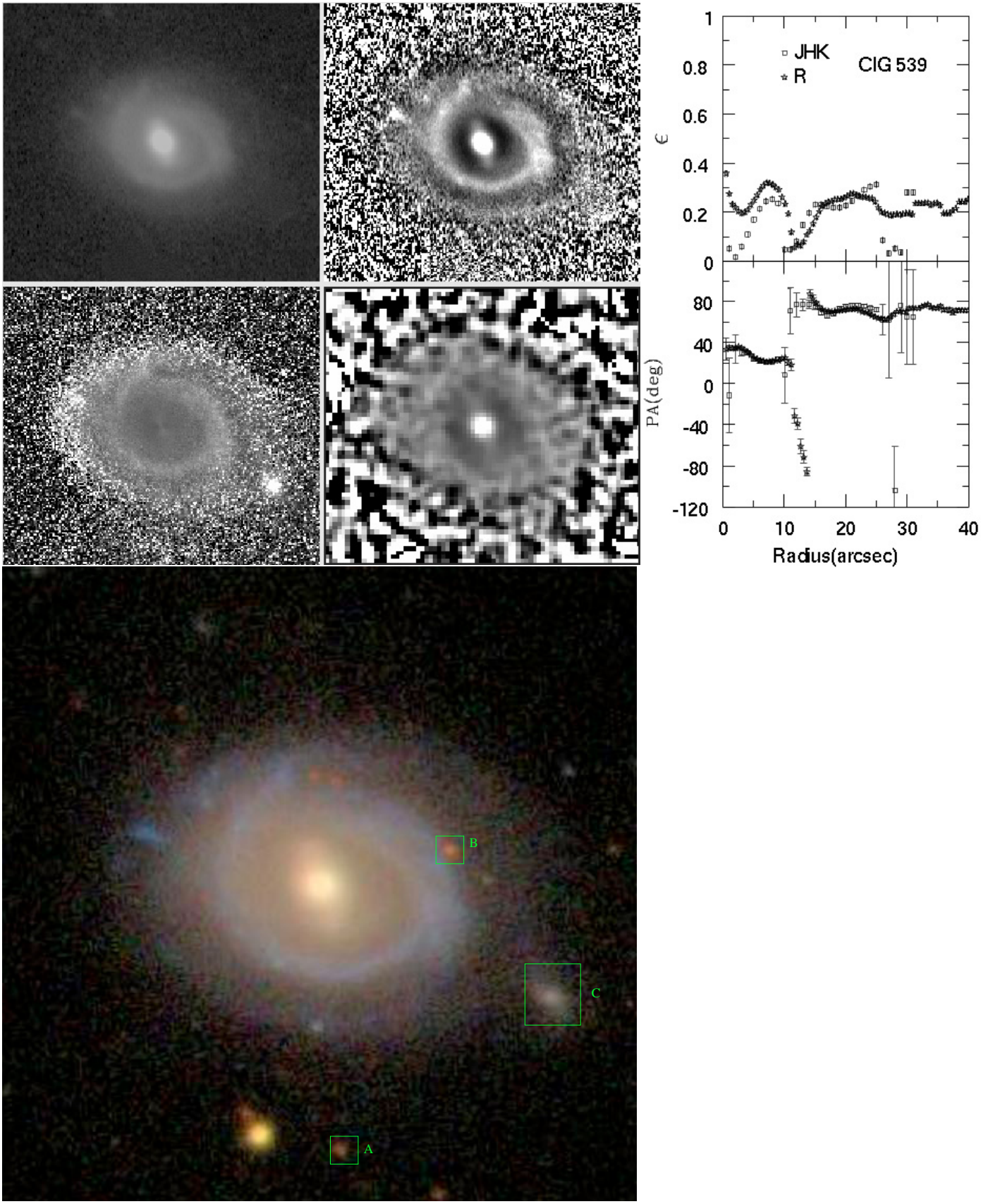

Fig. B.19. CIG 539 Mosaic. Same as Fig. 3. The major diameter of the galaxy in the optical images is 1.1 arcmin.

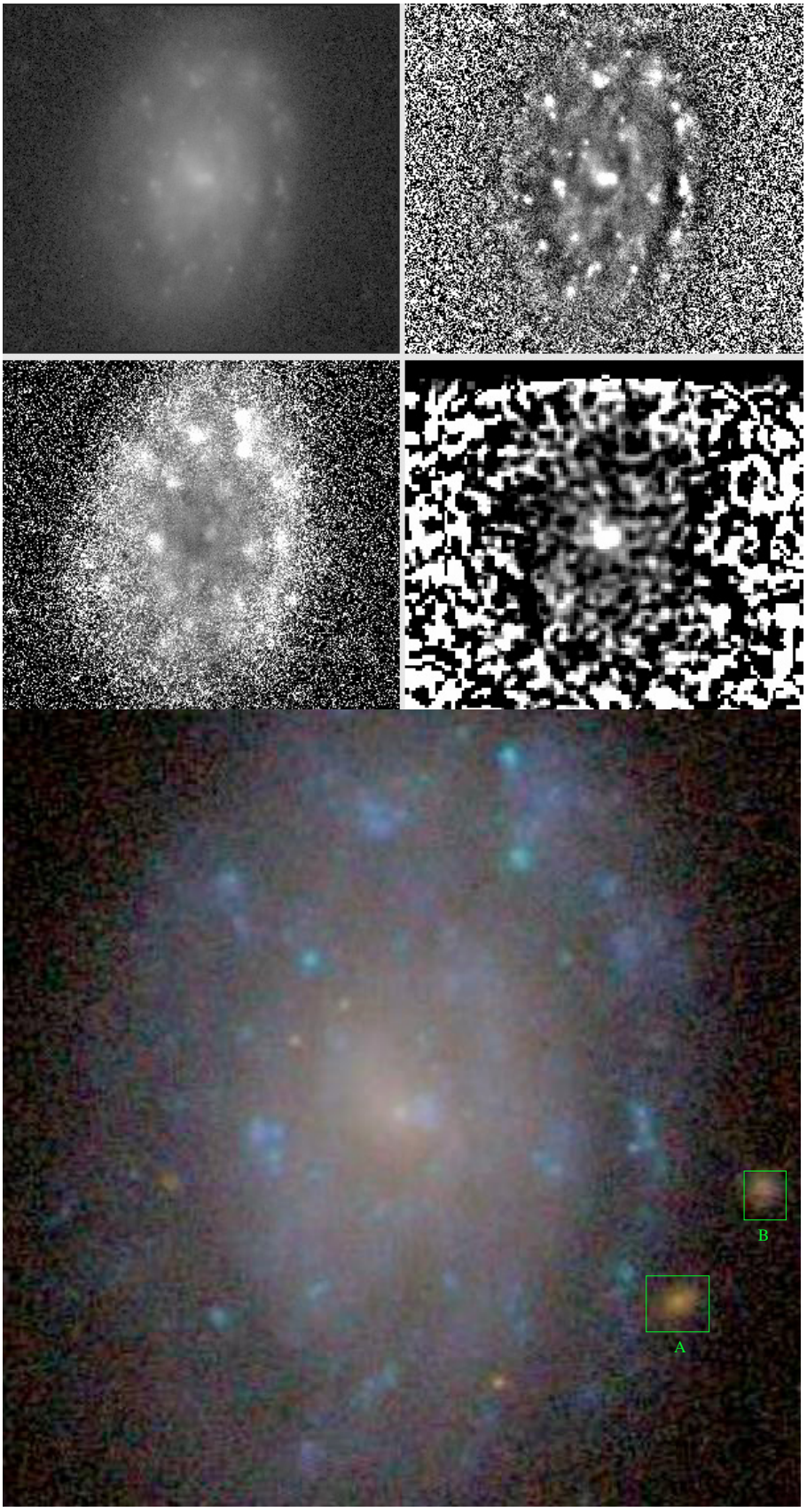

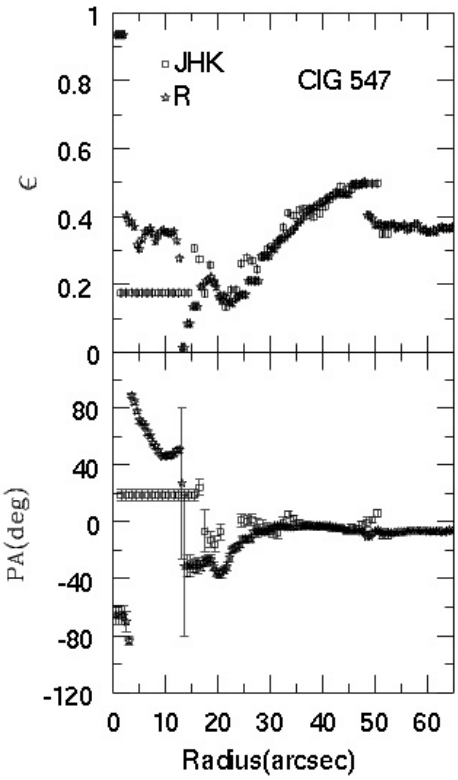

Fig. B.20. CIG 547 Mosaic. Same as Fig. 3. The major diameter of the galaxy in the optical images is 2.0 arcmin.

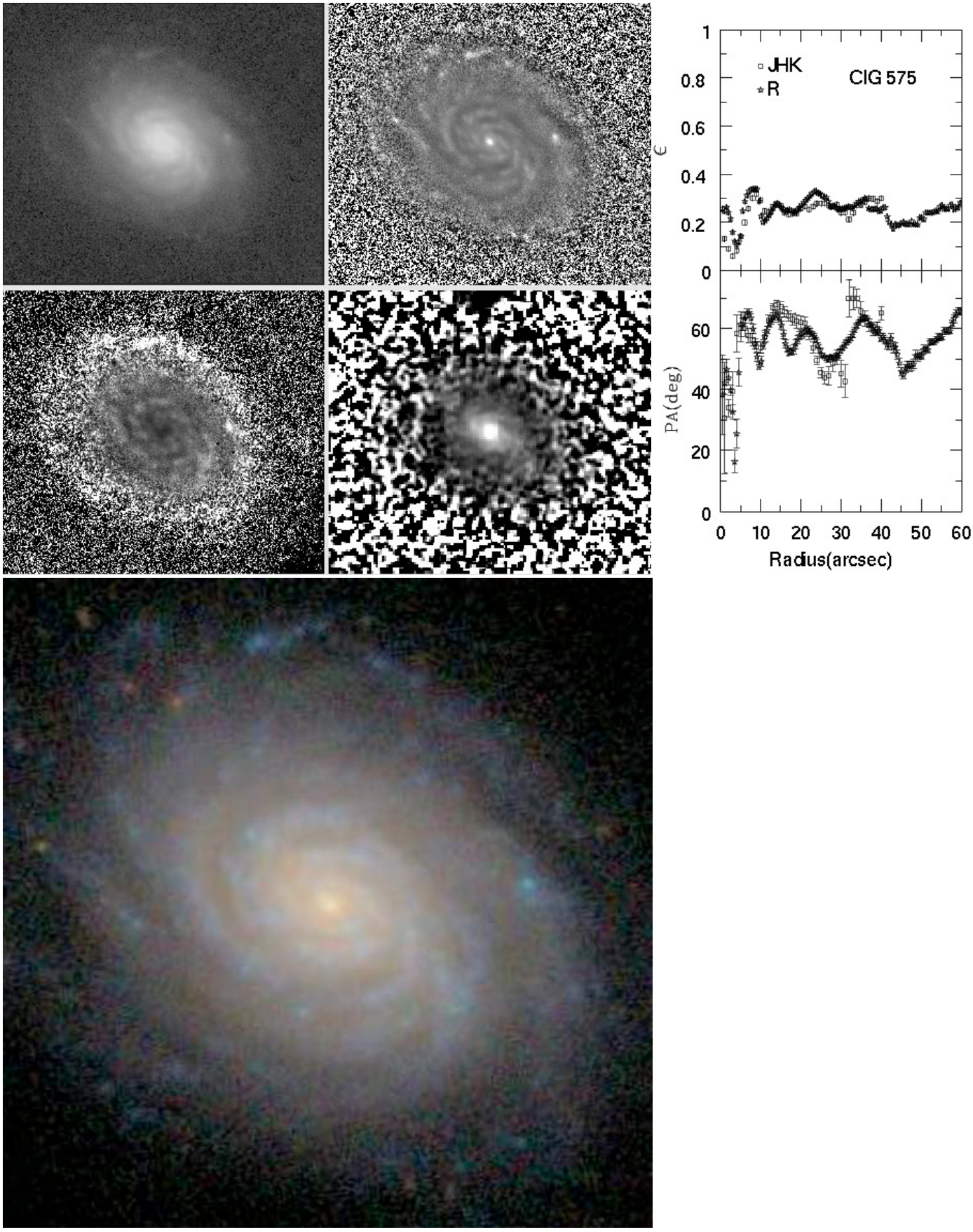

Fig. B.21. CIG 575 Mosaic. Same as Fig. 3. The major diameter of the galaxy in the optical images is 1.7 arcmin.

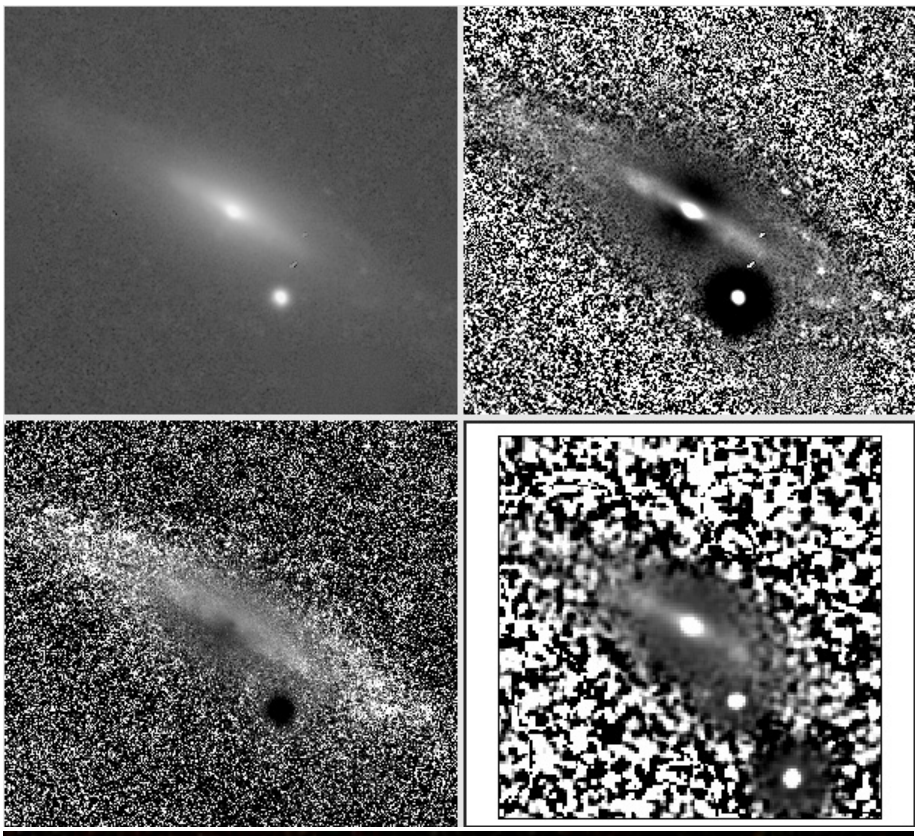

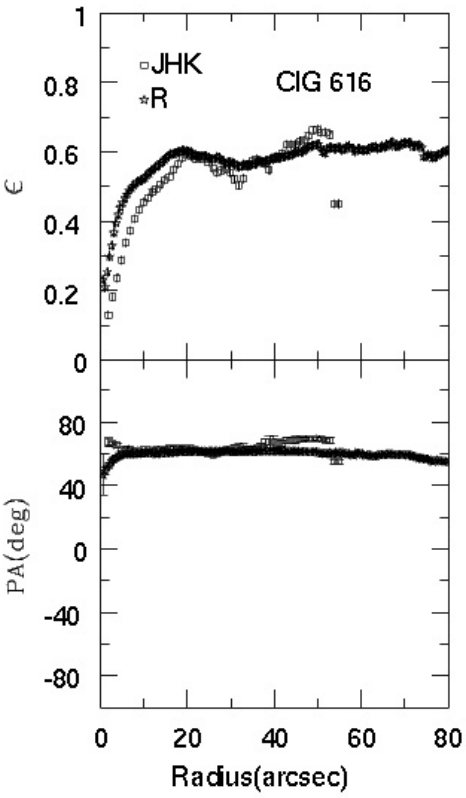

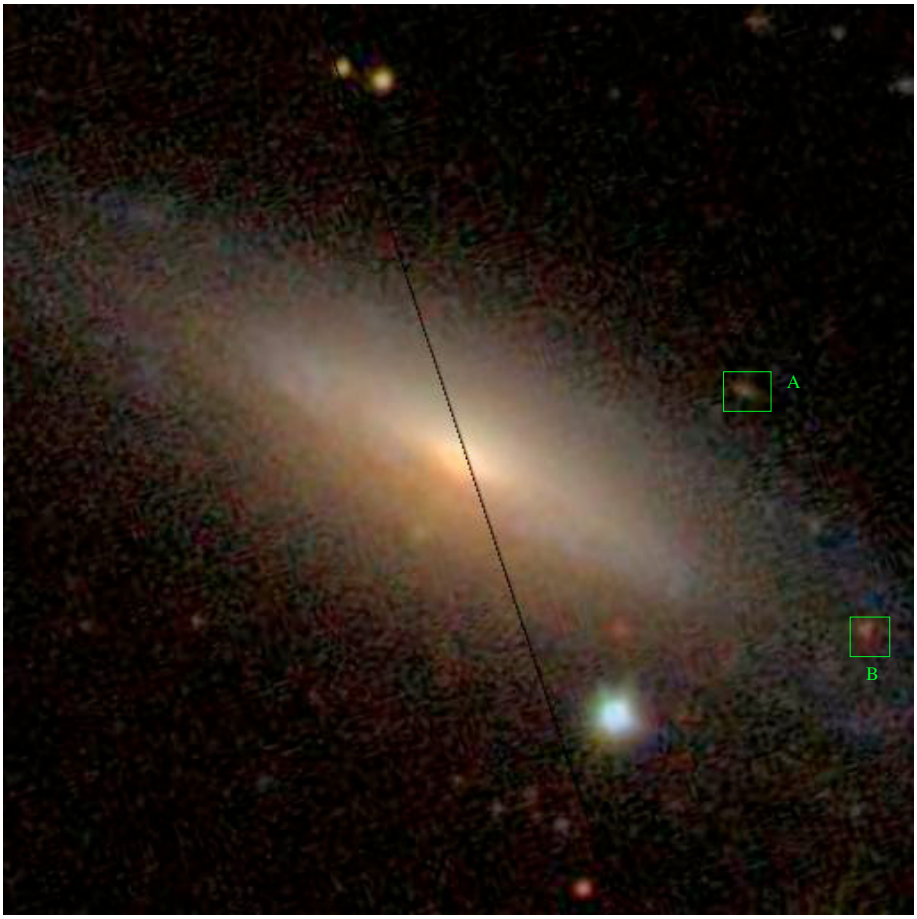

Fig. B.22. CIG 616 Mosaic. Same as Fig. 3. The major diameter of the galaxy in the optical images is 2.6 arcmin.

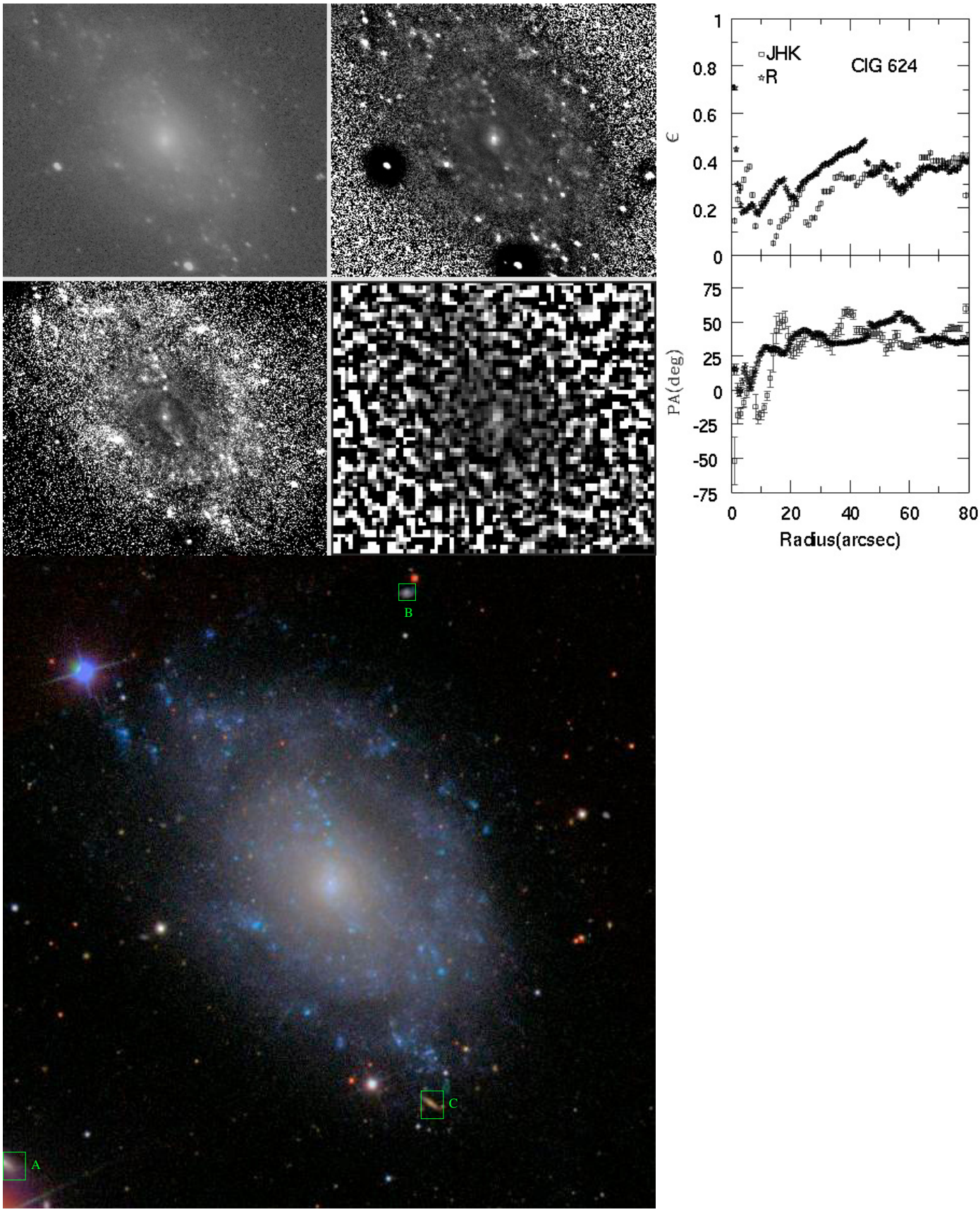

Fig. B.23. CIG 624 Mosaic. Same as Fig. 3. The major diameter of the galaxy in the optical images is 5.8 arcmin.

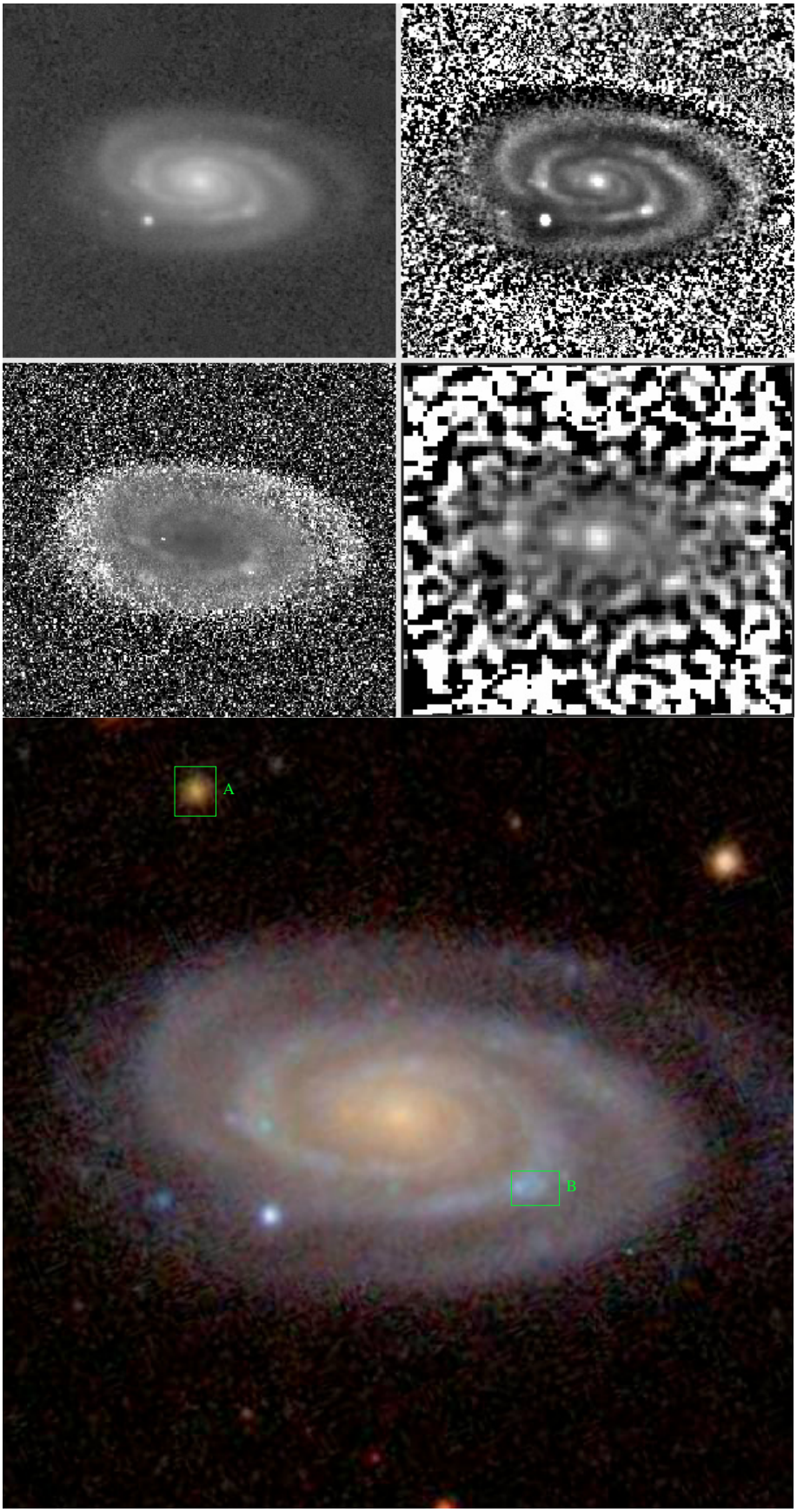

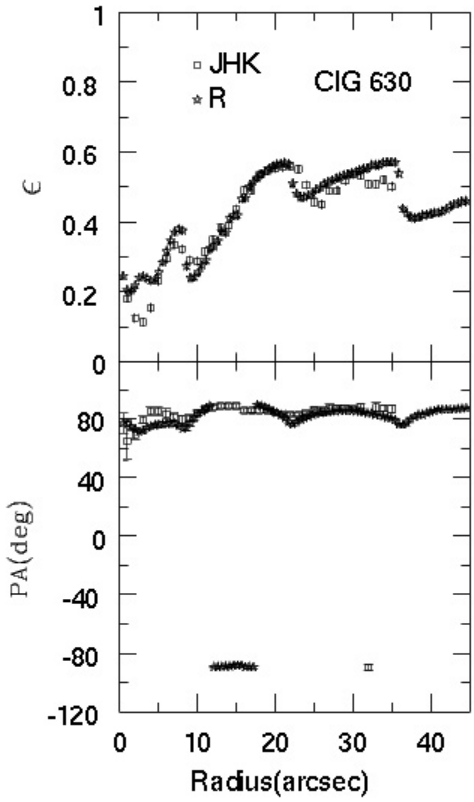

Fig. B.24. CIG 630 Mosaic. Same as Fig. 3. The major diameter of the galaxy in the optical images is 1.6 arcmin.

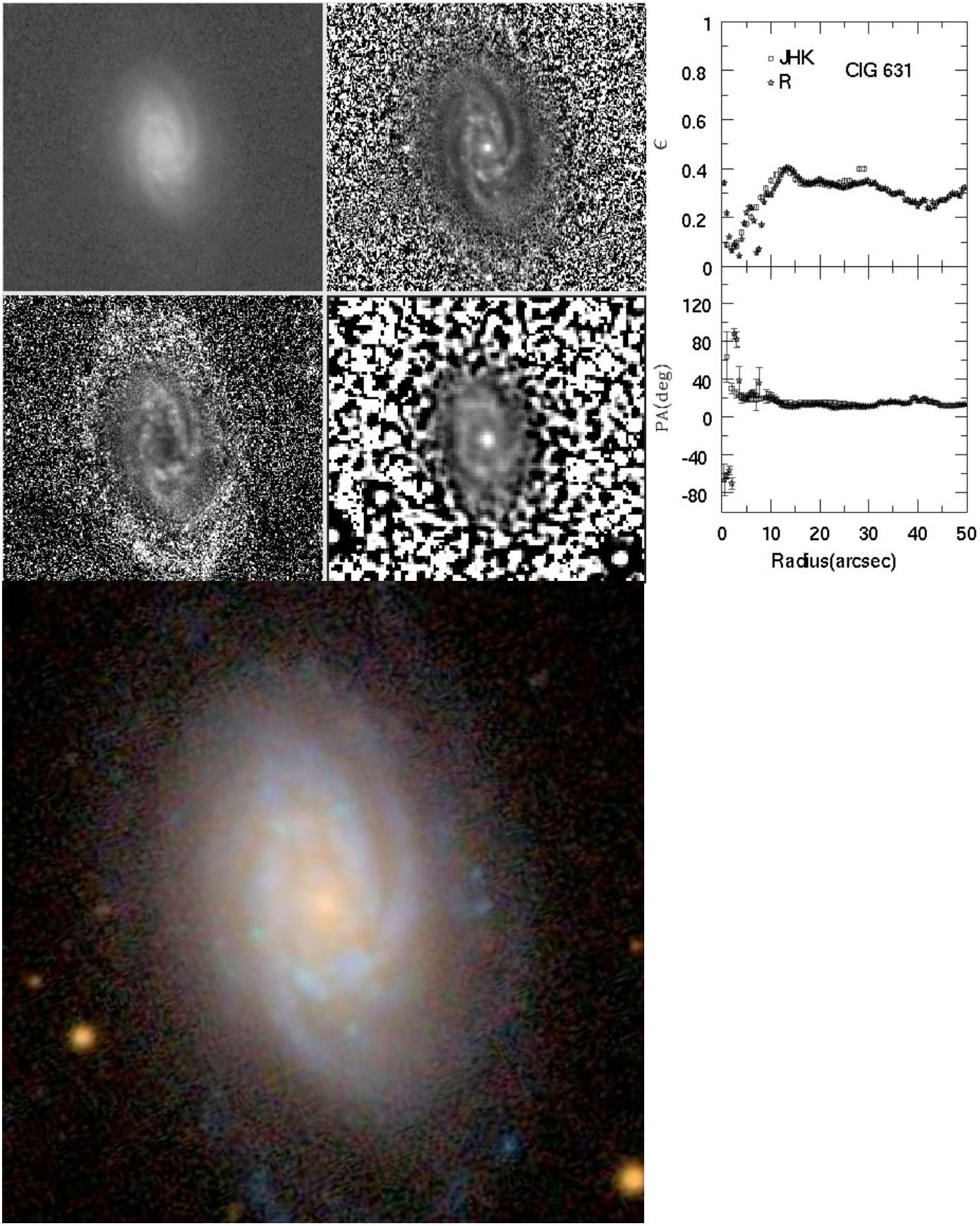

Fig. B.25. CIG 631 Mosaic. Same as Fig. 3. The major diameter of the galaxy in the optical images is 1.6 arcmin.

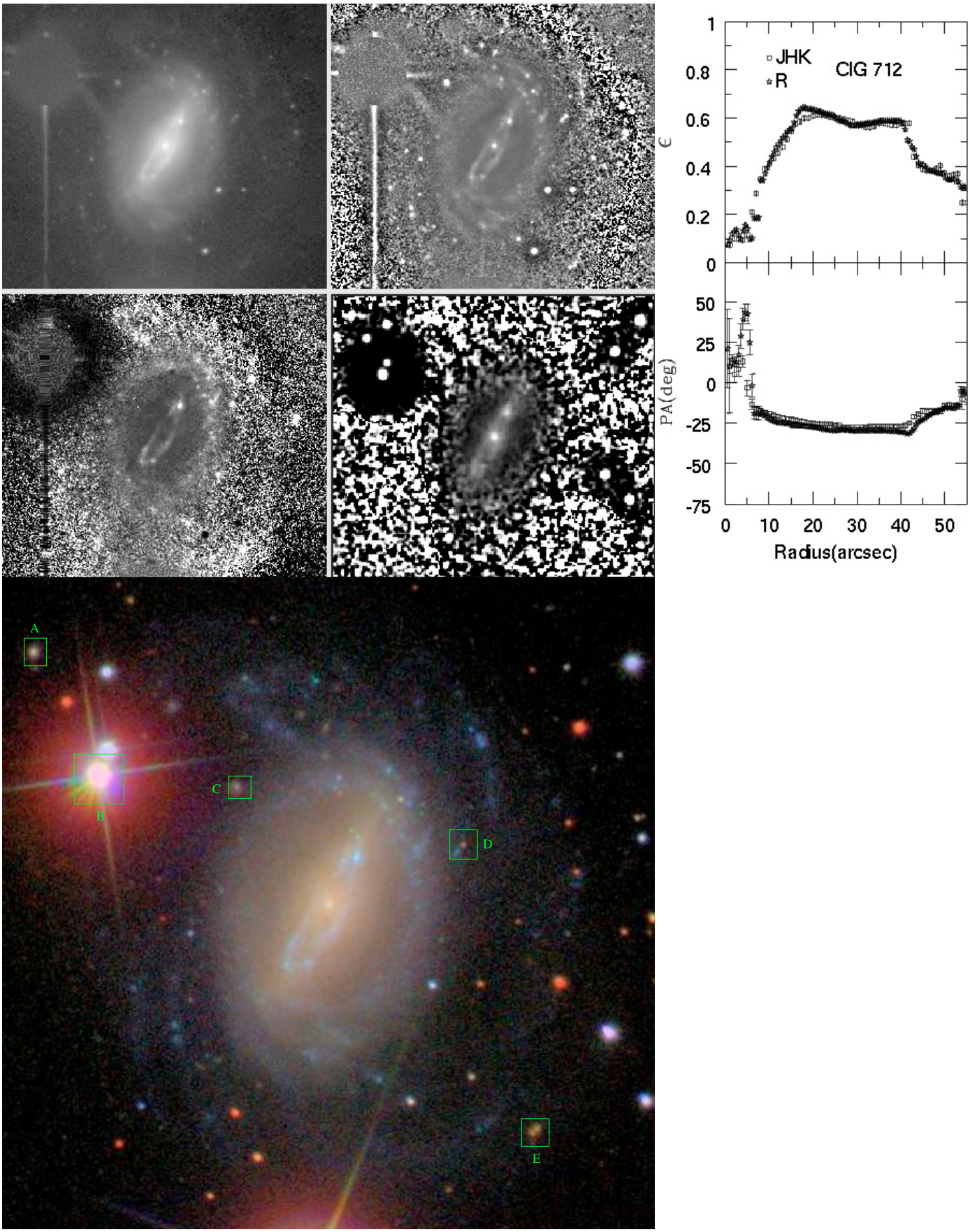

Fig. B.26. CIG 712 Mosaic. Same as Fig. 3. The major diameter of the galaxy in the optical images is 2.1 arcmin.

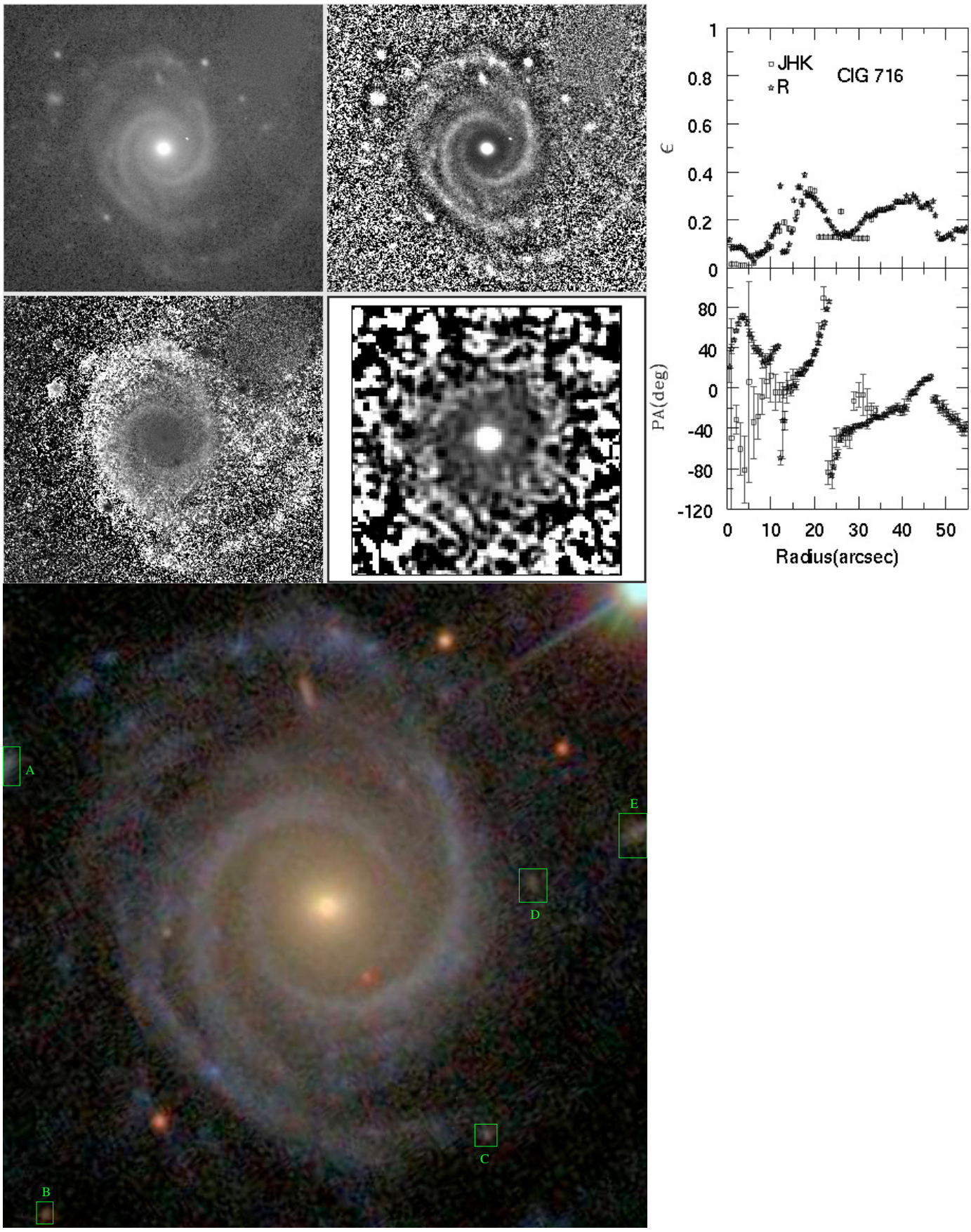

Fig. B.27. CIG 716 Mosaic. Same as Fig. 3. The major diameter of the galaxy in the optical images is 2.7 arcmin.

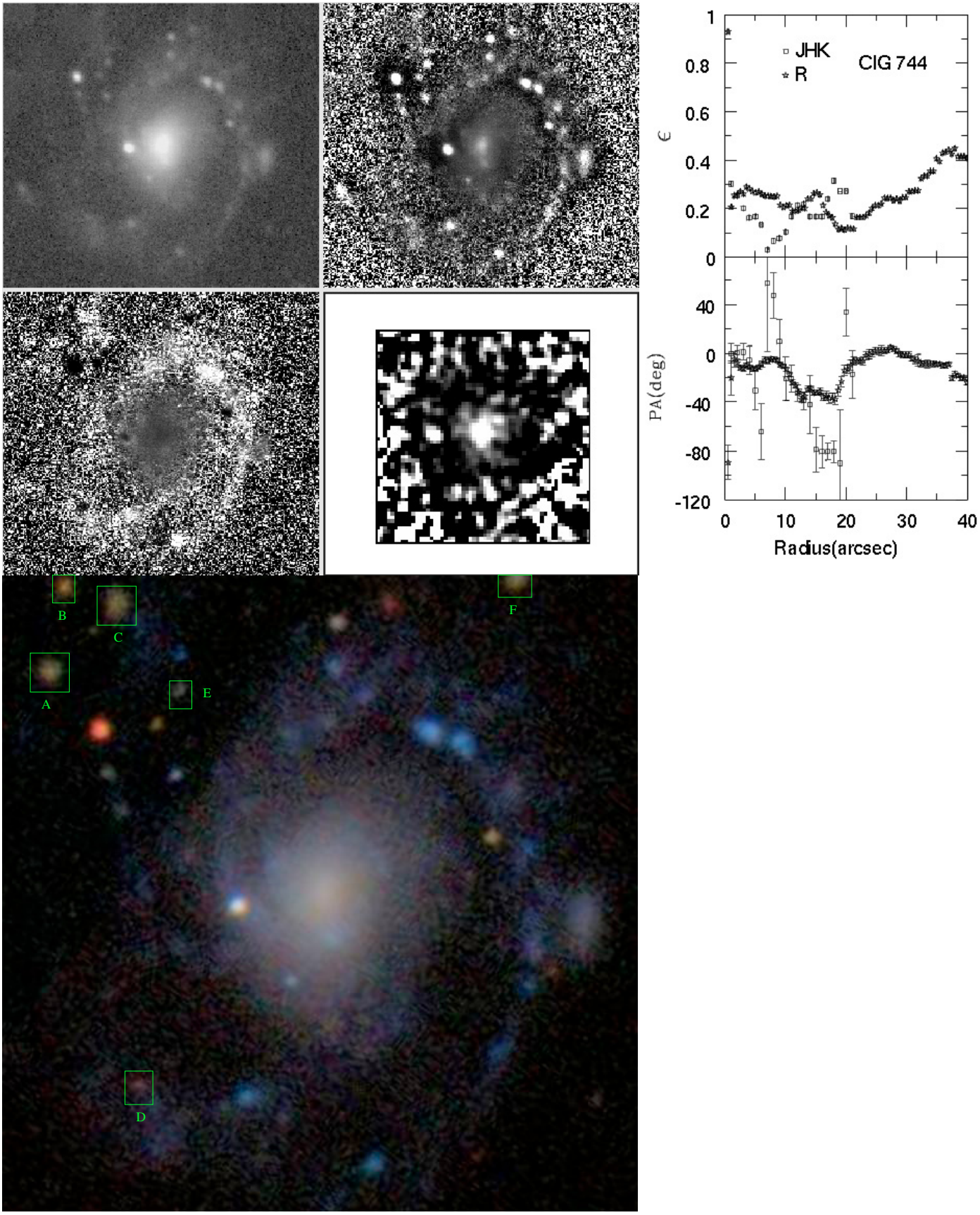

Fig. B.28. CIG 744 Mosaic. Same as Fig. 3. The major diameter of the galaxy in the optical images is 0.8 arcmin.

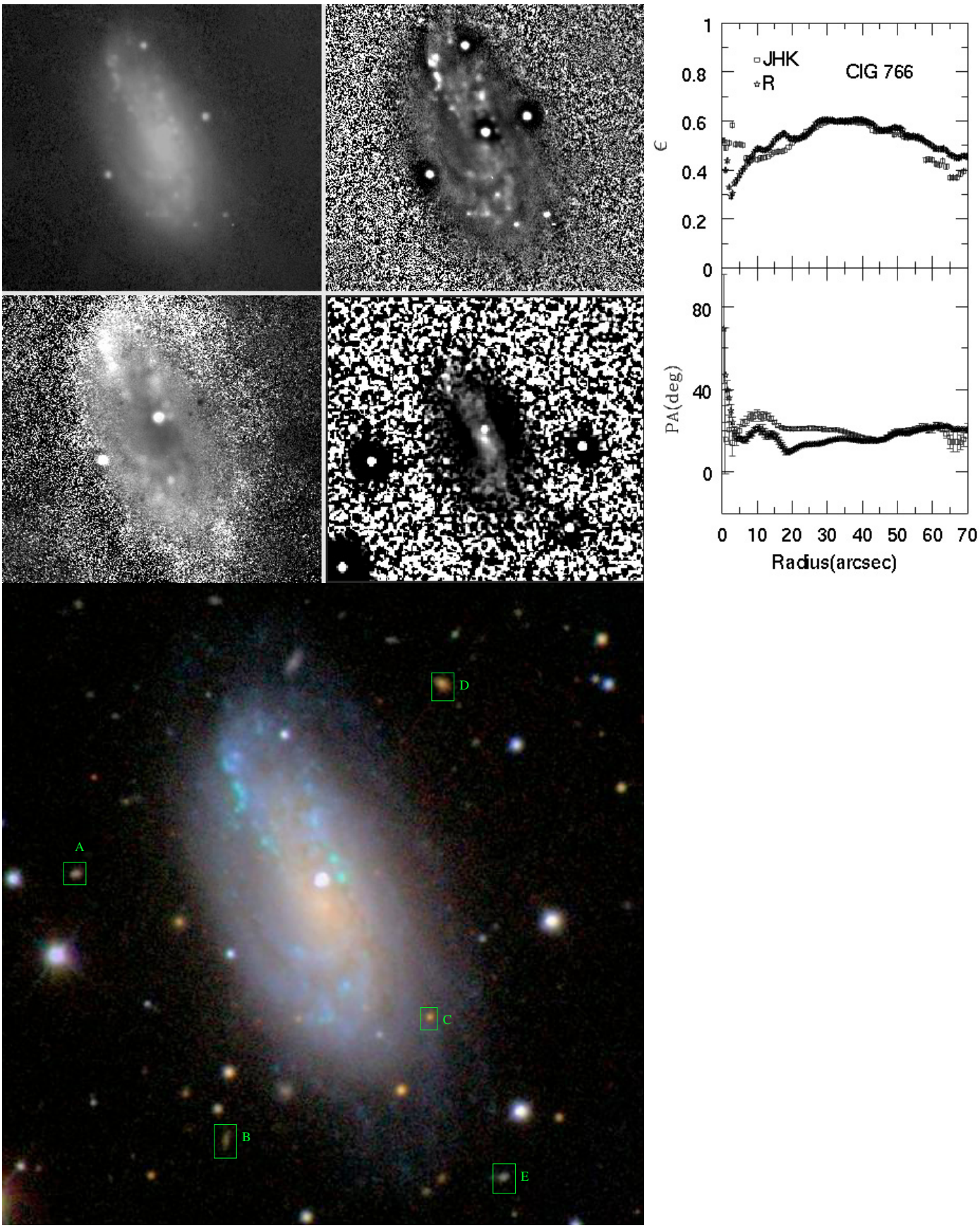

Fig. B.29. CIG 766 Mosaic. Same as Fig. 3. The major diameter of the galaxy in the optical images is 3.0 arcmin.

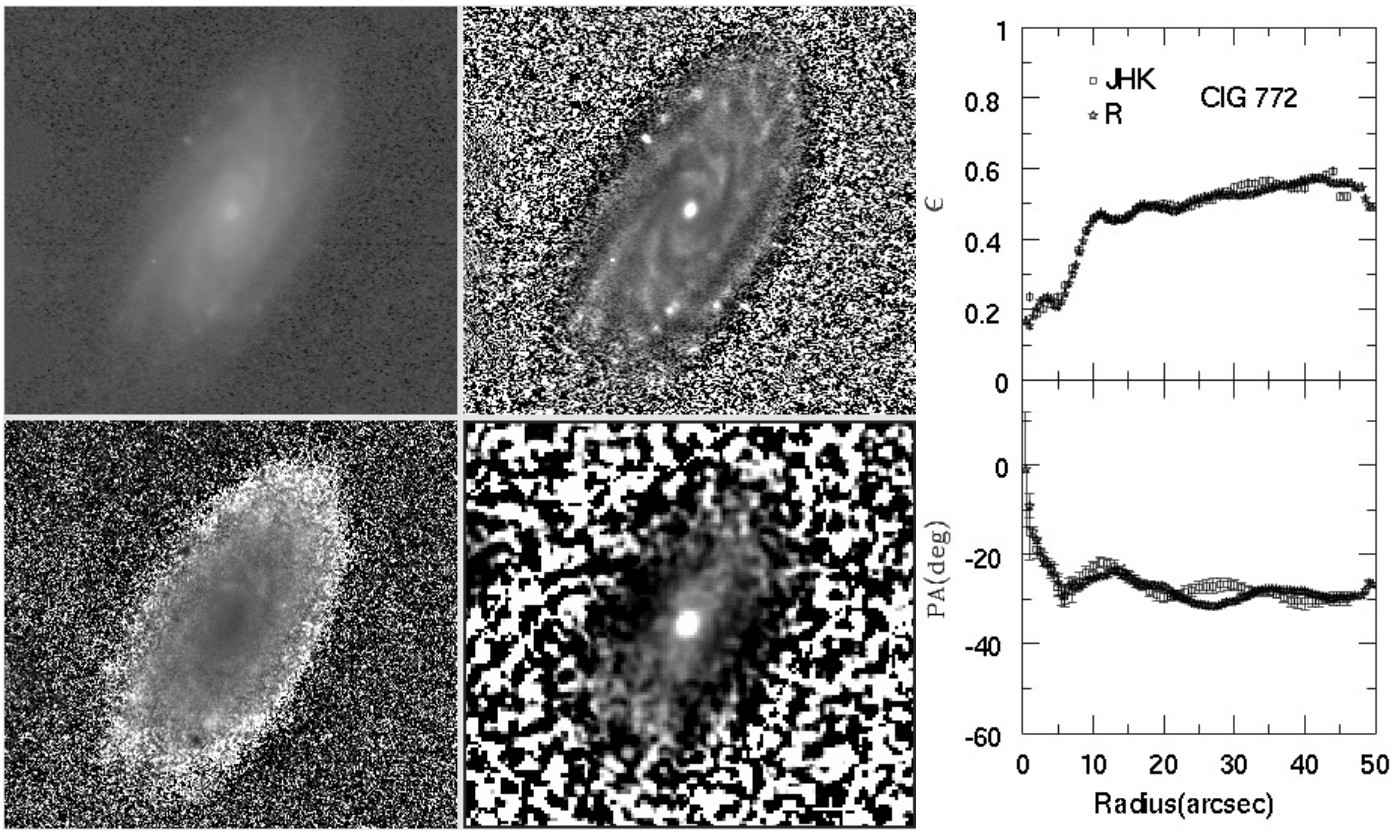

Fig. B.30. CIG 772 Mosaic. Same as Fig. 3. The major diameter of the galaxy in the optical images is 2.2 arcmin.

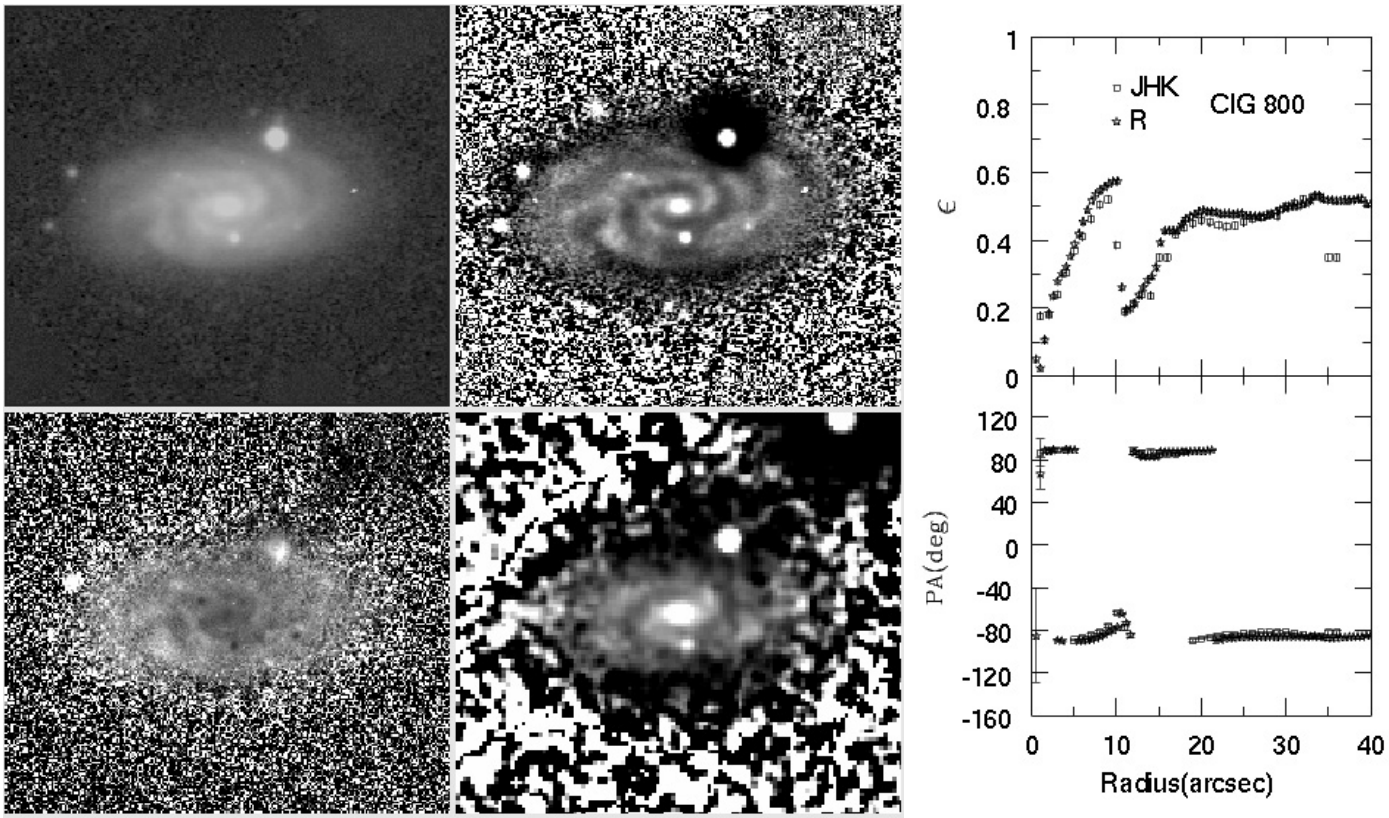

Fig. B.31. CIG 800 Mosaic. Same as Fig. 3. The major diameter of the galaxy in the optical images is 1.2 arcmin.

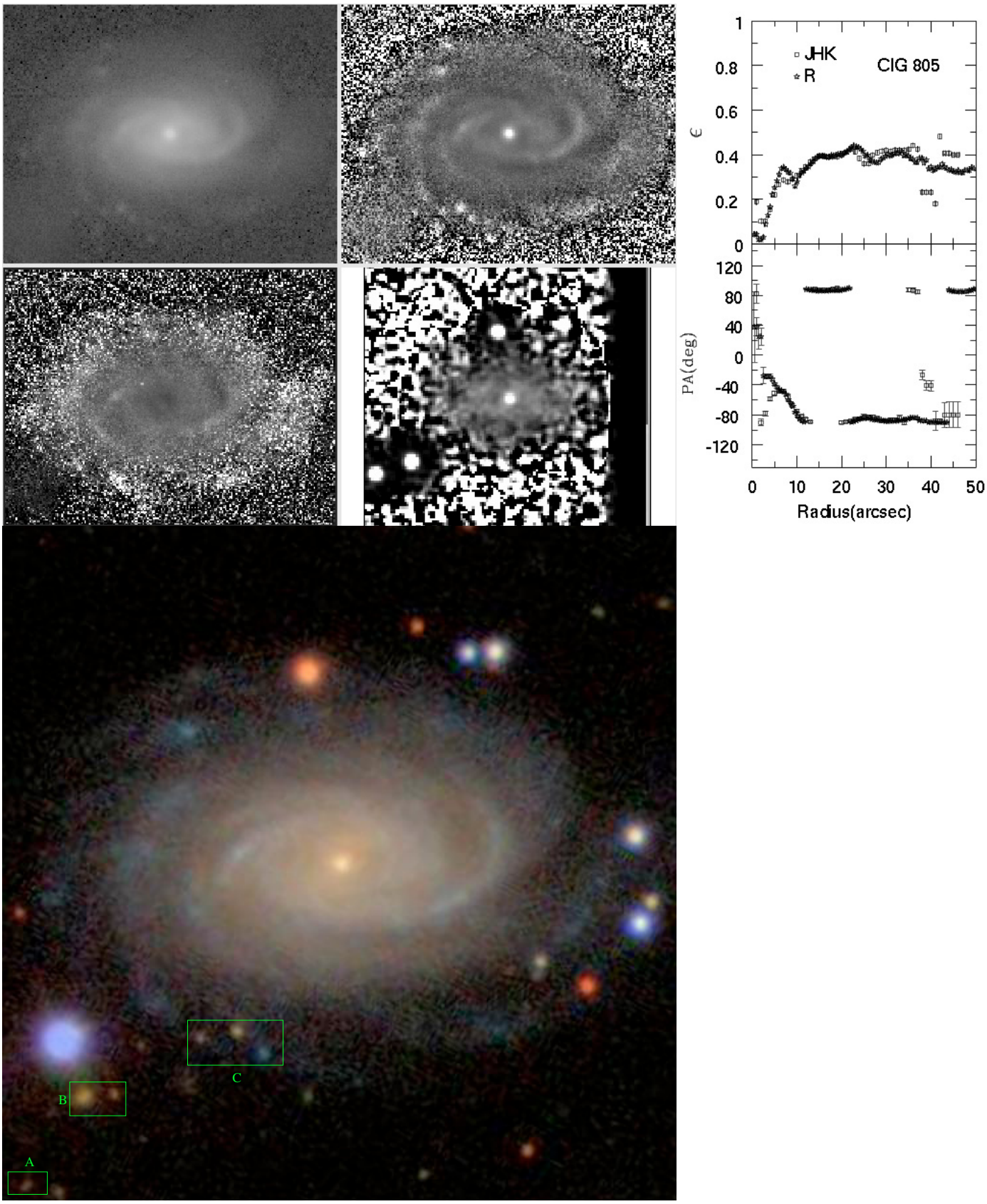

Fig. B.32. CIG 805 Mosaic. Same as Fig. 3. The major diameter of the galaxy in the optical images is 1.6 arcmin.

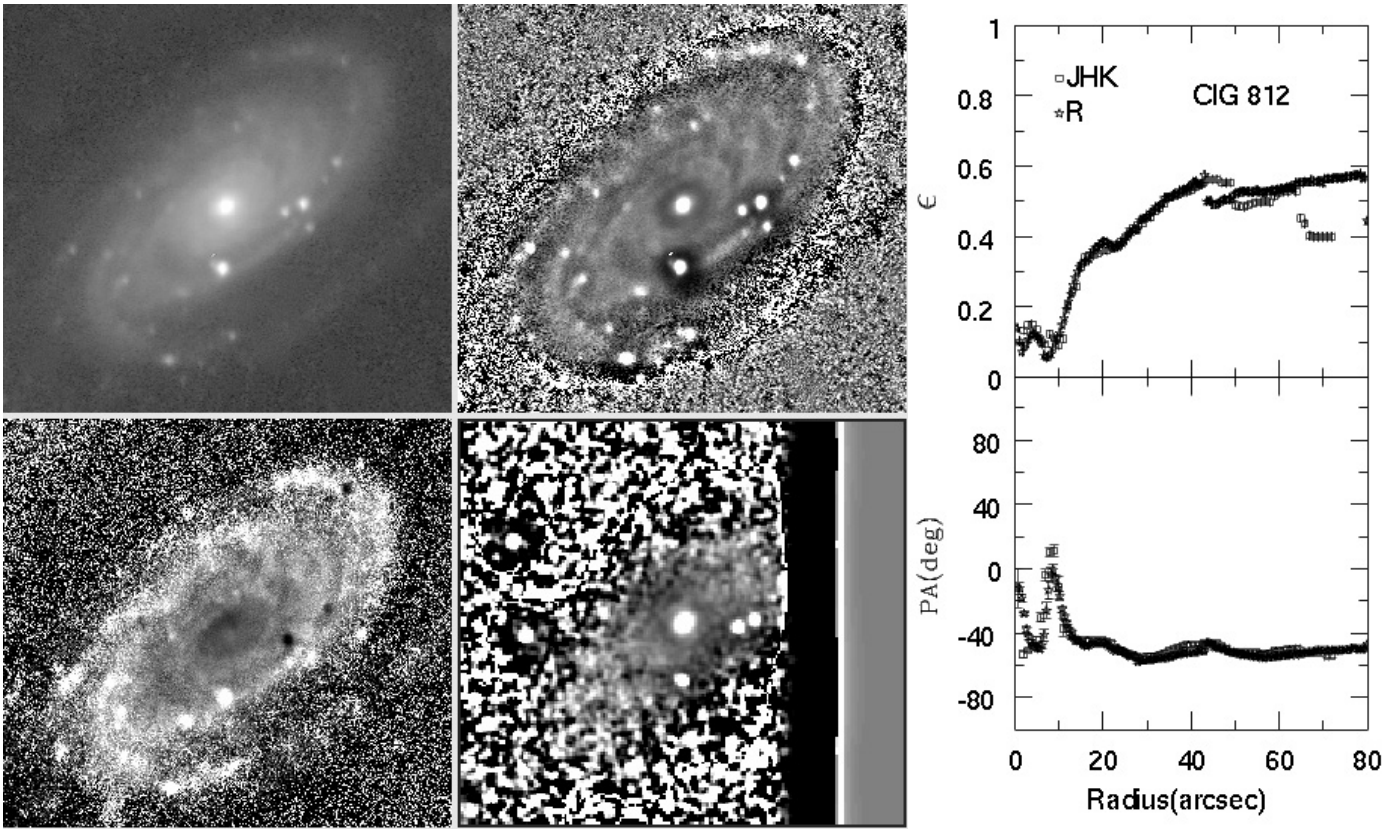

Fig. B.33. CIG 812 Mosaic. Same as Fig. 3. The major diameter of the galaxy in the optical images is 2.8 arcmin.

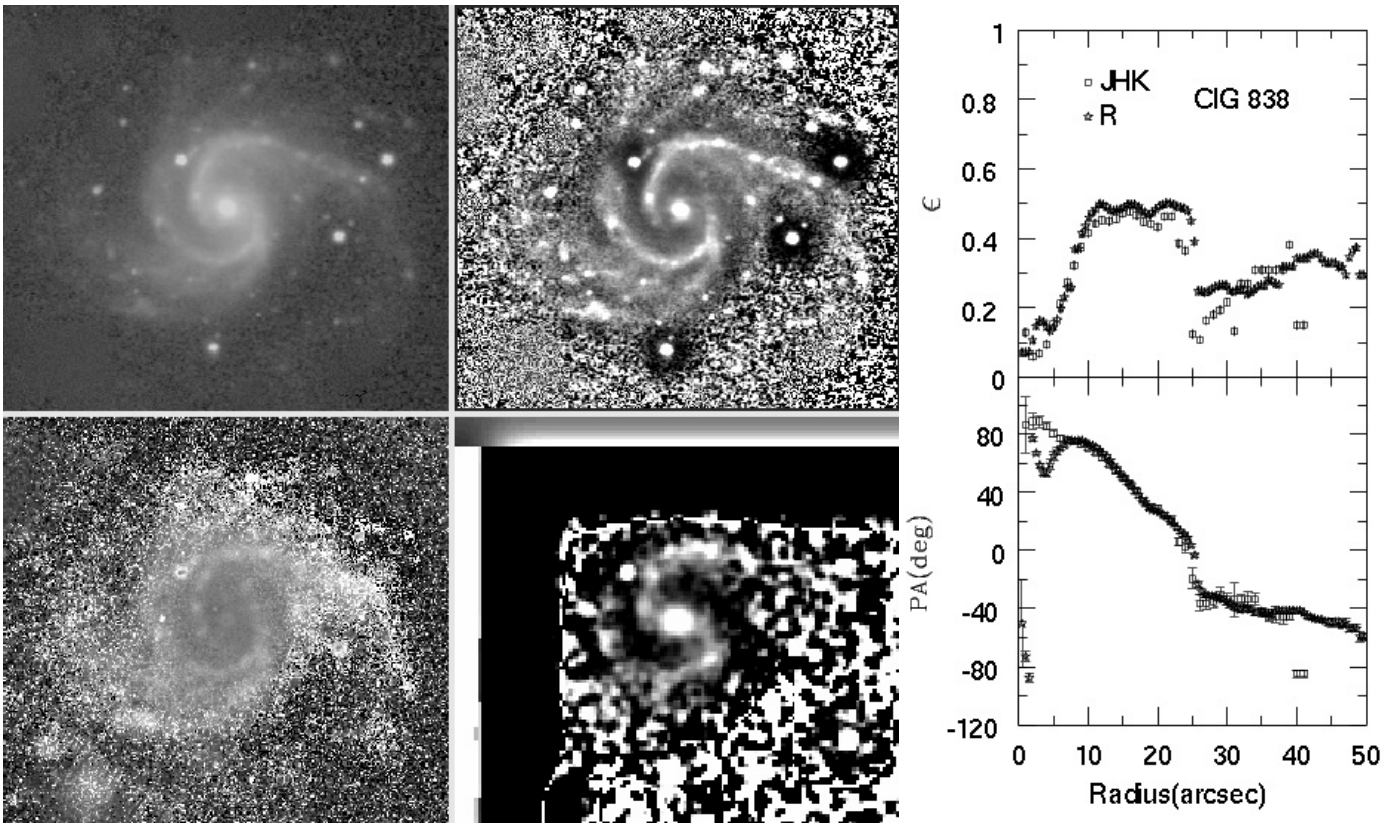

Fig. B.34. CIG 838 Mosaic. Same as Fig. 3. The major diameter of the galaxy in the optical images is 1.7 arcmin.

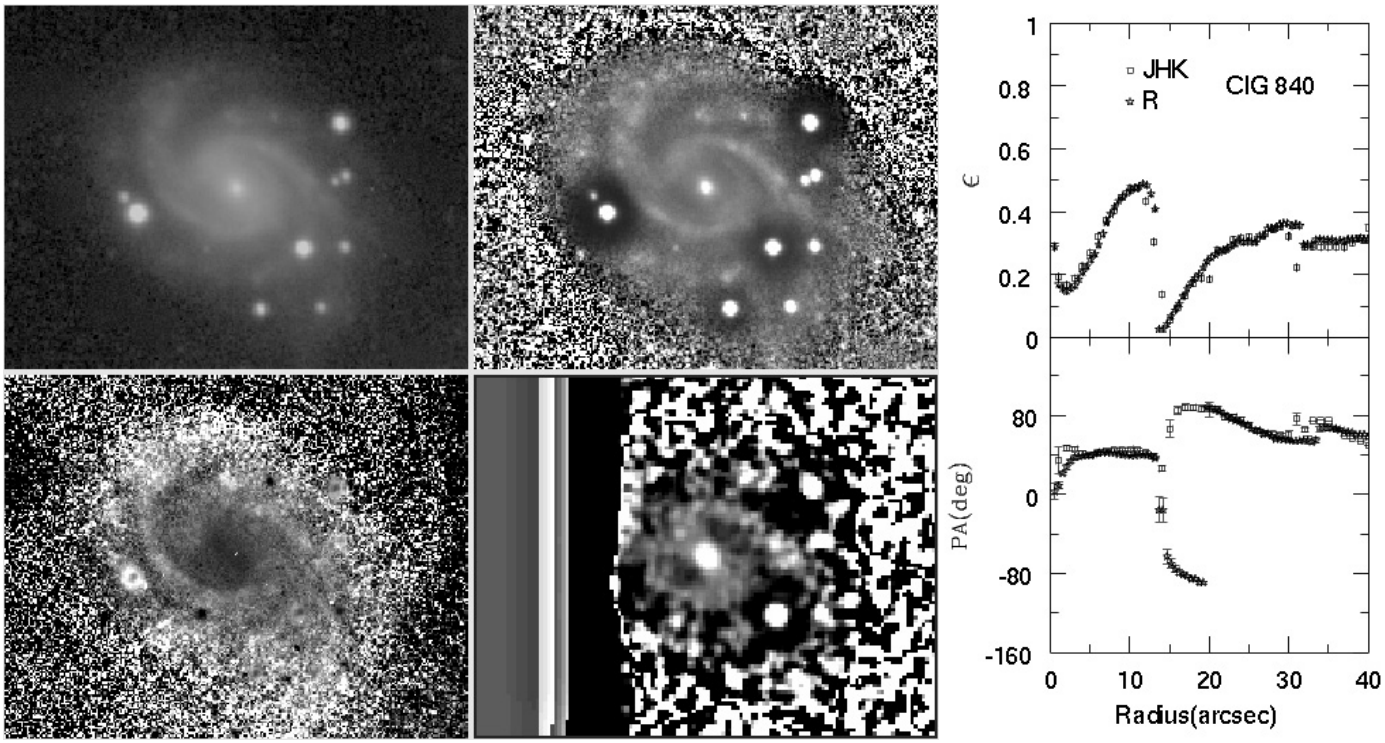

Fig. B.35. CIG 840 Mosaic. Same as Fig. 3. The major diameter of the galaxy in the optical images is 1.5 arcmin.

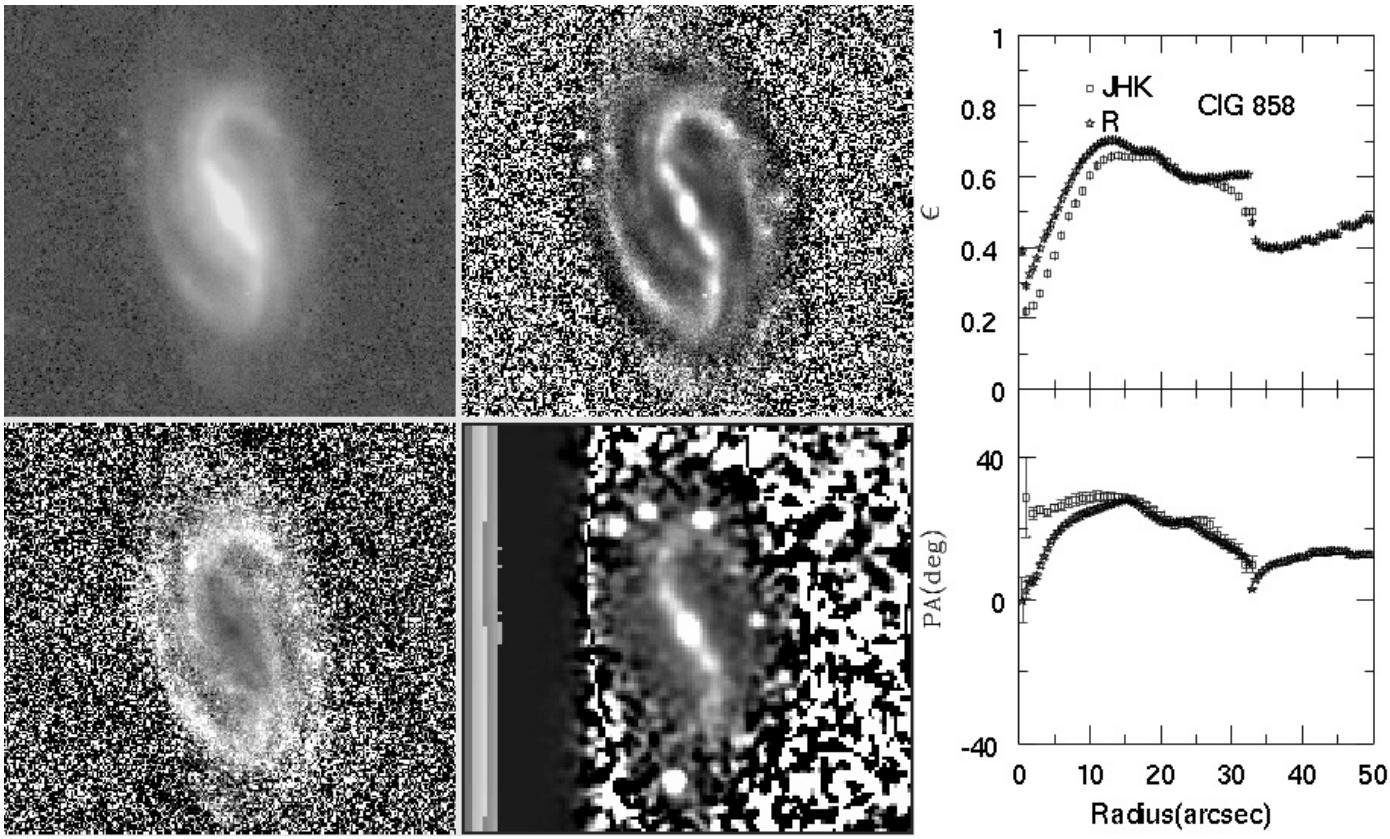

Fig. B.36. CIG 858 Mosaic. Same as Fig. 3. The major diameter of the galaxy in the optical images is 1.1 arcmin.

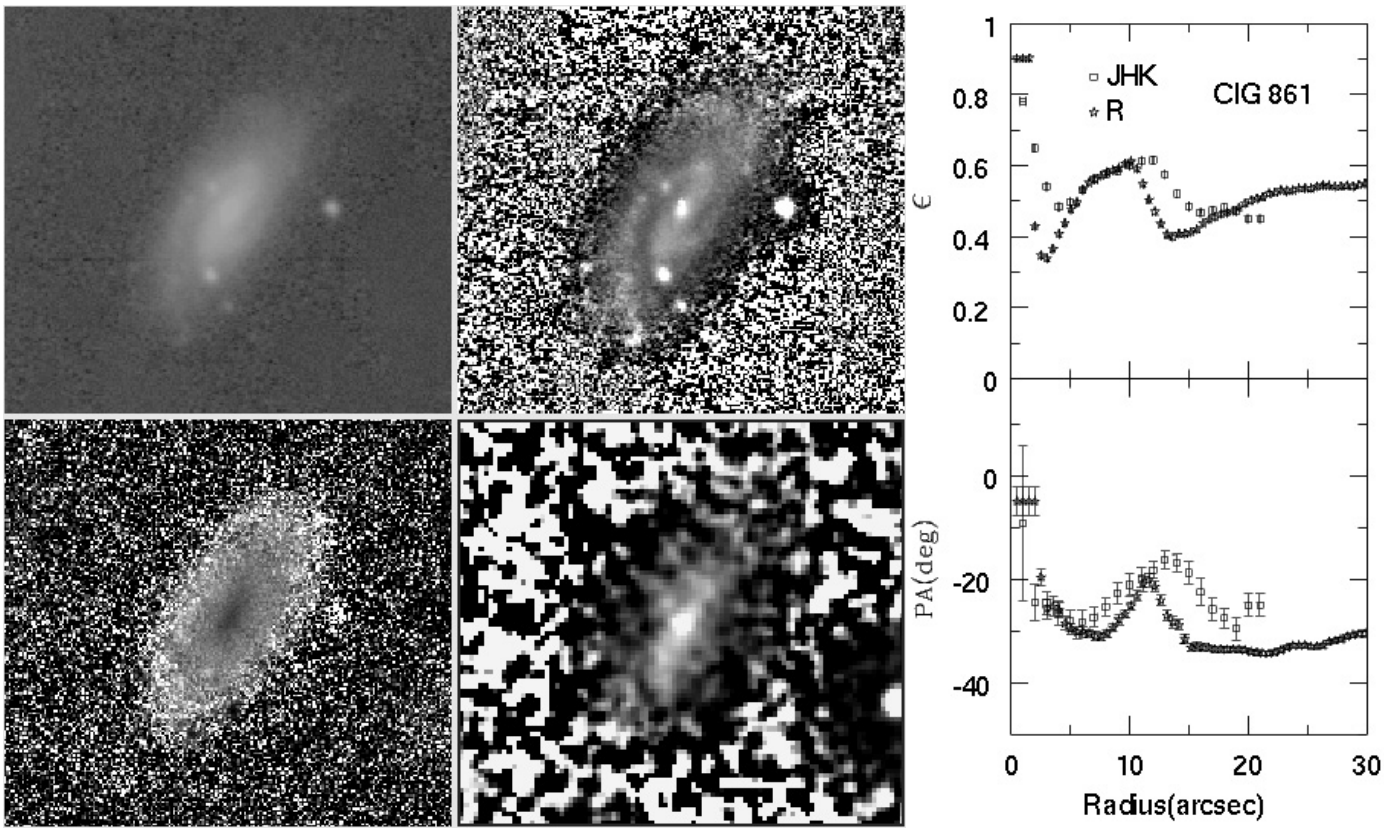

Fig. B.37. CIG 861 Mosaic. Same as Fig. 3. The major diameter of the galaxy in the optical images is 1.0 arcmin.

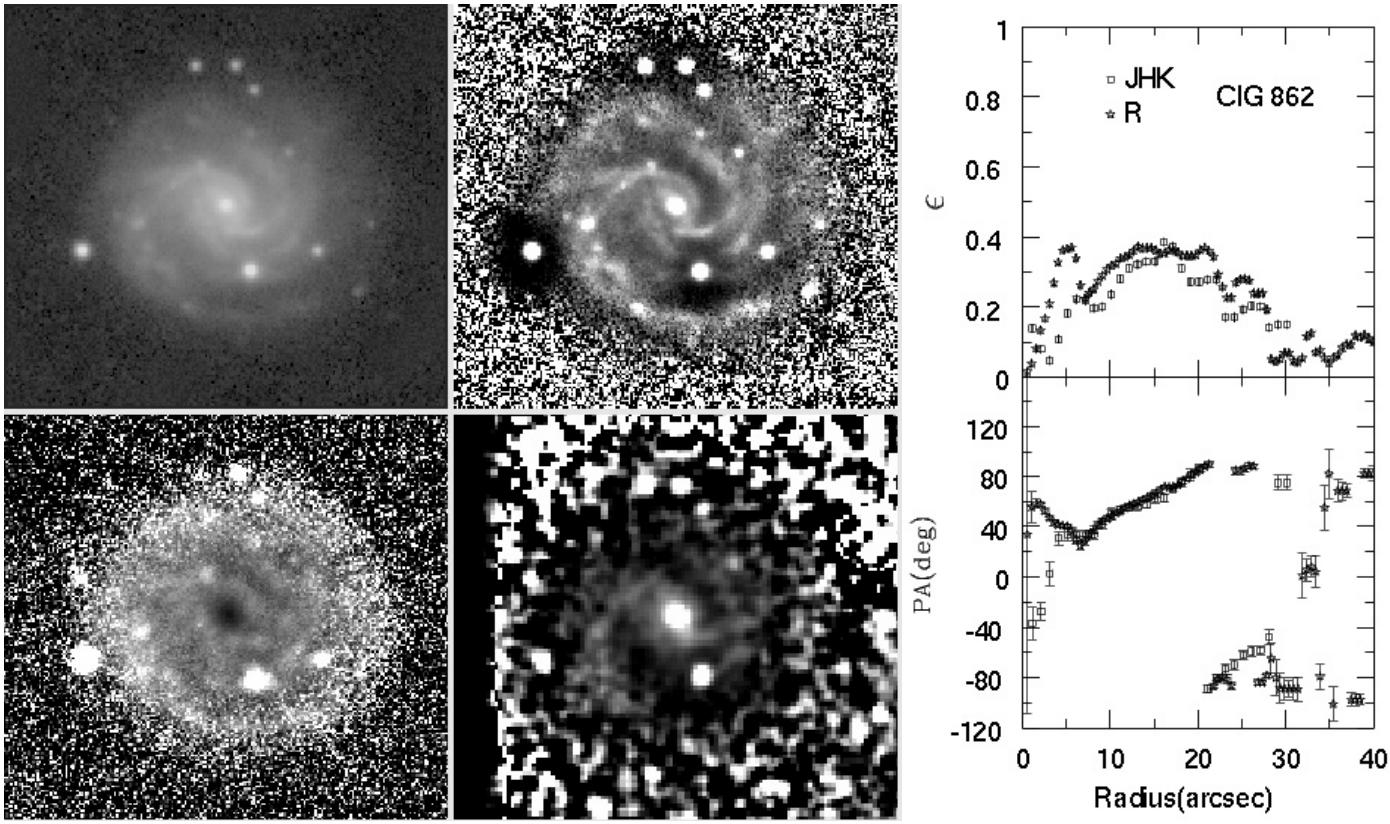

Fig. B.38. CIG 862 Mosaic. Same as Fig. 3. The major diameter of the galaxy in the optical images is 1.3 arcmin.

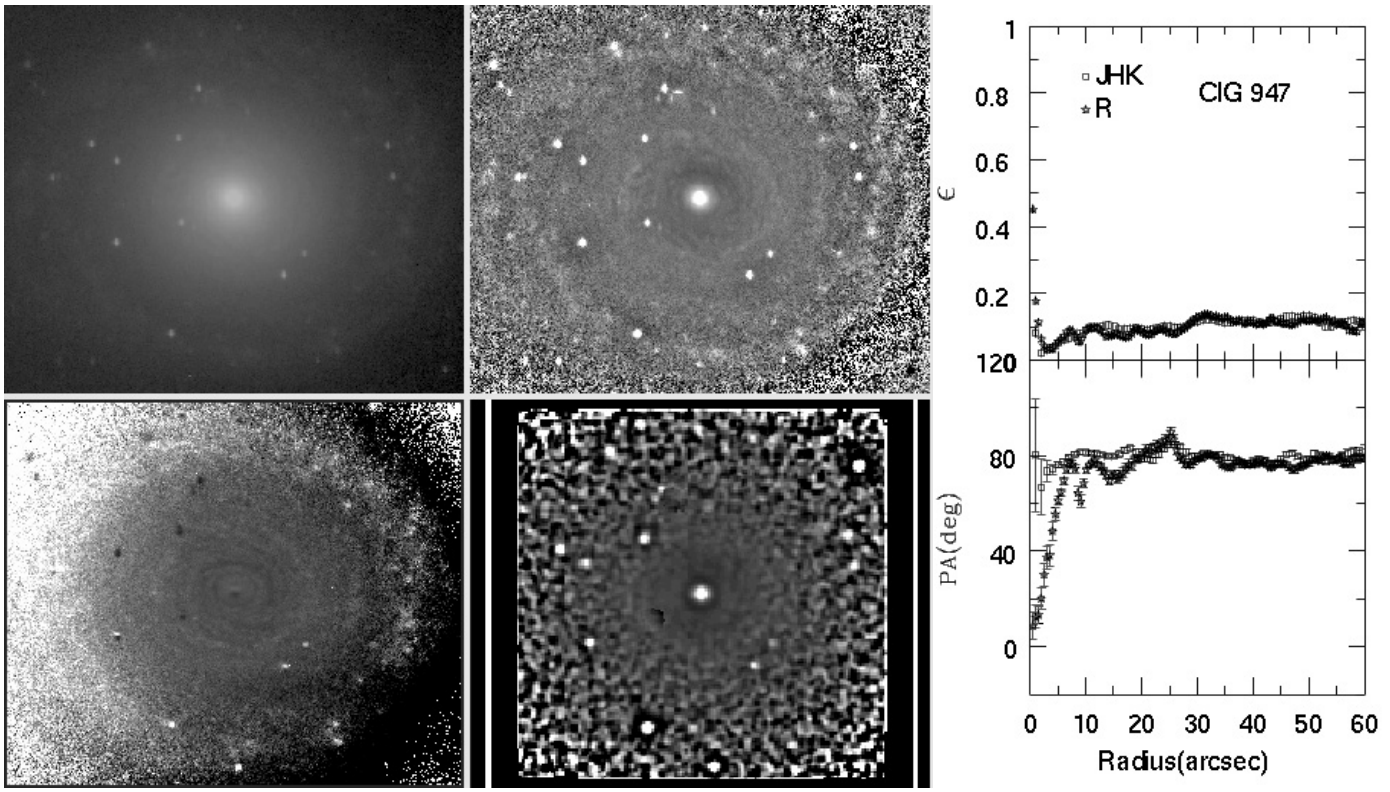

Fig. B.39. CIG 947 Mosaic. Same as Fig. 3. The major diameter of the galaxy in the optical images is 3.9 arcmin.